

BULGARIAN CHEMICAL COMMUNICATIONS

2020 Volume 52 / Number 3

*Journal of the Chemical Institutes
of the Bulgarian Academy of Sciences
and of the Union of Chemists in Bulgaria*

An efficient synthesis of azidohydrin catalyzed by a novel polymeric ionic liquid

B. Mombeni Goodajdar*, F. Akbari

Department of Chemistry, Omidyeh Branch, Islamic Azad University, Omidyeh, Iran

Received: January 27, 2019; Revised: March 17, 2020

In the current study, PEG-supported dicationic ionic liquid was synthesized as a green catalyst and applied in the ring opening of epoxides under reflux conditions in water. The reactions occurred in water and furnished the corresponding β -azido alcohol in high yields. The method described herein is a very good, safe, clean, economical and environmentally friendly alternative to the classical procedures. The structural properties of the catalyst were investigated by FT-IR, UV-VIS, Raman spectra and TGA analysis.

Keywords; Epoxide, Azido alcohol, Magnetic ionic liquid, Regioselectivity, Ring opening

INTRODUCTION

The dicationic ionic liquids (DILs) have two head groups, linked *via* a flexible spacer or a rigid spacer. This type of ionic liquids (ILs) has revealed unique characteristics of critical micelle concentration (CMC), more efficient behavior as lubricants, properties of electrolytes, surface tension, and greater thermal stabilities than monocationic ILs and other traditional solvents. Dicationic ionic liquids are an attractive new group of ionic liquids that acquire higher melting point, wider liquid range and better thermal stability. In addition to a combination of anion and cation, simple changes in the length of the spacer or in the aliphatic chains on the cations allow to tailor ILs' physical properties for certain applications [1-3].

PEG-DILs are new salts making the link between two distinct but very similar fluids: ionic liquids and poly (ethylene glycol). They exhibit excellent properties of ionic liquids in relation to green chemistry including low volatility, non-flammability, high thermal and chemical stability, negligible vapour pressure, and high solubility for both organic and inorganic materials [4].

The use of environmentally benign solvents instead of traditional organic solvents is an important and efficient strategy in green chemistry. Water is a promising green solvent for use in chemistry because it is cheap, readily available, and nontoxic. There is increasing recognition that organic reactions carried out in water may offer advantages over those in organic solvents. However, the poor solubility of reactants in water is the main obstacle to the use of water as a reaction solvent [5, 6].

Multiphase reactions are always difficult to take place owing to their immiscibility with each other

(basically aqueous and organic phases). However, with the help of an amphiphilic agent that is soluble both in aqueous and organic phases such reactions are now possible. These agents are phase transfer catalysts that along with helping the transfer of ion-pairs across the interfaces also help in enhancing the reaction rate. This process is called phase transfer catalysis (PTC). It's a green route to synthesize fine chemicals because of the advantages it has over other methods. In PTC, mild operating conditions are required, the yield of desired product is very high, unwanted side reactions are eliminated, and there is no generation of hazardous waste after the reaction completion. [7, 8].

Vicinal azido alcohols are an important class of organic compounds and they serve as precursors in the synthesis of vicinal aminoalcohols, carbohydrates, nucleosides, lactames, and oxazolines. They are usually prepared through ring opening of epoxides by using different kinds of azides in suitable solvents. The reactions are often carried out under either alkaline or acidic conditions and several different methods have been devised in order to obtain the direct azidolysis of epoxides in the presence of sodium azide. Under these conditions, azidolysis is usually carried out over a long reaction time and obtaining of azidohydrin is often accompanied by isomerization, epimerization, and rearrangement of products. In order to overcome some of these limitations, a number of alternative procedures have been reported over the past few years using a variety of catalysts [9–17].

As a part of our program aiming at developing selective and environmentally friendly methodologies for the preparation of fine chemicals and in continuation of our interest in magnetic ionic liquid-promoted organic reactions, in this work, H₂O-PEG-MDIL was designed and applied for the

* To whom all correspondence should be sent:

E-mail: bmombeni@gmail.com, mombeni.b@iauo.ac.ir

© 2020 Bulgarian Academy of Sciences, Union of Chemists in Bulgaria

regioselective ring opening of epoxide under mild reaction conditions.

EXPERIMENTAL

Material and Methods

Melting points were measured on an Electrothermal 9100 apparatus and are uncorrected. ^1H and ^{13}C NMR spectra were recorded on a Bruker Avance DPX 400 MHz spectrometer using TMS as the internal standard in CDCl_3 . IR spectra were recorded on a BOMEM MB-Series 1988 FT-IR spectrometer. Raman spectra were recorded on a Bruker RFS 100/s Raman spectrometer. Thermogravimetric analysis was performed under nitrogen by means of a Perkin Elmer instrument. Epoxides and PEG-400 were purchased from Merck Company in high purity. Products were characterized by comparison of their physical and spectroscopic data with those of known samples. Checking of products purity and reaction monitoring was accomplished by TLC on silica gel Poly Gram SILG/UV 254 plates.

The synthesis of dichloro substituted (Cl-PEG-Cl)

PEG-400 (15 g, 0.025 mol) and pyridine (5 mL, 0.0625 mol) were dissolved in toluene (20 mL), stirred at 87°C , thionyl chloride (5 mL, 0.0625 mol) was added slowly, and the resultant reaction mixture was stirred at 87°C for 15 h. Then the resulting solid was removed by filtration. After removal of the solvent under reduced pressure a viscous liquid residual was collected as dichloro substituted PEG-400 (91.6%).

Procedure for preparation of poly(ethylene glycol) bis(methylimidazolium chloride) (PEG-DIL). 1-Methylimidazole (2 mmol), and polyethylene glycol dichloride (1 mmol) were placed in a Pyrex glass tube, sealed and heated at 80°C for 16 h or at 110°C for 20 h. The organic solvent was removed and the residue was extracted with ethyl acetate (3×20 mL) and then washed with water (2×20 mL) and ether (2×10 mL), and dried over anhydrous magnesium sulfate. The solvent was removed under vacuum at 65°C overnight to give a colorless product.

Procedure for preparation of PEG-DIL based $\text{MnCl}_4 \cdot 2\text{H}_2\text{O}$. A solution of (0.2 g, 1 mmol) of $\text{MnCl}_2 \cdot 4\text{H}_2\text{O}$ in ethanol (10 mL) was added to a solution (1.0 mmol) of PEG-DIL [18] in ethanol (10 mL). After heating under reflux for 4 h, to give a pale yellow solution, preconcentration under reduced pressure led to a viscous liquid (90%).

General procedure for preparation of 1,2-azido alcohols. In a round-bottomed flask (25 mL) equipped with a condenser and a magnetic stirrer

bar, epoxide (1 mmol), nucleophilic reagent (NaN_3) (2 mmol), and Mn-DIL-MnCl_4 (0.2 g) in water (5 ml) were added, and heated under reflux conditions for an appropriate time (Table 2). The progress of the reaction was monitored by TLC (eluent: n-hexane/ethyl acetate 80:20). After completion of the reaction, the mixture was extracted with ether (2×10 ml). The extract was dried over anhydrous calcium chloride, and concentrated under vacuum to obtain 1,2-azido alcohols in 82-90% isolated yields.

1-Azido-3-phenoxypropan-2-ol (3a): FT-IR (neat): ν_{max} N_3 (2100 cm^{-1}); ^1H NMR (400 MHz, CDCl_3): 3.51 (d, 2H), 3.88–3.98 (m, 1H), 4.00 (d, 2H), 4.16 (s, 1H), 6.93–7.00 (m, 2H), 7.01–7.06 (m, 1H), 7.26–7.36 (m, 2H). ^{13}C NMR (100 MHz, CDCl_3): 53.50, 69.23, 69.20, 114.29, 121.15, 129.43, 158.37.

2-Azido-2-phenyl-1-ethanol (3b): FT-IR (neat): ν_{max} N_3 (2103 cm^{-1}); ^1H NMR (400 MHz, CDCl_3): 3.36 (s, 1H), 3.73 (m, 2H), 4.65 (m, 1H), 7.33–7.44 (m, 5H). ^{13}C NMR (100 MHz, CDCl_3): 66.27, 68.03, 127.47, 128.40, 128.51, 136.27 ppm.

2-Azidocyclohexan-1-ol (3c): FT-IR (neat): ν_{max} N_3 (2097 cm^{-1}); ^1H -NMR (400 MHz, CDCl_3): 1.20–1.36 (m, 4H), 1.71–1.78 (m, 2H), 2.00–2.08 (m, 2H), 2.52 (s, 1H), 3.10–3.22 (m, 1H), 3.28–3.42 (m, 1H). ^{13}C -NMR (100 MHz, CDCl_3): 24.36, 24.47, 24.52, 33.14, 62.15, 73.78.

1-Azido-3-propoxypropan-2-ol (3d): FT-IR (neat): ν_{max} N_3 (2102 cm^{-1}); ^1H NMR (400 MHz, CDCl_3): δ : 1.07 (t, 3H), 1.70–1.78 (m, 2H), 3.82 (s, 1H), 3.30 (m, 2H), 3.38 (t, 2H), 3.42 (d, 2H), 3.86 (m, 1H). ^{13}C NMR (100 MHz, CDCl_3): δ : 19.15, 31.74, 53.50, 69.73, 70.59, 71.71 ppm.

1-Azido-3-allyloxy propan-2-ol (3e): FT-IR (neat): ν_{max} N_3 (2098 cm^{-1}), OH (3398 cm^{-1}); ^1H NMR (400 MHz, CDCl_3): δ : 5.85 (m, 1H), 5.2 (dd, 2H), 3.9 (q, 2H), 3.8 (s, 1H), 3.6 (q, 3H), 3.3 (m, 2H). ^{13}C NMR (100 MHz, CDCl_3): δ : 53.37, 69.52, 71.33, 72.17, 117.57, 134.46 ppm.

1-Azido-3-isopropoxypropan-2-ol (3f) liquid; FT-IR (neat): ν_{max} N_3 (2103 cm^{-1}); ^1H NMR (CDCl_3 , 400 MHz): δ : 1.40 (d, $J = 6.5$ Hz, 6H), 3.01 (m, 1H), 3.20 (dd, $J = 7.0, 11.5$ Hz, 1H), 3.25 (dd, $J = 4.0, 11.5$ Hz, 1H), 3.30–3.50 (m, 2H), 3.96 (brs, 1H, OH), 3.97–4.0 (m, 1H). ^{13}C NMR (CDCl_3 , 100 MHz) δ : 25.7, 53.4, 70.3, 71.12, 72.33 ppm.

1-Azidobutan-2-ol (3g): FT-IR (neat): ν_{max} N_3 (2098 cm^{-1}); ^1H NMR (400 MHz, CDCl_3): δ : 0.96 (t, 3H), 1.47 (m, 2H), 3.2 (m, 1H), 3.4 (d, 2H), 3.96 (br, 1H). ^{13}C NMR (100 MHz, CDCl_3): δ : 8.2, 27.6, 53, 71.2 ppm.

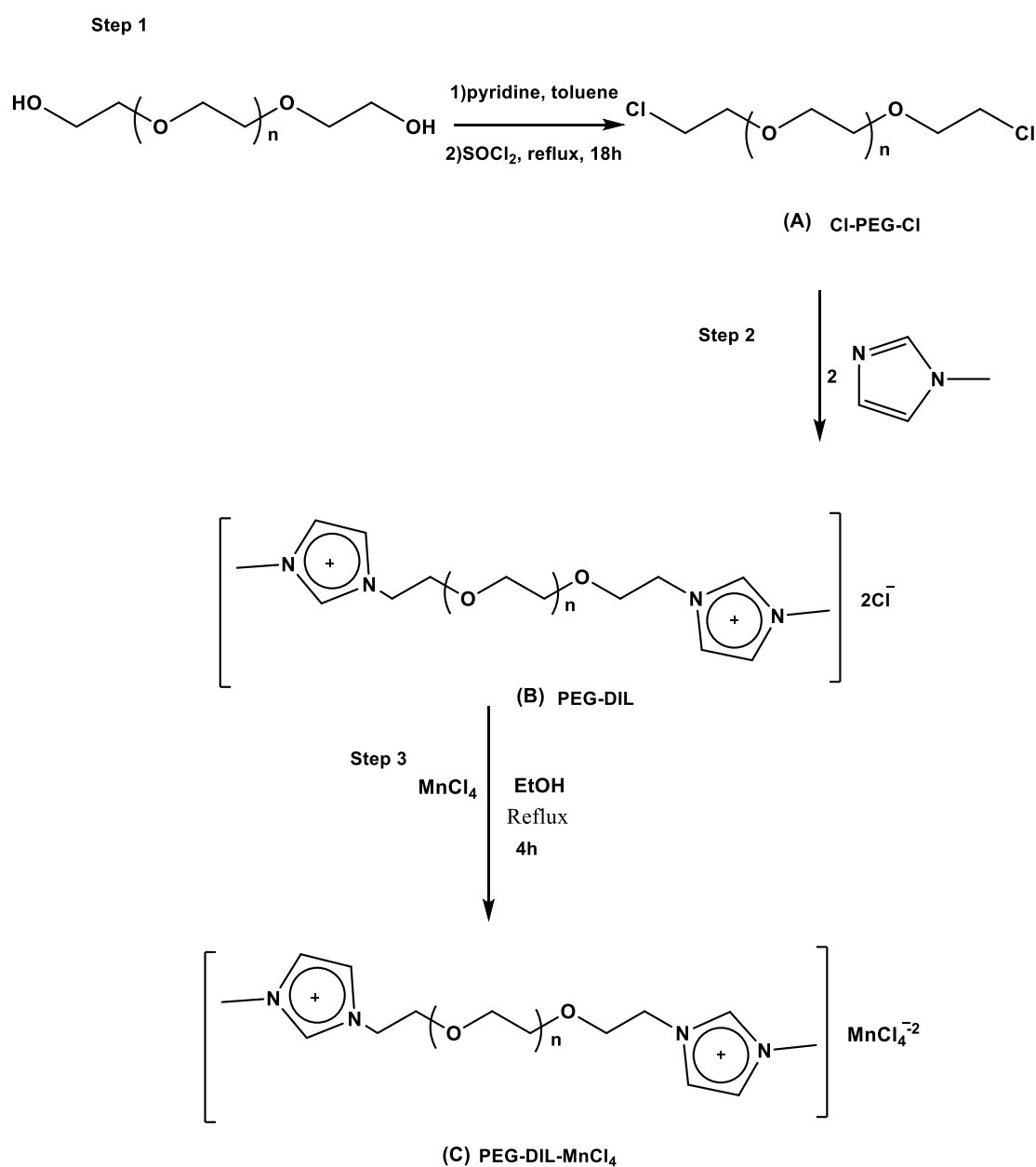
RESULTS AND DISCUSSION

In recent years, ionic liquids have been considered as catalysts or solvents in organic reactions and separation approaches. Herein, we desire to report the synthesis and application of a polymeric dicationic ionic liquid due to numerous benefits along with eco-friendliness, ease of separation of products, energy saving, and availability. The preparation route of PEG-DIL based MnCl_4^{2-} is shown in scheme 1.

The novel catalyst was characterized by FT-IR, UV-VIS, Raman, and TGA analysis. The FT-IR spectra of the native Cl-PEG-Cl and of the PEG-DIL- MnCl_4 sample are shown in Fig. 1. The lack of

OH peak in the poly (ethylene glycol) dichloride spectrum and appeared absorption frequency of C-Cl at 663 cm^{-1} suggests that the reaction between PEG and SOCl_2 has successfully occurred (Fig. 1a). There are peaks at about 1145 cm^{-1} , which were assigned to the characteristic absorption of N- CH_2 in the functionalized PEG-MDIL.

The absorption bands at 3152 and 3013 cm^{-1} (imidazolium CH stretching modes), presented in the inset of Figure 3 demonstrate modification of the PEG. The absorption at 2911 cm^{-1} is usually assigned to CH_2 stretching of the polyether linkage chains. The absorption observed at 1571 cm^{-1} is also characteristic of the imidazolium ring and is assigned to imidazolium ring stretching (Fig. 1b).



Scheme 1. Synthesis of PEG-MDIL- MnCl_4 .

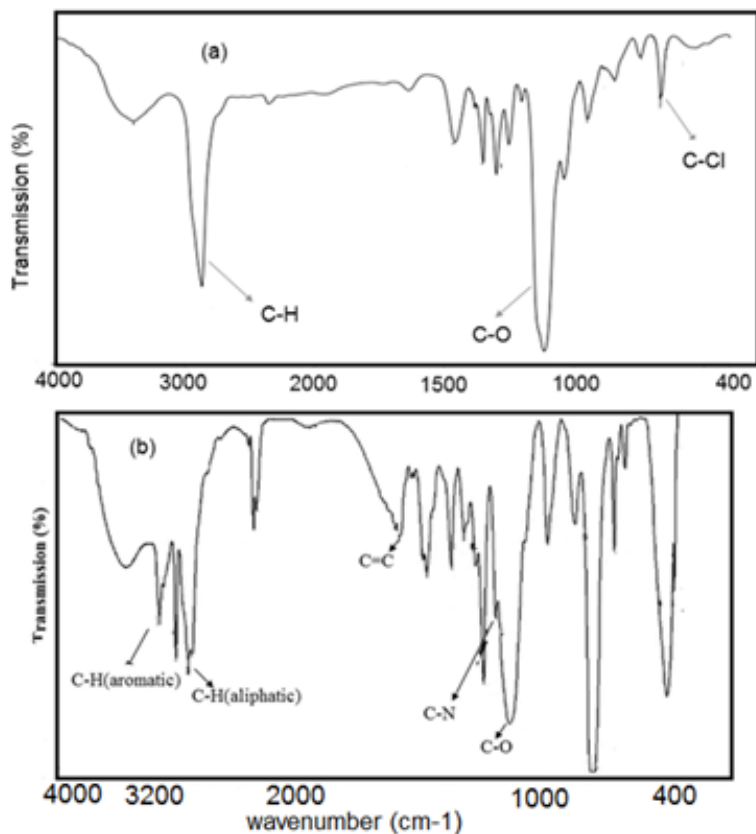


Fig. 1. FT-IR spectra of Cl-PEG-Cl(1a) and of PEG-DIL-MnCl₄(1b)

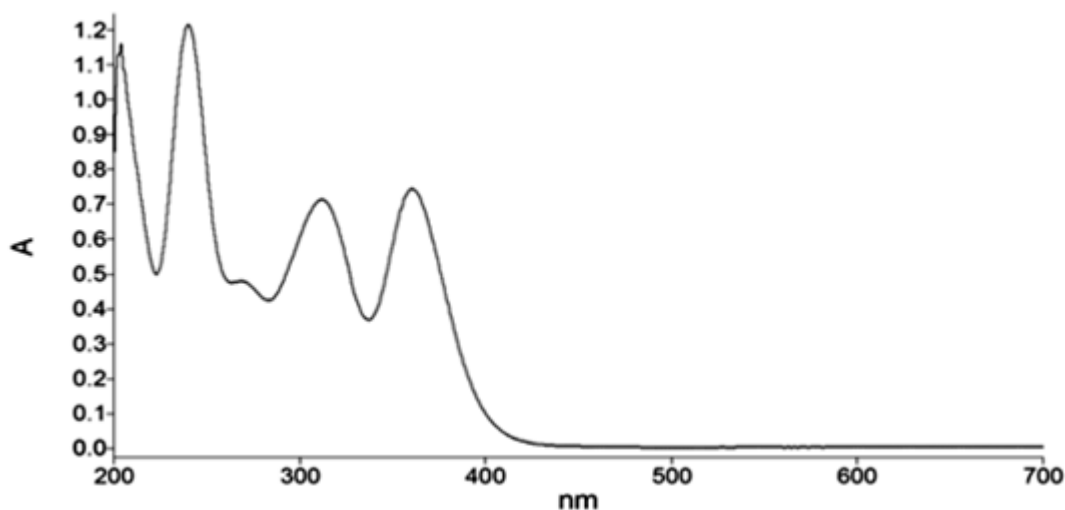


Fig. 2. Visible spectrum of PEG-DIL-MnCl₄

The UV/Vis spectrum of PEG-DIL-MnCl₄ is quite similar showing a strong band at 230-270 nm which corresponds to the π - π^* transition at the imidazolium cation and a band at 305-350 nm which is associated with ligand-to-metal charge transfer transition (Fig. 2). The thermal stability of PEG-DIL-MnCl₄ was studied by the use of TGA under N₂ atmosphere. From the TGA curve, it can be concluded that PEG-DIL based MnCl₄²⁻ is thermally

stable up to the temperature of about 250 °C under N₂ atmosphere. Weight loss of up to 200 °C is related to absorbed water evaporation. The significant weight loss occurs at 250 -400 °C, which is related to the degradation of imidazole rings and polyethylene glycol chains (Fig. 3).

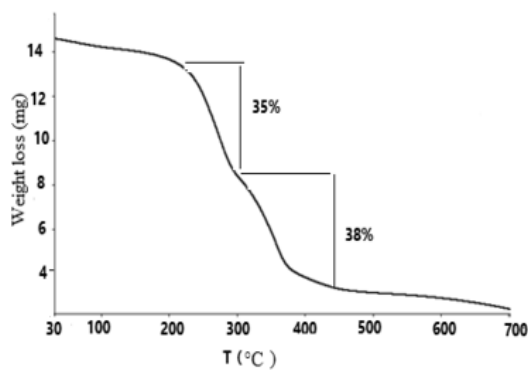


Fig. 3. TGA of PEG-DIL-MnCl₄

The Raman spectrum was used to prove the presence of the MnCl₄²⁻ anion in the structure of the ionic liquid. As shown in Fig. 4, strong and sharp peaks at 1296 and 1590 cm⁻¹ are related to imidazole rings, while the relatively weak peaks at 164.9 and 431.85 cm⁻¹ can be attributed to the presence of MnCl₄²⁻ anion in the structure of ionic liquid.

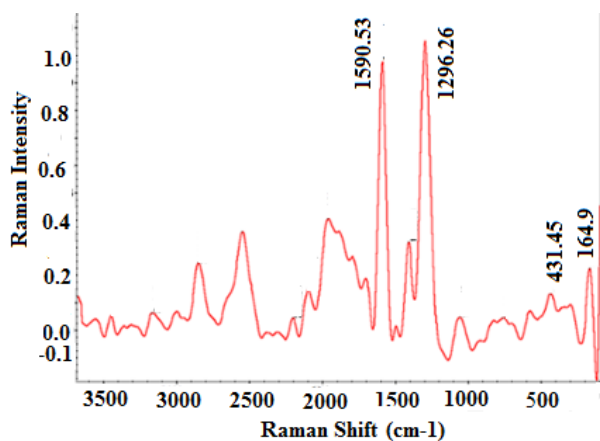


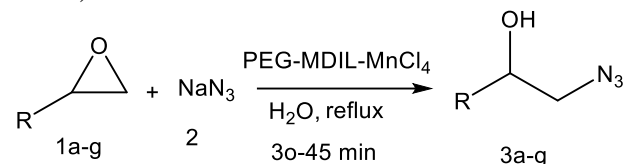
Fig. 4. Raman spectrum of PEG-DIL-MnCl₄

Table 1. Effect of the amount of PEG-DIL-MnCl₄, temperature and solvent in the synthesis of β-azidoalcohol

Entry	Catalyst (g)	T (°C)	Solvent	Time(min)	Yield
1	-	100	H ₂ O	180	-
2	0.05	100	H ₂ O	90	40
3	0.1	100	H ₂ O	90	70
4	0.2	100	H ₂ O	30	92
5	0.3	100	H ₂ O	30	92
6	0.2	100	CH ₃ CN	60	87
7	0.2	100	DMSO	30	88
8	0.2	100	CH ₂ Cl ₂	120	-
9	0.2	25	H ₂ O	180	Trace

After characterization, the possible catalytic properties of PEG-DIL-MnCl₄ in the azidolysis reaction of epoxides with azide anion in water were studied (scheme 2).

To optimize the reaction conditions, the mixture of phenyl glycidyl ether (1 mmol) and NaN₃ (2 mmol) in water were chosen for the model reaction.

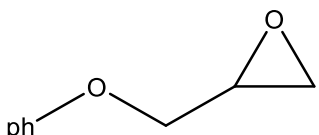
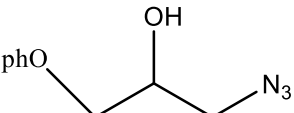
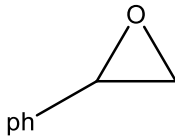
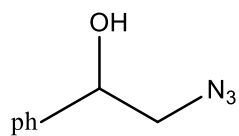
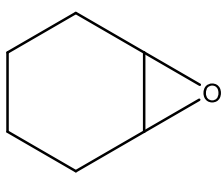
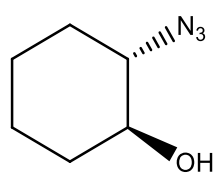
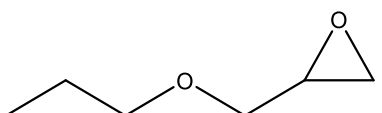
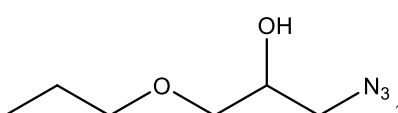
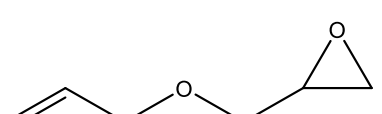
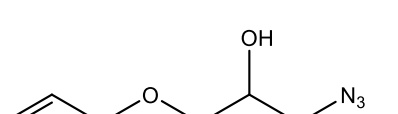
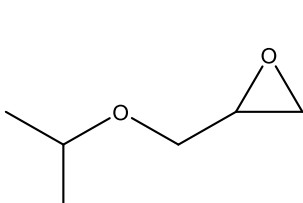
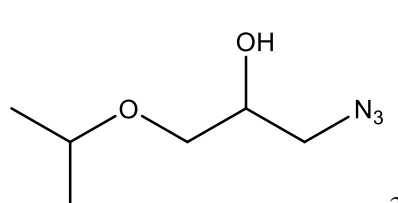
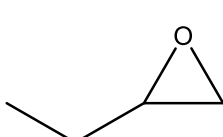
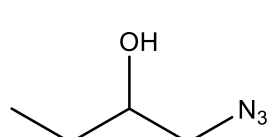


Scheme 2. Synthesis of β-azido alcohols in the presence of PEG-MDIL-MnCl₄.

The reaction was conducted with different amounts of catalyst and solvent in the temperature range from room temperature up to 100 °C. It was observed that the reaction model did not carry out at room temperature with different amounts of the catalyst. The best yield (92%) and reaction time (30 min) for preparation of azidoalcohol were obtained in the presence of 0.2 g of PEG-DIL-MnCl₄ in water as a green solvent at 100 °C. It is worth noting that in the absence of catalyst, the reaction was sluggish and, even after long reaction times, a considerable amount of starting material remained (Table 1).

Thus, water is an excellent solvent in terms of cost, availability, environmental impact and shorter reaction times. Epoxides bearing activated and deactivated groups were quickly and efficiently converted to the virtually pure β-azidoalcohol in high isolated yields (Table 2).

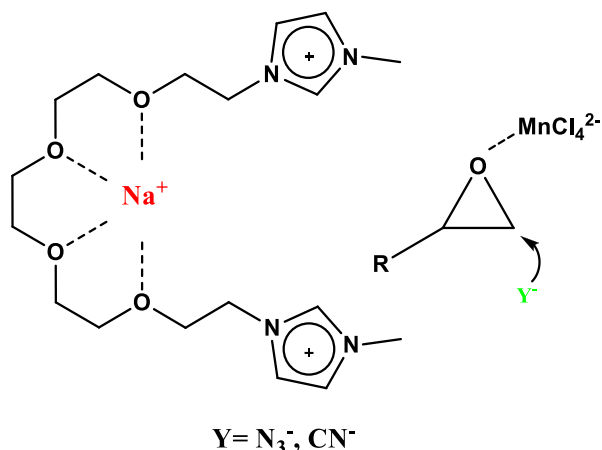
Table 2. Ring opening of various epoxides in the presence of PEG-DIL-MnCl₄

Substrate	Product	No.	N ₃ ⁻	
			Time (min)	Yield (%)
		3a	30	92
		3b	40	87
		3c	30	84
		3d	30	86
		3e	30	85
		3f	35	83
		3g	30	79

No evidence for the formation of diols or by-products of the reactions was observed and the products were obtained in pure form without further purification. All the products were characterized and identified by comparison of their spectral data (IR, ¹H NMR and ¹³CNMR) with those of authentic samples [19].

After completion of the reaction, the mixture was cooled and the organic phase was extracted with diethyl ether.

The PEG-DIL-MnCl₄ showed remarkable reactivity as a Lewis acid reagent and considerably accelerated the reactions. It seems that the counter cation (PEG-DIL) encapsulates alkali metal cations, much like crown ethers, and these complexes cause the anion to be activated. Also, Mn²⁺ in the MnCl₄²⁻ groups can act as a Lewis acid, catalyzing the ring opening of epoxides (Scheme 3).



Scheme 3. Possible mechanism for promotion of the reaction by PEG-DIL- $MnCl_4$

REFERENCES

1. J. H. Liang, X. Q. Ren, J. T. Wang, M. Jinag, Z. J. Li, *Journal of Fuel Chemistry and Technology*, **38**, 275 (2010).
2. D. Wei-Li, J. Bi, L. Sheng-Lian, L. Xu-Biao, T. Xin-Man, A. Chak-Tong, *Catalysis Today*, **233**, 92 (2014).
3. J. L. Anderson, R. Ding, A. Ellern, D. W. Armstrong, *Journal of the American Chemical Society*, **127**, 593 (2005).
4. (a) Y. L. Wang, J. Luo, Z. L. Liu, *J. Chin. Chem. Soc.* **60**, 1007 (2013); (b) Y. L. Wang, J. Luo, T. J. Hou, Z. L. Liu, *Aust. J. Chem.* **66**, 586 (2013); (c) J. Luo, T. T. Xing, Y. L. Wang, *New J. Chem.*, **37**, 269 (2013).
5. U. M. Lindström, *Chem. Rev.*, **102**, 2751 (2002).
6. M. Siskin, A.R. Katritzky, *Chem. Rev.*, **101**, 825 (2001).
7. E. V. Dehmlow, S. S. Dehmlow, *Phase Transfer Catalysis*, 3rd edn., VCH, Weinheim, 1993.
8. C. M. Starks, C. L. Liotta, M. H. Halpern, *Phase-Transfer Catalysis: Fundamentals, Applications and Industrial Perspectives*, Chapman & Hall, 1994.
9. S. L. Regon, L. Dulak, *Journal of the American Chemical Society*, **99**, 623 (1977).
10. D. M. Coe, P. L. Myers, D. M. Parry, S. M. Roberts, R. Storer, *Journal of the Chemical Society, Chemical Communications*, **2**, 151 (1990).
11. B. T. Smith, V. Gracias, J. Aube, *Journal of Organic Chemistry*, **65**, 3771 (2000).
12. J. G. Badiang, J. Aube, *Journal of Organic Chemistry*, **61**, 2484 (1996).
13. G. Sabitha, R. S. Babu, M. Rajkumar, J. S. Vadav, *Organic Letters*, **4**, 343 (2002).
14. P. Tanmaya, *Chemical Reviews*, **102**, 1623 (2002).
15. E. F. V. Seriven, K. Turnbull, *Chemical Reviews*, **88**, 297 (1988).
16. A. R. Kiasat, M. F. Mehrjardi, *Journal of the Iranian Chemical Society*, **6**, 542 (2009).
17. P. Crotti, V. D. Bussolo, L. Favero, F. Macchia, M. Pineschi, *Tetrahedron Letters*, **37**, 1675 (1996).
18. B. M. Godajdar, B. Ansari, *J. Mol. Liq.*, **202**, 34 (2015)
19. A. R. Kiasat, R. Mirzajani, H. Shalhaf, T. Tabatabaei, M. Fallah-Mehrjardi, *J. Chin. Chem. Soc.*, **56**, 594 (2009).

CO₂ methanation over Co–Ni/Al₂O₃ and Co–Ni/SiC catalystsA. G. Dyachenko¹, O. V. Ischenko¹, M. G. Zhudenko², S. V. Gaidai¹,
T. M. Zakharova¹, A. V. Yatsymyrskiy¹, V. V. Lisnyak^{1*}¹ Chemical Faculty, Taras Shevchenko National University of Kyiv, 64, Volodymyrska Str., 01033 Kyiv, Ukraine² Ukrorgsyntez Ltd, 67, Chervonotkatska Str., 02002 Kyiv, Ukraine

Received: April 15, 2019; Revised: March 23, 2020

In this study, highly loaded 20 wt% (Co_xNi_{100-x})/Al₂O₃ and (Co_xNi_{100-x})/SiC catalysts, where $x = 0, 20, 60, 80,$ and 100 wt%, were prepared by a three-stage method, which includes wet impregnation of Al₂O₃ and SiC with the metal nitrates, thermal decomposition of the loaded nitrates, and obtaining of the loaded metals by reducing their oxides with hydrogen at 350 °C. The prepared catalysts were examined by different methods and tested in the CO₂ methanation. Scanning electron microscopy and X-ray powder diffraction studies showed a difference in the loaded particle dispersion and the phase composition of catalysts. The highly loaded 20 wt% Co–Ni/Al₂O₃ catalysts showed the highest catalytic activity. In the presence of 20 wt% Co₆₀Ni₄₀/Al₂O₃, 20 wt% Co₈₀Ni₂₀/Al₂O₃, and 20 wt% Co₁₀₀/Al₂O₃ catalysts, 100% CO₂ can be converted into CH₄ at 300 °C. This temperature is lower by 100 °C than the temperature at the total conversion over 20 wt% (Co–Ni)/SiC catalysts. Thermal desorption mass spectroscopy revealed that the methanation of CO₂ passed through the formation of CHO* intermediate over the most active 20 wt% Co₈₀Ni₂₀/Al₂O₃ and 20 wt% Co₈₀Ni₂₀/SiC catalysts.

Keywords: Carbon dioxide methanation, Renewable fuels, Highly loaded Co–Ni catalysts, Alumina, Carborundum.

INTRODUCTION

Modern levels of energy consumption require identifying, preparing, and using new energy resources. Despite the growing role of renewable energy sources, organic fossil fuels remain the basic resources of energy. Their use has increased the amount of anthropogenic carbon dioxide (CO₂) and carbon monoxide (CO) in the atmosphere [1–3]. The average increase in CO₂ emissions *per annum* is about 2.2%. In this situation, an attractive problem solution is converting CO₂ into an eco-fuel, creating methane gas. By capturing CO₂ from the atmosphere and generating methane, we could solve environmental and energy problems. For the methanation reaction, the most used catalysts are based on nickel and cobalt metals [2–5]. Today, alumina (Al₂O₃) and carborundum (SiC) are valuable carriers/components that provide thermo-mechanical resistance for catalysts [6, 7]. The potential of catalysts, which were prepared by combining bimetallic active phase and inert carriers, was partially explored and reported in [8, 9].

In the present study, we reported on the activity and selectivity of Co–Ni/Al₂O₃ and Co–Ni/SiC catalysts in the CO₂ methanation. To find correlations between the catalyst activity and other physicochemical characteristics, we examined them by scanning electron microscopy (SEM), X-ray powder diffraction (XRPD), and thermal desorption

mass spectroscopy (TD MS).

EXPERIMENTAL

Materials

Reakhim Al₂O₃ and SiC powders were products of reagent quality. The metal nitrate salts, nickel nitrate hexahydrate (Ni(NO₃)₂·6H₂O) and cobalt nitrate hexahydrate (Co(NO₃)₂·6H₂O), were purchased from Aldrich.

Preparation

Both Al₂O₃ and SiC carriers were wet impregnated with the required quantity of Co(NO₃)₂ and Ni(NO₃)₂ aqueous solutions prepared from the respective hexahydrates. The metal salt solutions contained, according to the desired Ni and/or Co loading, different masses of dissolved Ni(NO₃)₂ or/and Co(NO₃)₂, which were accounted in such a way, to prepare 20 wt% (Co_xNi_{100-x})/Al₂O₃ and 20 wt% (Co_xNi_{100-x})/(SiC) catalysts, where $x = 0, 20, 60, 80,$ and 100 wt%.

During wet impregnation, the selected carrier (Al₂O₃ or SiC) was placed in a glass beaker, and aqueous solutions of Ni(NO₃)₂ or Co(NO₃)₂, or their mixed solution with a volume significantly higher than the pore volume of the carrier was added. The water from the solutions impregnating the carrier solids was vaporized on a thermostat bath at 80 °C in an evaporating dish, and afterward, the resulting solid samples were air-dried for 12

* To whom all correspondence should be sent:
E-mail: lisnyak@chem.univ.kiev.ua

hours at 120 °C.

The prepared samples containing cobalt and nickel oxides were reduced in a quartz glass reactor at atmospheric pressure. For the reduction, 0.5 cm of quartz wool and 2.0 g of the dried solid were packed in the reactor, and a thermocouple was placed directly within the packed bed. Hydrogen gas, which was used for reduction, was diluted with helium up to 50 vol% helium concentration in the resulting H₂–He mixture. The reduction in flowing hydrogen (volumetric flow: 100 mL/min) occurred at 350 °C within 120 min (heating rate: 10 °C/min). As a result, an active phase, in the form of bimetallic Co/Ni particles, was formed on the surface of the carriers.

Catalytic test

The methanation of CO₂, according to the reaction $\text{CO}_2 + \text{H}_2 = \text{CH}_4 + \text{H}_2\text{O}$, was carried out in the presence of a catalyst in a fixed-bed quartz reactor at atmospheric pressure. The catalyst packed volume and the catalyst mass were 1 cm³ and 1 g, correspondingly, and the major portion of particles was between 40 and 100 mesh. The closed packed reactor was placed in a programmable resistive furnace, and then the catalysts sample was treated in the reaction mixture under gradually raised temperature from 30 to 450 °C (heating rate: 10 °C/min). The reaction temperature inside the catalyst layer was monitored with a covered thermopile. A thermal conductivity detector on a Shimadzu GC 2014 gas chromatograph was used to analyze the outlet and inlet gas mixtures. All gases were separated for the analysis on a 1.0 m chromatographic column packed with molecular sieves. For the catalytic CO₂ methanation [10, 11], the conversion of CO₂ (X_{CO_2}) and the yields of CO and CH₄ (Y_{CO} and Y_{CH_4}) were calculated from the equations:

$$X_{\text{CO}_2} (\%) = \frac{[\text{CO}_2]_{\text{in}} - [\text{CO}_2]_{\text{out}}}{[\text{CO}_2]_{\text{in}}} \times 100 \quad (1)$$

$$Y_{\text{CO}} (\%) = \frac{[\text{CO}]_{\text{out}}}{[\text{CO}_2]_{\text{in}}} \times 100 \quad (2)$$

$$Y_{\text{CH}_4} (\%) = \frac{[\text{CH}_4]_{\text{out}}}{[\text{CO}_2]_{\text{in}}} \times 100 \quad (3)$$

where $[\text{CO}_2]_{\text{in}}$, $[\text{CO}_2]_{\text{out}}$, $[\text{CO}]_{\text{out}}$, and $[\text{CH}_4]_{\text{out}}$ are the gas volume concentrations in mixtures sampled at the inlet and outlet (see respective indices) of the catalytic reactor.

Characterization

Morphological studies and microanalysis were carried out on a MIRA3 Tescan scanning electron microscope equipped with an energy-dispersive X-ray spectroscopy analyzer (EDX) for elemental analysis.

XRPD patterns were collected on a Dron-4-07 diffractometer; the wavelength of CuK α radiation was used. Phase analysis was performed using structural data available in open crystallographic databases or can be extracted for single phases from open databases for powder diffraction. Specific surface areas (S_{sp}) were measured by argon adsorption at –196.15 °C and 25 °C.

The catalyst samples for the TD MS studies were prepared in the same reactor and under the same conditions used for the catalytic tests. Upon reaching the temperature at a maximum CO₂ conversion, the methanation in the presence of a selected catalyst was carried out for 2 hours at the stated temperature, and then the catalytic reactor was quenched to room temperature under the flow of the reaction mixture. Afterward, the sampled mass was transferred under the flow of reacting gases to a quartz glass ampoule, and then the ampoule was vacuumed. All operations were carried out at room temperature using standard Schlenk techniques. Under the stated conditions of the catalyst sampling, we fixed the surface of the catalyst covered with adsorbed products, reagents, and intermediate compounds. Subsequently, we collected structural information on the adsorbed particles, including those involved in the CO₂ methanation reaction, directly from the fragmentation pattern of molecules which was registered by the electron impact ionization mass spectroscopy (MS) method.

For this purpose, after vacuum sealing, the ampoule with the sample was disconnected from the vacuum pump, and the ampoule's outlet was connected online to the ionization source of a unipolar quadrupole mass-spectrometer (Selmi, MX7304A model). MS data were acquired from the m/z range 10–100, and thermal desorption (TD) profiles were registered in the temperature range from ambient temperature to 800 °C, under the heating rate of 14 °C/min [12]. The constant heating rate was provided by a toroidal (elliptical) electric heater concentrating heat onto the ampoule. The temperature was controlled with a type K thermocouple positioned in the thermowell of the ampoule. This thermocouple was placed as close as possible to the catalyst sample. The working vacuum was varied from 10^{–4} to 10^{–5} Pa that allowed the detection of very small amounts of

desorbed particles (10⁻⁴ to 10⁻⁵ moles/m³). Considering the TD profiles and the current of desorbed particles registered in the positive ion mode, one can qualitatively characterize the processes occurring on the surface of the catalyst, and one can propose the possible mechanism of the reaction.

RESULTS AND DISCUSSION

According to Table 1, the prepared monometallic and bimetallic catalysts highly loaded onto the Al₂O₃ exhibit from 96% to 100% selectivity in the methanation reaction at 250 °C and above. In general, the reaction selectivity increases with increasing the reaction temperature, decreasing the yield of CO to 0%. Under the optimized reaction conditions, 71% and 100% CO₂ conversion and nearly 100% CH₄ selectivity were achieved over 20 wt% Ni₁₀₀/Al₂O₃ and 20 wt%

Co₁₀₀/Al₂O₃ catalysts, correspondingly, with good stability at 350 °C for over 24 h. An increase in the amount of Co (from 20 to 80 wt%) in the bimetallic 20 wt% Co_xNi_{100-x}/Al₂O₃ catalysts leads to an increase in the yield of methane (Table 1). Our findings show the 100% CO₂ conversion to CH₄ in the presence of 20 wt% Co₆₀Ni₄₀/Al₂O₃ and 20 wt% Co₈₀Ni₂₀/Al₂O₃ catalysts at the lowest reaction temperature of 300 °C.

Al₂O₃ and SiC have different physicochemical characteristics, such as *S*_{sp}, temperature stability, and affinity to metal or metal oxide. The catalysts of 20 wt% Co–Ni/SiC series are operated at higher reaction temperatures (Table 2). The tendency to increase the yield of CH₄ stays the same at increasing the reaction temperature and the Co content in the bimetal 20 wt% Co_xNi_{100-x}/SiC catalysts.

Table 1. Parameters for the catalysts of 20 wt% Co–Ni/Al₂O₃ series.

Catalyst	^a <i>S</i> _{sp} (m ² /g)	Reaction temperature (°C)			
		200	250	300	350
		^b Yield, <i>Y</i> _{CH₄} / <i>Y</i> _{CO} (%)			
20 wt% Ni ₁₀₀ /Al ₂ O ₃	68	2/2	60/2	68/2	69/2
20 wt% Co ₂₀ Ni ₈₀ /Al ₂ O ₃	65	5/2	44/2	70/1	83/1
20 wt% Co ₆₀ Ni ₄₀ /Al ₂ O ₃	62	11/2	61/1	100/0	100/0
20 wt% Co ₈₀ Ni ₂₀ /Al ₂ O ₃	58	14/1	69/1	100/0	100/0
20 wt% Co ₁₀₀ /Al ₂ O ₃	52	6/1	58/2	83/0	100/0

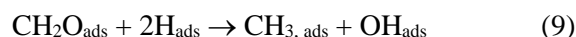
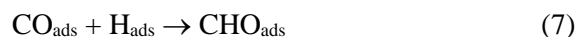
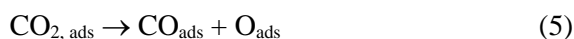
^a*S*_{sp} (Al₂O₃) = 68 m²/g. ^bConversion of CO₂ = *Y*_{CH₄} + *Y*_{CO}.

Table 2. Parameters for the catalysts of 20 wt% Co–Ni/SiC series.

Catalyst	^a <i>S</i> _{sp} (m ² /g)	Reaction temperature (°C)			
		300	350	400	450
		^b Yield, <i>Y</i> _{CH₄} / <i>Y</i> _{CO} (%)			
20 wt% Ni ₁₀₀ /SiC	0.6	0.5/6	4/21	22/29	36/30
20 wt% Co ₂₀ Ni ₈₀ /SiC	1.0	3/9	16/23	66/5	80/1
20 wt% Co ₄₀ Ni ₆₀ /SiC	0.5	3/8	13/20	51/3	86/1
20 wt% Co ₆₀ Ni ₄₀ /SiC	1.0	15/9	81/3	98/1	100/0
20 wt% Co ₈₀ Ni ₂₀ /SiC	2.0	89/1	96/0	98/0	100/0
20 wt% Co ₁₀₀ /SiC	2.0	68/1	82/1	86/1	98/1

^a*S*_{sp} (SiC) = 0.6 m²/g. ^bConversion of CO₂ = *Y*_{CH₄} + *Y*_{CO}.

Approximately 100% CO₂ conversion to CH₄ was achieved on 20 wt% Co₁₀₀/SiC, 20 wt% Co₆₀Ni₄₀/SiC, and 20 wt% Co₈₀Ni₂₀/SiC catalysts at 450 °C. According to Table 2, 20 wt% Ni₁₀₀/SiC, 20 wt% Co₂₀Ni₈₀/SiC, and 20 wt% Co₄₀Ni₆₀/SiC catalysts showed 25–40% selectivity towards CH₄ at 300–350 °C. For 20 wt% Ni₁₀₀/SiC, 20 wt% Co₂₀Ni₈₀/SiC, and 20 wt% Co₄₀Ni₆₀/SiC catalysts, Y_{CO} depends on the reaction temperature and can reach about 20% at 350 °C. Considering available temperature dependencies, we suggest that the dissociation of CO₂ is the methanation limiting step for all studied catalysts. That is why the yield of CH₄ shows a significant increase with increasing temperature, simultaneously reducing the yield of CO. Considering the results of the catalytic test, we suggest that the ratio of Co (60–80%) to Ni (40–20%) in the active complex of catalysts has a positive influence on the performance and promotes the course of surface methanation, regardless of the used carrier. Below, we will point on the main differences in the TD profiles on an example of 20 wt% Co₈₀Ni₂₀/Al₂O₃ and 20 wt% Co₄₀Ni₆₀/SiC catalysts that have higher and lower catalytic activity, correspondingly. Figure 1a shows the typical temperature profiles of particles found after catalysis over high-activity catalysts (Y_{CH₄} ≈ 100% at above 300 °C). Up to 100 °C, we registered intensive desorption of the adsorbed H₂O (m/z 18), CO₂ (m/z 44), and CO (m/z 28). According to Karelovic and Ruiz [13], multiple ways to methanation are known nowadays. Among them, the mechanism presented below is in good agreement with the TD MS data.



As can be seen in Fig. 1a, CO₂, CO, CH₄, CH₃*, and COH* are released simultaneously between 400 and 550 °C. Their thermal desorption peaks are seen at ~450 °C. In our opinion, the dissociation of CO₂ molecules (CO + O) and the formation of CH₄ molecules, as the target product, through intermediates (CH₃* and COH*) [14], take place simultaneously in this temperature range. Therefore, we can assume that the CO₂ methanation reaction over high-activity 20 wt% Co–Ni/Al₂O₃ catalysts proceeds by the substitution of oxygen atoms in CO for hydrogen atoms.

Figure 1b presents the TD profiles of desorbed particles registered after catalysis over the 20 wt% Co₄₀Ni₆₀/SiC catalyst that showed lower activity at medium-temperature CO₂ methanation (Y_{CH₄} ≤ 70% at 300–400 °C). In contrast to the TD profiles of high-activity catalysts, the profile of CO₂ has peaked at 120, 360, and 540 °C. The peaks do not necessarily coincide with thermal desorption peaks of CO and COH*. This is because of the surface coverage with adsorbed CO molecules. As follows from the presented profiles, dissociating CO₂ molecules have saturated the surface layer with CO. Adsorbed CO gradually interacts with adsorbed hydrogen and blocks the surface of loaded metals, slowing down the overall methanation rate [15, 16].

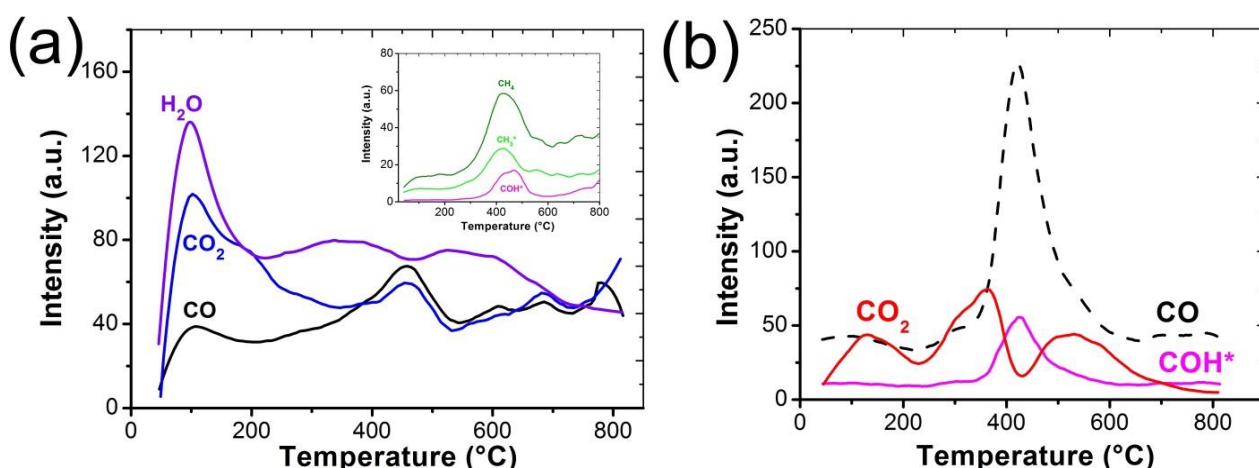


Figure 1. TD profiles of particles adsorbed on (a) 20 wt% Co₈₀Ni₂₀/Al₂O₃ and (b) 20 wt% Co₄₀Ni₆₀/SiC catalysts.

Below, we will consider SEM and XRPD data for the typical representatives of the catalyst series. SEM images of 20 wt% Co₈₀Ni₂₀/Al₂O₃ after catalysis have shown that the agglomerated particles ranged from 10 to 100 microns (Figure 2a).

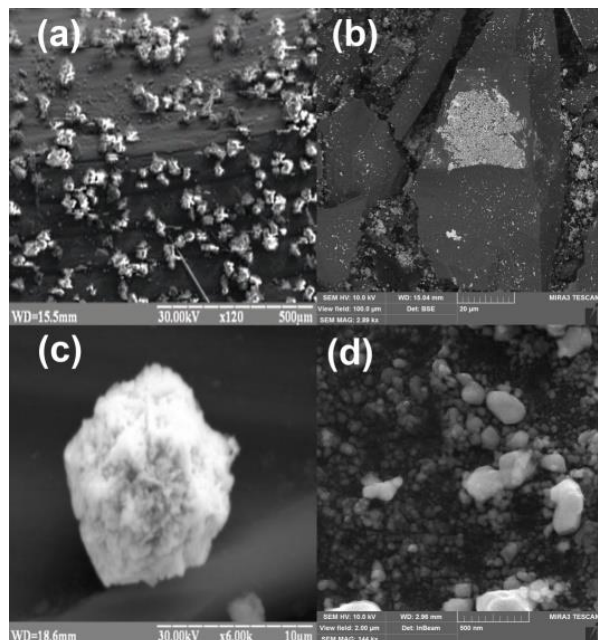


Figure 2. SEM micrographs of (a, c) 20 wt% Co₈₀Ni₂₀/Al₂O₃ and (b, d) 20 wt% Co₈₀Ni₂₀/SiC catalysts, (c, d) micrographs of higher magnification.

Their average size is about 30 microns, and the particles have many grains showing a rough structure of the surface and many cavities. The microanalysis data for 20 wt% Co₈₀Ni₂₀/Al₂O₃ catalyst (53.7 mass% Al, 19.7 mass% O, 20.7 mass% Co and 5.9 mass% Ni) showed that 30% of the active mass is uniformly present on the surface. The ratio between cobalt and nickel is 78:22, which

is practically the same as was calculated. The uniform distribution of the particles of the active mass on the alumina surface has a positive effect on the catalytic activity of 20 wt% Co–Ni/Al₂O₃ in the CO₂ methanation reaction. The wet impregnation used here cannot provide uniform loading of the metal masses on the surface of Al₂O₃. Therefore, the EDX analysis of the Co₈₀Ni₂₀/Al₂O₃ sample shows the surface area with the overstated amount of the loaded Co and Ni metals of 30 wt%.

For the smooth SiC surface (Fig. 2b), the loaded Co and Ni masses are unevenly distributed (the load was varied from 30 to 90 wt%). Particles of size from 50 nm to large agglomerates up to 20 µm are observed. The large agglomerates are composed of volumetric porous particles of 20–300 nm in size. In contrast to the 20 wt% Co–Ni/Al₂O₃ catalysts, the specific surface area of 20 wt% Co–Ni/SiC catalysts is small (Table 2). Figure 3 presents typical XRPD patterns of higher activity catalysts, on the example of Co₈₀Ni₂₀/Al₂O₃ catalyst, and lower activity catalysts, on the example of Co₈₀Ni₂₀/SiC catalyst, studied after the catalytic experiments. Room temperature XRPD patterns were collected for the samples of Co₈₀Ni₂₀/Al₂O₃ and Co₈₀Ni₂₀/SiC catalysts that had worked 10 hours or more in the reaction medium at 300 °C and 450 °C, respectively.

After catalysis, the crystalline phases of corundum Al₂O₃, boehmite γ-AlO(OH), and γ-Al₂O₃ were found in the composition of 20 wt% Co₈₀Ni₂₀/Al₂O₃ and 20 wt% Co₆₀Ni₄₀/Al₂O₃ catalysts. We also registered cobalt oxide (Co₃O₄), hexagonal close-packed phases of Ni and Co metals, and, possibly, of Ni–Co alloys with partial substitution of Co for Ni. Broad reflexes of the Co₃O₄ are typical for nanometer-sized particles.

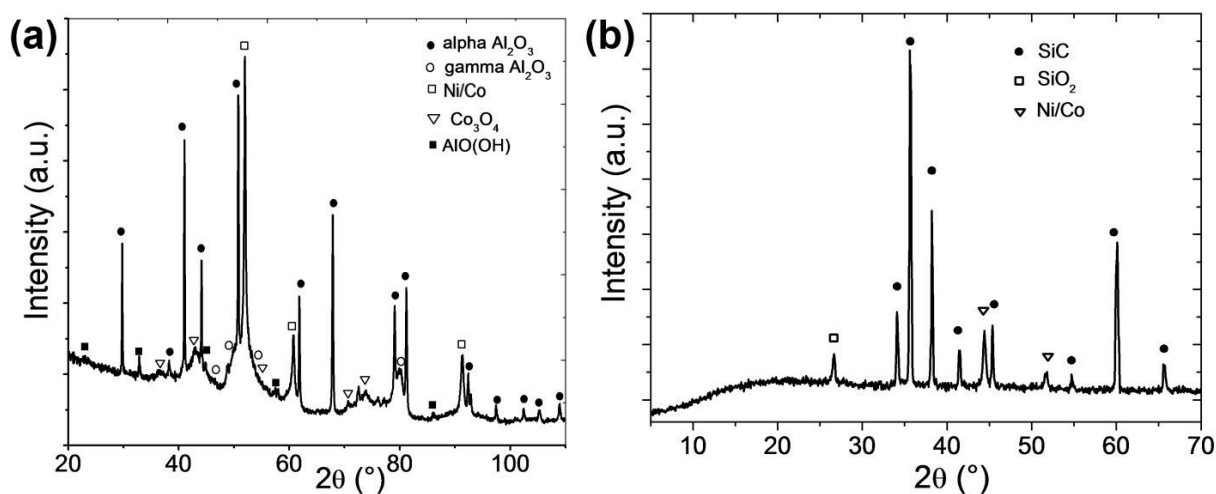


Figure 3. XRPD patterns of (a) 20 wt% Co₈₀Ni₂₀/Al₂O₃ and (b) 20 wt% Co₈₀Ni₂₀/SiC catalysts.

Narrow and very intensive reflexes of metals indicate large crystallite sizes. Metallic nickel and cobalt and their solid solutions have similar crystal structures. For this reason, it is almost impossible to separate the overlapping peaks for the observed diffraction pattern (Fig. 3a). High dispersion of the carrier can provoke the formation of amorphous cobalt metal at the stage of catalyst preparation. At the final stage of the catalyst preparation, the oxides of nickel and cobalt and their mixtures are reduced with hydrogen in the reactor immediately before the catalytic experiment. Therefore, one can assume that the catalyst surface during the course of CO₂ methanation is free of metal oxides. After a catalytic experiment, the reflexes of the Co₃O₄ phase, which appears, perhaps, because of surface passivation, were registered in the diffraction pattern of the 20 wt% Co₆₀Ni₄₀/Al₂O₃ catalyst. In the reaction medium, metallic nickel (in the micrometric particles) has lower oxygen reduction ability and oxidizes slower than metallic cobalt. That is why the reflexes related to the NiO phase are absent in the diffraction pattern.

For 20 wt% Co₈₀Ni₂₀/SiC catalysts, one can see crystalline phases of SiC, Ni/Co metal, and SiO₂, assuming the latter as the product of SiC oxidation (Figure 3b). Carborundum SiC has a geometric surface area, which value is much lower than that of the alumina, and, consequently, this carrier has an insignificant amount of functional surface groups. That is why microcrystals of metallic Ni and Co loaded on such an inert carrier are not subjected to deep oxidation when working in the reaction mixture.

CONCLUSIONS

From the results of the present study, we can draw the following conclusions about the behavior of methanation catalysts: the operating temperatures of 20 wt% Co–Ni/Al₂O₃ catalysts are much lower than those of the 20 wt% Co–Ni/SiC catalysts. The uniform distribution of the active Co–Ni metal mass on the surface of alumina increases the accessibility of active catalyst centers for the course of CO₂ methanation. An additional factor that, in our opinion, contributes to the methanation efficiency is the intensive microheterogeneity in the composition of the loaded Co–Ni active phase. Although the efficiency of 20 wt% Co₈₀Ni₂₀/SiC catalysts is lower than that

of the 20 wt% Co₈₀Ni₂₀/Al₂O₃ catalysts, the latter provides better performance (100% conversion of CO₂ to CH₄) unlike the massive Co₈₀Ni₂₀ metallic catalyst giving the maximum methane yield of only 65% at above 450 °C [17]. For the Co-rich, high activity catalysts, the thermal desorption peaks for particles taking part in the CO₂ methanation reaction and adsorbed on the active sites are registered at the same temperature. The presence of CHO* formate intermediate registered for the studied catalysts confirms that the reaction takes place *via* intermediates under softer conditions and at a faster rate, which is the reason for the highest activity of the Co-rich bimetallic Co–Ni catalysts.

REFERENCES

1. W. Wang, S. Wang, X. Ma, J. Gong, *Chem. Soc. Rev.*, **40**, 3703 (2011).
2. T. A. LeJong, K. Kang, E. D. Park, *Top. Catal.*, **15-17**, 1537 (2018).
3. C. Liu, T. R. Cundari, A. K. Wilson, *J. Phys. Chem. C*, **116**, 5681 (2012).
4. M. Zhudenko, A. Dyachenko, O. Bieda, S. Gaidai, M. Filonenko, O. Ischenko, *Acta Phys. Polonica A*, **133**, 1084 (2018).
5. S. Hwang, J. Lee, U. G. Hong, J. H. Baik, D. J. Koh, H. Lim, I. K. Song, *Catal. Lett.*, **142**, 860 (2012).
6. S. Rahmani, M. Rezaei, F. Meshkani, *J. Ind. Eng. Chem.*, **20**, 1346 (2014).
7. M. J. Ledoux, C. Pham-Huu, *CATTECH*, **5**, 226 (2001).
8. M. Feyzi, A. Babakhanian, M. B. Gholivand, *Korean J. Chem. Eng.*, **31**, 37 (2014).
9. S. Carencu, C.-H. Wu, A. Shavorskiy, S. Alayoglu, G. A. Somorjai, H. Bluhm, *Small*, **11**, 3045 (2015).
10. D. Beierlein, D. Häussermann, M. Pfeifer, T. Schwarz, K. Stöwe, Y. Traa, E. Klemm, *Appl. Catal. B: Environ.*, **247**, 200 (2019).
11. R. Meshkini Far, O. V. Ishchenko, A. G. Dyachenko, O. Bieda, et al., *Funct. Mater. Lett.*, **11**, art. no. 1850057 (2018).
12. V. L. Veselovskyi, E. V. Ischenko, S. V. Gayday, V. V. Lisnyak, *Catal. Commun.*, **18**, 137 (2012).
13. A. Karelovic, P. Ruiz, *J. Catal.*, **301**, 141 (2013).
14. I. A. Fisher, A. T. Bell, *J. Catal.*, **162**, 54 (1996).
15. V. K. Yatsimirsky, V. L. Budarin, V. E. Diyuk, L.Y. Matzui, M. I. Zacharenko, *Adsorpt. Sci. Technol.*, **18**, 609 (2000).
16. A. V. Puga, *Catal. Sci. Technol.*, **8**, 5681 (2018).
17. O. V. Ishchenko, A. G. Dyachenko, A. V. Yatsymyrskiy, T. M. Zakharova, et al., *E₃S Web Conf.*, **154**, 02001 (2020).

Toxic solvent-free: Radical polymerizations of vinyl monomers using a di-site phase-transfer catalyst – a kinetic approach

M. Meena*, M. J. Umapathy

*R.M.K. Engineering College, Kavaraipettai-601206, Tiruvallur District, Tamil Nadu, India
Anna University, Chennai 600025, Tamil Nadu, India*

Received: June 17, 2019; Revised: March 12, 2020

Free radical polymerizations of vinyl monomers, namely methyl methacrylate and ethyl methacrylate, were performed using 1,1,4,4-tetramethyl-1,4-dioctylethylenediammonium bromide (TDEDDB) which is a newly synthesized di-site phase-transfer catalyst (PTC), in ethyl acetate/water as a biphasic medium. The catalyst was characterized by Fourier-transform infrared, $^1\text{H-NMR}$, and $^{13}\text{C-NMR}$ spectroscopies along with C, H, and N elemental analyses. Polymerization was initiated using the water-soluble potassium peroxydisulfate initiator at a constant temperature of 60 ± 1 °C. The competency of TDEDDB was examined in a kinetic study. The reaction orders with respect to the monomer, PTC and initiator were determined. The effect of ionic and acid strengths and solvent polarity were also investigated. A suitable mechanism was proposed on the basis of the experimental conditions. The molecular weights of the poly(methyl methacrylate) and poly(ethyl methacrylate) were determined by gel permeation chromatography.

Keywords: Di-site phase-transfer catalyst; 1,1,4,4-Tetramethyl-1,4-dioctylethylenediammonium bromide; Mechanism; Radical polymerization; Potassium peroxydisulfate

INTRODUCTION

Reactions between inaccessible reactants present in heterogeneous phases are made possible through the use of phase-transfer catalysts (PTCs) which are powerful tools. The introduction to these highly active, interface-penetrating PTCs by Starks [1] in 1971 led to tremendous transformations in synthetic chemistry. This versatile and reliable synthetic methodology has garnered attention in chemical industries because of its affordability, trivial reaction conditions, high conversions or yields, lack of byproducts, purging of excessive and dangerous non-ecofriendly solvents that dissolve the reactants in a single phase, solvent-selection flexibility, and ability to easily treat wastewater streams [2–4]. Hence, these robust catalysts have emerged as an area of research thrust, especially in organic synthesis and polymer chemistry. Phase-transfer-catalyzed polymerization reactions have facilitated the use of water and reduced or eliminated the usage of non-ecofriendly organic solvents. The transportation of aqueous-phase-soluble inorganic reactants across the boundary in a heterogeneous aqueous–organic solvent system using a PTC was first reported by Makosza [5]. This motivated the researchers to investigate the use of single-site and multi-site PTCs, especially in the free radical polymerizations of vinyl monomers in aqueous–organic biphasic media [6–18]. Success in this chemistry motivated us to investigate the competency of a newly synthesized di-site PTC in

the radical polymerizations of methyl and ethyl methacrylates, which were analyzed in a kinetic study using a water-soluble potassium peroxydisulfate initiator.

EXPERIMENTAL

Materials and Methods

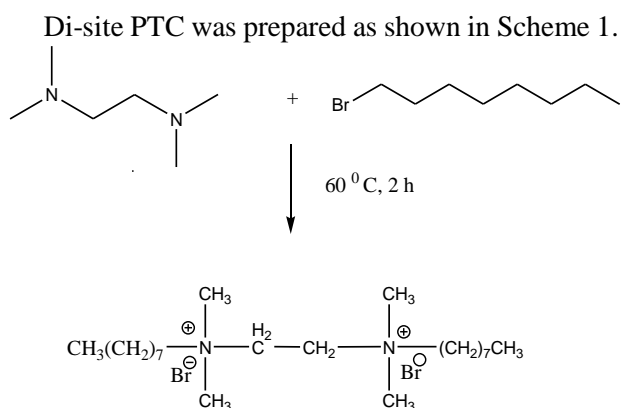
Methyl methacrylate (MMA) and ethyl methacrylate (EMA) (Merck, Mumbai) were distilled at reduced pressure prior to use. The PDS water-soluble initiator (SRL, Mumbai), was used as received. Methanol (SRL, Mumbai) and ethyl acetate (SRL, Mumbai) were distilled before use. Doubly distilled water was used as the solvent in the biphasic system.

Instrumentation

The FT-IR spectra were recorded on a Perkin Elmer Spectrum RX I spectrometer in the 4400–400 cm^{-1} spectral region using the KBr-disc method. High-resolution $^1\text{H-NMR}$ and $^{13}\text{C-NMR}$ spectra were recorded on Bruker 500 MHz and DRX 125.77 MHz FT-NMR spectrometers at room temperature using D_2O as the solvent. The molecular weight of the polymer was determined by gel permeation chromatography (GPC) using a Waters 501 instrument, with styragel column and tetrahydrofuran as the eluent. Polystyrene standards were employed for calibration.

* To whom all correspondence should be sent:
E-mail: mm.sh@rmkec.ac.in

Synthesis of Di-site PTC: 1,1,4,4-Tetramethyl-1,4-dioctylethylenediammonium bromide



Scheme 1. Synthesis of TDEDDB

A solution of 0.01 M N,N,N',N'-tetramethylethylenediamine and 0.02 M 1-bromooctane was introduced into a 250-mL flask. The mixture was gently refluxed at 60 °C for 2 h. The resulting white 1,1,4,4-tetramethyl-1,4-dioctylethylenediammonium bromide (TDEDDB) precipitate was collected by filtration, dried and then purified by dissolving it in a minimal amount of acetone/ethanol. The melting point of the prepared TDEDDB was found to be 173 °C.

FT-IR Spectral Analysis of TDEDDB

The FT-IR spectrum of TDEDDB (Fig. 1) displays the following signals: 3112 cm⁻¹ (C–H stretches of the methyl groups attached to the positively charged nitrogen atoms), 2966 and 2838 cm⁻¹ (symmetric and asymmetric stretches of the methyl and methylene groups, respectively), 1488 and 1397 cm⁻¹ (CH₂–N and CH₃–N stretches, respectively), and 932 cm⁻¹ (CH₂-group rocking).

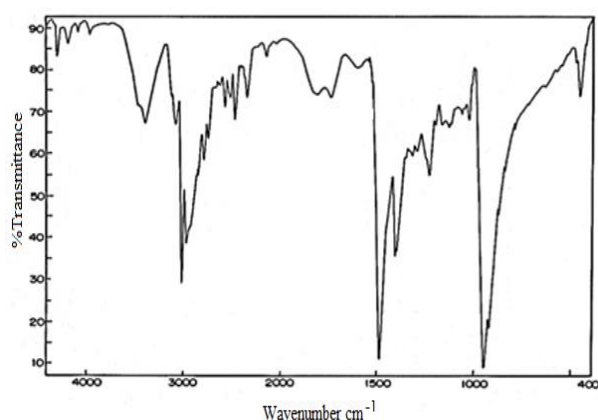


Fig. 1. FT-IR spectrum of TDEDDB

¹H-NMR Spectrum of TDEDDB

The ¹H NMR spectrum of TDEDDB is shown in

Fig. 2 and exhibits the following signals: 2.78 ppm (ethylene protons), 2.45 ppm (methylene protons of the octyl groups attached to the nitrogen atoms), 2.21 ppm (protons of the methyl groups attached to the nitrogen atoms), 1.79 and 1.18 ppm (remaining methylene protons of the octyl groups), and 0.99 ppm (methyl protons of the octyl groups).

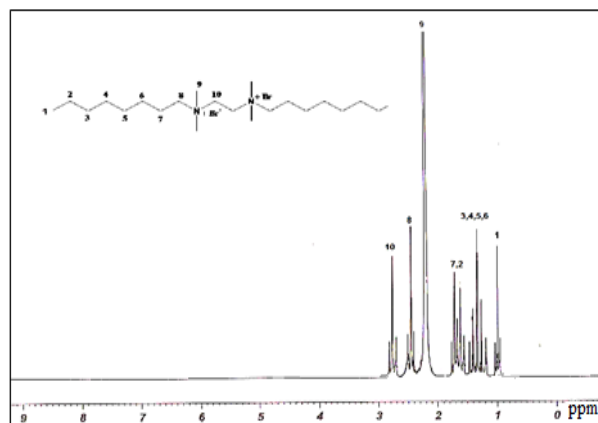


Fig. 2. ¹H NMR spectrum of TDEDDB

¹³C-NMR Spectrum of TDEDDB

The ¹³C-NMR spectrum of TDEDDB is presented in Fig. 3, which displays the following signals: 61.55 and 61.49 ppm (methylene carbons of the octyl groups and those of the ethylene groups attached to the nitrogen atoms, respectively), 46.06 ppm (methyl carbons attached to the nitrogen atoms), 14.02 ppm (methyl carbons of the octyl groups), and 32.53, 30.02, 28.32, 27.24, and 23.13 ppm (remaining methylene carbons of the octyl groups).

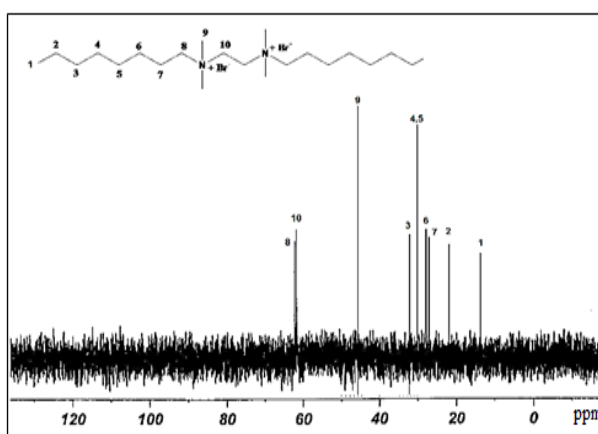


Fig. 3. ¹³C-NMR spectrum of TDEDDB

Elemental Analysis of TDEDDB

The C, H, and N contents of TDEDDB were determined and found to be very close to the theoretical values. Molecular formula: C₂₂H₅₀Br₂N₂;

Mol. wt. 502; Elemental analysis (%): C: 52.52 (found): 52.59 (calculated), H: 10.09 (found): 10.03 (calculated), N: 5.54 (found): 5.58 (calculated).

Polymerization Procedure

Methyl methacrylate and ethyl methacrylate (RMA) were polymerized in a classic manner in thick-walled, long, sealed Pyrex tubes without stirring in an inert atmosphere at 60 ± 1 °C. The reaction mixture was composed of the monomer in 10 mL of the organic phase (ethyl acetate), the phase-transfer catalyst (TDEDDB), sodium bisulfate (0.5 M) to control the ionic strength, and sulfuric acid (0.2 M) to control the pH of the 10-mL aqueous phase. Polymerization was initiated by the addition of PDS to the reaction mixture. After the stipulated period of time, the reaction was terminated by pouring the reaction mixture into ice-cold methanol [6-10,11,14]. The precipitated polymer was collected by filtration using a sintered glass crucible, washed several times with doubly distilled water and methanol, and then dried in an oven (60 ± 0.1 °C) to constant weight. The rate of polymerization (R_p) was calculated using equation (1):

$$R_p = \frac{1000 \times W}{V \times t \times M} \quad (1)$$

where R_p is the rate of polymerization, W is the weight of the polymer (g), V is the volume of the reaction mixture, t is the reaction time (s), and M is the molecular weight of the monomer.

RESULTS AND DISCUSSION

Kinetics of Free Radical Polymerization

Polymerization is discussed in terms of the kinetics of the free radical polymerizations of methyl and ethyl methacrylate using TDEDDB as the catalyst and PDS as the initiator in ethyl acetate/water as the biphasic medium under the experimental conditions described below.

Steady-state Polymerization Rates

The rates of monomer polymerization were determined at monomer concentrations of 2.0 M and a PDS concentration of 0.02 M in a total volume (aqueous + organic phase) of 10 mL; sulfuric acid (0.2 M), and sodium bisulfate (0.5 M) were also added. Furthermore, polymerization was initiated by adding 0.1 M TDEDDB into the aqueous phase. Fig. 4 displays the relationships between polymerization rates and time. The steady-state rates of polymerization were determined from these plots at 50 min for both MMA and EMA with TDEDDB as the PTC.

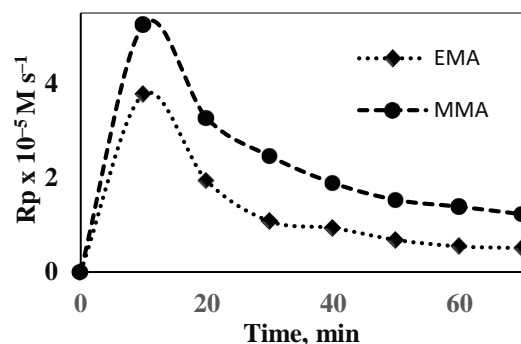


Fig. 4. Steady-state rates of polymerization (R_p) catalyzed by TDEDDB as functions of time.

Impact of Monomer Concentration on the Rate of Polymerization

The dependence of polymerization rate on monomer concentration was determined by varying its concentration from 0.8 to 1.8 M while maintaining the concentration of PDS at 0.02 M and of TDEDDB at 0.1 M, with the ionic strength maintained at 0.5 M at a constant pH. We observed that R_p increased with increasing monomer concentration. The reaction orders with respect to the MMA and EMA monomer concentrations are almost one half, which contrasts with the first-order reactions observed for vinyl monomers. The observed deviation from first order [19-21] has been attributed to primary-radical termination and occlusion phenomena, or gelation effects during the initiation step. But in the present case, deviation may be due to the formation of a charge-transfer complex with the oxygen of PDS, hence this would have hampered the reactivity of the monomer. The increase in viscosity of the medium also restricted the diffusion of ions [22, 23]. Fig. 5 shows the plots of R_p as a function of monomer concentration raised to suitable powers such that the straight lines pass through the origin in each case; these plots confirm the above observations with respect to [RMA].

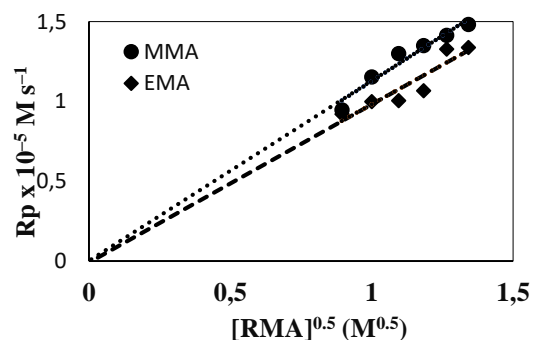


Fig. 5. Rate of polymerization (R_p) as a function of $[RMA]^{0.5}$

Effect of TDEDDB Concentration on the Rate of Polymerization

By keeping the concentration of the other factors constant, the effect of TDEDDB on R_p was determined in the 0.015–0.025 M concentration range. The plot of $\log R_p$ vs. $\log [TDEDDB]$ is linear with a slope of 0.5 for EMA, signifying a half-order dependence. However, for the polymerization of MMA, the order is almost equal to unity under the same catalyst conditions. The plots of R_p vs. $[TDEDDB]$ (Figs. 6 and 7) are linear and pass through their respective origins, which supports the above observations. The results show a lack of polymerization in the absence of the catalyst even after several hours. Moreover, the first-order

d
e
p

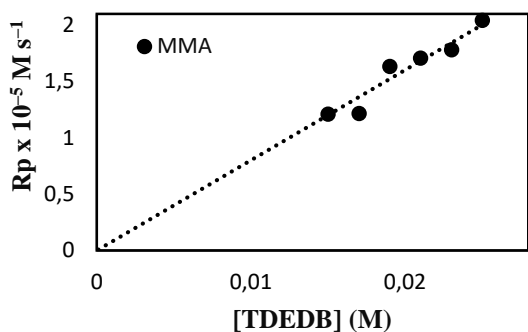


Fig. 6. Rate of polymerization (R_p) as a function of $[TDEDDB]$ for MMA

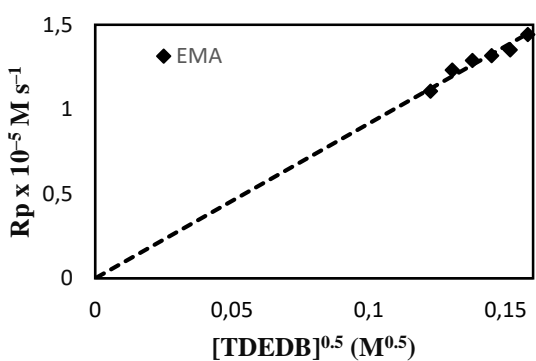


Fig. 7. Rate of polymerization (R_p) as a function of $[TDEDDB]^{0.5}$ for EMA

v
i
o
u
s
l
y

b
e
e
n

Effect of Initiator Concentration on the Rate of Polymerization

The effect of concentration of $K_2S_2O_8$ on the rate of polymerization of RMA was studied by varying the concentration of $K_2S_2O_8$ in the range of 0.015 to 0.025 M by keeping other concentrations constant. As the concentration of PDS was increased, R_p was found to increase. The plot of $\log R_p$ versus $\log [PDS]$ and the order of reaction are found to be nearly unity for MMA and nearly half-order for EMA. Figs. 8 and 9 show that the plot of R_p versus $[PDS]$ raised to suitable power passes through the origin, supporting the above observation. The normal half-order dependence of the rate on initiator concentration which is observed in most of the free radical polymerization has been deviated for MMA.

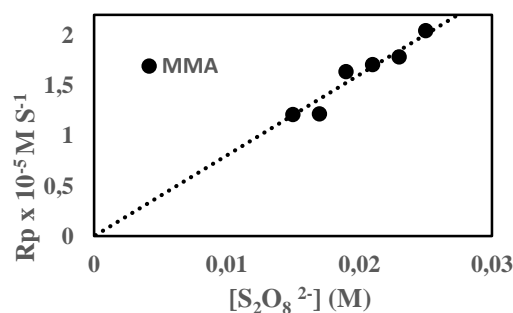


Fig. 8. Rate of polymerization (R_p) as a function of $[S_2O_8]$ for MMA

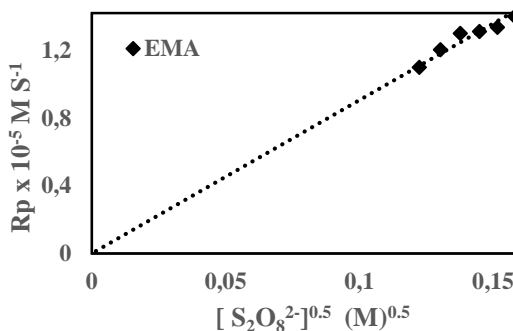


Fig. 9. Rate of polymerization (R_p) as a function of $[S_2O_8]^{0.5}$ for EMA

In the case of free radical polymerization of vinyl monomers, the order with respect to initiator is found to be a square root of initiator concentration when the polymer radical terminates by mutual bimolecular reaction. The higher order of polymerization in the case of MMA may be due

either to the induced decomposition of the initiator or to the decrease in termination rate constant. The induced decomposition of peroxydisulphate in the presence of oxidizable organic compounds is well known. The decomposition of PDS in water was greatly enhanced [26-28] in the presence of methanol, ethanol, ethyl acetate, etc.

Effect of Ionic Strength and Acid Strength

The effect of ionic strength varied in the range from 0.4 to 0.6 M and acid strength from 0.1 to 0.3 M on the rate of polymerization was studied by maintaining constant concentrations of monomer, initiator, PTC and solvent. It was observed that there were no significant changes in the rate of polymerization [11, 13-15, 29].

Effect of Solvent Polarity on the Rate of Polymerization

MMA and EMA were polymerized using three different solvents, namely cyclohexane, ethyl acetate, and cyclohexanone, whose dielectric constants are 2.02, 6.02, and 18.03, respectively. The rates of polymerization were found to increase in the order:

cyclohexane < ethyl acetate < cyclohexanone.

Fig. 10 displays the influence of the polarity (dielectric constant) of the solvent on the rate of polymerization. We observed that the dielectric constant of the medium increases the rate of polymerization, which is attributable to the greater migration of sulfate ions into the organic phase with increasing solvent polarity [12,14, 30].

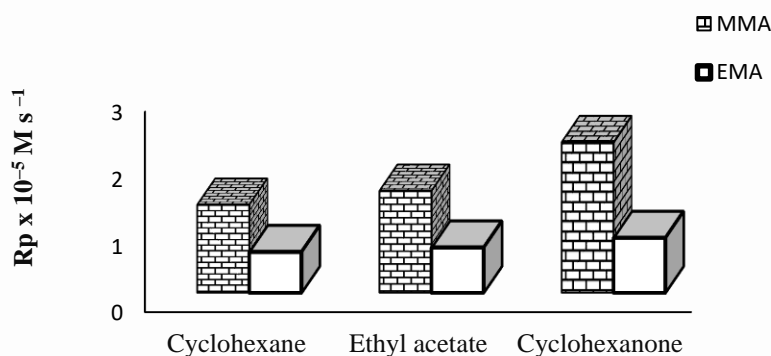


Fig. 10. Effect of solvent polarity on Rp

Table 1. Mn, Mw, and Mw/Mn of polymers

1. Polymer	M _n	M _w	M _w /M _n
PMMA – L	37276	57685	1.547
PMMA – H	53437	102534	1.919
PEMA – L	17212	27815	1.616
PEMA – H	37805	62118	1.643

Determining the Molecular Weights of the Poly(alkyl methacrylate)s

The molecular weights of the polymers were established by gel permeation chromatography. The number-average molecular weight (M_n), weight-average molecular weight (M_w), and polydispersity index (M_w/M_n) of each polymer are presented in Table 1. The molecular weights of the polymers which were synthesized at low monomer concentrations and fixed concentrations of the PTC and PDS are referred to as “poly(alkyl methacrylate - L)”, while those synthesized at higher monomer concentrations and fixed initiator and PTC concentrations are referred to as “poly(alkyl

methacrylate - H)”. The polydispersity index values of both poly(methyl methacrylate) (PMMA) and poly(ethyl methacrylate) (PEMA) suggest that chains are terminated predominantly through disproportionation [30–32]. The molecular weight of PMMA was found to consistently be higher than that of PEMA, which is attributable to chain-propagation difficulties during the polymerization of EMA compared to MMA. In this study, we observed that the molecular weights of the polymers increased with increasing monomer concentration.

Product Analysis

The FT-IR spectra of the products obtained by the phase-transfer polymerization of MMA and EMA revealed the absence of the peak at 1635 cm⁻¹ originally present in the FT-IR spectra of the monomers. This suggests that the olefinic double bond was involved in the polymerization process, and that the products are PMMA and PEMA, respectively.

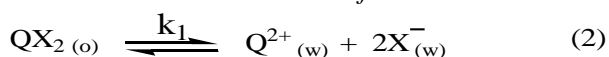
Mechanism

The following observations were made during the free radical polymerizations of the alkyl methacrylates using K₂S₂O₈ as the initiator and the di-site quaternary ammonium salt, TDEDDB, as the PTC:

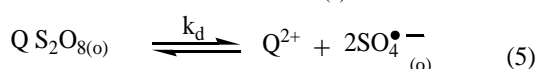
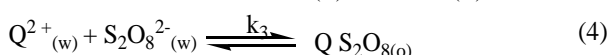
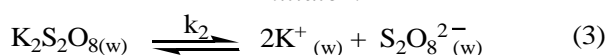
- The reaction exponent with respect to [monomer] = 0.5–1;
- The reaction order with respect to [TDEDDB] = 0.5–1;
- The reaction order with respect to [K₂S₂O₈] = 0.5 to 1;
- R_p increases with increasing solvent polarity;
- The rate of polymerization is independent of ionic strength (μ) and [H⁺].

We propose an appropriate mechanism to explain the above-mentioned experimental observations. Scheme 2 displays a pathway for the polymerization of an alkyl methacrylate (M) initiated by K₂S₂O₈/PTC in an ethyl acetate/water biphasic system. Subscripts (w) and (o) refer to aqueous and organic phases, respectively, while k₁, k₂ and k₃ are equilibrium constants of equations (2) to (4); k_d is the dissociation constant of equation (5); k_i, k_p, and k_t are the rates of initiation, propagation, and termination, respectively, and QX₂ represents the PTC.

Phase Transfer:



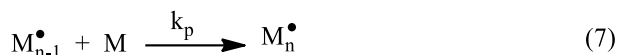
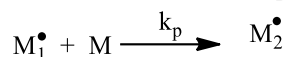
Initiator:



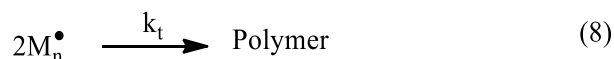
Initiation:



Propagation:



Termination:



Scheme 2. Mechanism proposed for the polymerization of an alkyl methacrylate initiated by K₂S₂O₈/PTC in an ethyl acetate/water biphasic system.

Based on this mechanism, the rate of polymerization for RMA catalyzed by TDEDDB can be derived to be:

$$R_p = k_p \left[\frac{k_d K}{k_t} \right]^{1/2} [Q^{2+}]^{0.5} [S_2O_8^{2-}]^{0.5} M^{0.5}$$

This derived expression sufficiently explains all experimental observations.

CONCLUSION

The kinetics of the free radical polymerizations of alkyl methacrylates initiated by K₂S₂O₈ was studied using a newly synthesized di-site PTC in an ethyl acetate/water biphasic medium under inert conditions. The rates of polymerization were evaluated by increasing the concentrations of the monomer, PTC and initiator. The reaction orders were found to be 0.5 with respect to monomers, 0.5–1 with respect to initiator and di-site PTC. Based on the results obtained, a suitable mechanism was proposed. The effects of ionic and acid strengths, as well as of solvent polarity were also determined. Insignificant changes were observed by the increase of ionic and acidic strengths but polarity of the solvents played a significant role in increasing the rate of polymerization. The molecular weight of polymers was found to be higher at higher monomer concentrations and at fixed initiator and PTC concentrations. Hence, the synthesized PTC promotes higher polymerization rates in the ethyl acetate/water biphasic system using a water-soluble initiator. In addition, the newly synthesized PTC is expected to be applied to organic reactions, such as alkylation, oxidation, reduction, hydrolysis, etherification, and esterification, among others; hence the hidden potential of this PTC needs to be further explored.

REFERENCES

1. C. M. Starks, *J. Am. Chem. Soc.*, **93**, 195 (1971).
2. E. V. Dehmlow, S. S. Dehmlow, *Phase Transfer Catalysis*, VCH, Weinheim, 1993.
3. C. M. Starks, C. Liotta, *Phase Transfer Catalysis*:

- Principles and Techniques, Academic Press, New York, 1978.
- V. W. P. Weber, G. W. Gokel, Phase Transfer Catalysis in Organic Synthesis, Springer-Verlag, New York, 1977.
 - M. Makosza, *Pure Appl. Chem.*, **43**, 439 (1975).
 - M. J. Umapathy, T. Balakrishnan, *J. Polym. Mater.*, **15**, 275 (1998).
 - M. J. Umapathy, D. Mohan, *Hung. J. Ind. Chem.*, **27**, 245 (1999).
 - M. J. Umapathy, D. Mohan, *J. Polym. Mater.*, **16**, 167 (1999).
 - M. J. Umapathy, R. Malaisamy, D. Mohan, *J. Macromol. Sci. Pure Appl. Chem.*, **37**, 1437 (2000).
 - M. J. Umapathy, D. Mohan, *Ind. J. Chem. Tech.*, **8**, 510 (2001).
 - M. Meena, S. Nanjundan, M. J. Umapathy, *IJAER*, **11**, 2177 (2016).
 - K. M. Dharmendira, T. P. Konguvel, M. J. Umapathy, M. Rajendran, *Int. J. Polym. Mater.*, **53**, 95 (2004).
 - S. Savitha, M. Vajjiravel, M. J. Umapathy, *Int. J. Polym. Mater.*, **55**, 537 (2006).
 - M. Vajjiravel, M. J. Umapathy, *Colloid Polym. Sci.*, **286**, 729 (2008).
 - J. Usha, M. J. Umapathy, *Int. J. Polym. Mater. Polym. Biomater.*, **58**, 409 (2009).
 - P. A. Vivekanand, T. Balakrishnan, *Catal. Commun.*, **10**, 687 (2009).
 - K. M. Mustaque, S. Jayakumar, T. K. Shabeer, *J. Chem. Biol. Phys. Sci.*, **2**, 601 (2012).
 - J. P. Idoux, R. Wysocki, S. Young, J. Turcot, C. Ohlman, R. Leonard, *Synth. Commun.*, **13**, 139 (1983).
 - G. M. Burnett, P. Evans, H. W. Melville, *Trans. Faraday Soc.*, **49**, 1096 (1953).
 - G. M. Burnett, P. Evans, H. W. Melville, *Trans. Faraday Soc.*, **49**, 1105 (1953).
 - G. M. Burnett, G. G. Cameron, M. M. Zafar, *Eur. Polym. J.*, **6**, 823 (1970).
 - M. Vajjiravel, M. J. Umapathy, *J. Polym. Res.*, **15**, 235 (2008).
 - A. K. Bajpai, R. Dengre, *Indian J. Chem.*, **40A**, 831 (2001).
 - T. Balakrishnan, N. Jayachandramani, *J. Macromol. Sci. A.*, **31**, 847 (1994).
 - J. Usha, P. Shymalavathy, M. J. Umapathy, *Int. J. Polym. Mater.*, **58**, 99 (2009).
 - M. Ueda, S. Shouji, T. Ogata, M. Kamachi, C. U. Pittman, *Macromolecules*, **17**, 2800, (1984).
 - P. D. Bartlett, J. D. Catman, *J. Am. Chem. Soc.*, **71**, 1419 (1949).
 - I. M. Kolthoff, I. K. Miller, *J. Am. Chem. Soc.*, **73**, 3055 (1951).
 - J. Prabha, W. Susan Jemima, M. Jayaprada, M. J. Umapathy, *Ultrason. Sonochem.*, <http://dx.doi.org/10.1016/j.ultsonch.2016.10.011>.
 - A. W. Herriott, D. Picker, *J. Am. Chem. Soc.*, **97**, 2345 (1975).
 - H. W. Melville, B. Noble, W. F. Watson, *J. Polym. Sci.*, **4**, 629 (2003).
 - S. Teramachi, A. Hasegava, M. Akatsuka, A. Yamashita, N. Takemoto, *Macromolecules*, **11**, 1206 (1978).

Gravitational instability of a rotating streaming plasma cloud with radiation

A. A. Hasan

Basic and Applied Sciences Department, College of Engineering and Technology, Arab Academy for Science, Technology and Maritime Transport (AASTMT), Sadat Road - P.O. Box 11, Aswan, Egypt

Received January 27, 2019; Revised: July 18, 2020

The gravitational instability of an inviscid compressible rotating streaming plasma cloud with radiation is investigated. The self-gravitating force is destabilizing while the rotating force has a stabilizing influence under certain restrictions. The radiation has a strong stabilizing influence for all modes of perturbations. In the presence of radiation, the uniform streaming has no influence at all on the instability of the model and the radiation overcomes the self-gravitating instability of a plasma cloud. Stability of fluid layers or cylinders has gained considerable importance because of their applications in industries and chemical laboratories, such as medical applications of electrohydrodynamic and magnetohydrodynamic stabilities as injection of drugs inside the vessels, electric shock to treat heart attack and effect of magnetic resonance on blood flow.

Keywords: Self-gravitating, Radiation, Rotating, Plasma cloud.

INTRODUCTION

It is well known since long time ago (Jeans [1]) that a self-gravitating fluid becomes unstable with respect to small perturbations if the related wavelength exceeds a certain value. In this case the gravitational force overpowers the pressure gradient and the instability set in this process clearly plays a basic role in the initial stage of a stellar cluster formation from fragmentation of interstellar matter. It is found that the model becomes unstable for all perturbations of wave numbers less than a critical value $k^2 C_s^2 - 4\pi G \rho_o < 0$, called Jeans' criterion, where k is the net wave number of the propagated wave, C_s^2 is the sound speed in the fluid of density ρ_o , and G is the self-gravitational constant. Chandrasekhar and Fermi [2], and later on Chandrasekhar [3] made several extensions. The Jeans' model of self-gravitational medium has been elaborated with streams of variable velocity distribution by Sengar [4]. Hasan [5] has investigated the magnetodynamic stability of a fluid jet pervaded by a transverse varying magnetic field. In 2013 Kormendy and Ho [6] have analyzed the stability of the observed clumps considering that a criterion is required. However, the conventional Jeans' criterion and Roche limit become insufficient, because they regard self-gravity as the only force binding a gas cloud, which is not true in galactic nuclei. Chen *et al.* [7] have formulated a new scheme for judging the stability of the observed clumps and proved that these clumps are stable, contrary to what one would naively deduce from the

Roche (tidal) limit. Hasan [8] has studied the linear stability of self-gravitating compound dielectric immiscible jets under the influence of an axial electric field. He [9] developed the magnetohydrodynamic stability of a self-gravitating rotating streaming viscous fluid medium pervaded by a general magnetic field. He [10] discussed the stability of the interface between two incompressible self-gravitating non-conducting fluids in the presence of an electric field. Hoshoudy *et al.* [11] investigated the compressibility effects on the Rayleigh-Taylor instability of two plasma layers. Morimoto *et al.* [12] clarified theoretically the suppression of three-dimensional (3D) nucleation by microscopic magnetohydrodynamic flow and formation of stream pattern of macroscopic MHD flow by the multiple nucleation of 3D nuclei in electrodeposition under a uniform parallel magnetic field. In 2019 they [13] have established the amplitude of the micro-MHD flows and concentration fluctuation on the solution side independent of the fluctuation on the electrode-surface side. Weyens *et al.* [14] have presented new expressions for the quantities of interest, namely the parallel current density, the local shear and the normal and geodesic components of the curvature. In this present work the effect of radiation on the self-gravitating instability of a rotating plasma cloud with streams of variable velocity distribution function of coordinate is discussed. There are many applications of electrohydrodynamic and magnetohydrodynamic stability in several fields of science such as:

Geophysics: the fluid of the core of the Earth and was theorized to be a huge MHD dynamo that

* To whom all correspondence should be sent:
E-mail: alfaisal772001@aast.edu

generates the Earth's magnetic field because of the motion of the liquid iron.

Astrophysics: MHD applies quite well to astrophysics since 99% of baryonic matter content of the universe is made of plasma, including stars, interplanetary medium, nebulae and jets, spiral arms of galaxies, etc. Many astrophysical systems are not in local thermal equilibrium, and therefore require an additional kinematic treatment to describe all the phenomena within the system.

Engineering applications: there are many applications in engineering sciences including oil and gas extraction processes surrounded by electric field or magnetic field, gas and steam turbines, MHD power generation systems and magneto-flow meters,

$$\rho \left(\frac{\partial \underline{u}}{\partial t} + (\underline{u} \cdot \nabla) \underline{u} \right) = -\nabla P + \rho \nabla V - 2\rho (\underline{u} \wedge \underline{\Omega}) + \frac{1}{2} \rho (\underline{\Omega} \wedge \underline{r})^2 \quad (1)$$

$$\frac{\partial \rho}{\partial t} + (\underline{u} \cdot \nabla) \rho = -\rho (\nabla \cdot \underline{u}) \quad (2)$$

$$\nabla^2 V = -4\pi G \rho \quad (3)$$

$$P = K \rho^\Gamma \quad (4)$$

Radiating equation of state:

$$\rho \frac{\partial T}{\partial t} - (\Gamma - 1) T \frac{\partial \rho}{\partial t} = 0 \quad (5)$$

Here ρ and \underline{u} are the fluid density, velocity vector, V and G are the self-gravitating potential and constant, $\underline{\Omega}$ is the angular velocity of rotation, K and Γ are constants where Γ is the polytropic exponent,

$$P_g = R \rho T \quad (6)$$

$$P_r = \frac{1}{3} a_R T^4 \quad (7)$$

where a_R is the Boltzmann constant and R is the general constant of plasma. Equation (5) is the equation of state that indicates adiabatic changes in

$$(\Gamma - 1)(4 - 3b) = T_1 - b \quad (8)$$

with

$$T_1 - b = (b + 12(\gamma - 1)(1 - b)) = (\gamma - 1)(4 - 3b)^2 \quad (9)$$

$$b = \frac{P_g}{P} \quad (10)$$

where γ is the ratio of the specific heats.

In the absence of radiation:

$$P_r = 0 \quad (11)$$

etc.

Formulation of the problem

We consider an unbound plasma cloud under the combined effect of self-gravitating variable inertia, gas pressure gradient and radiation forces. The plasma medium is assumed to be homogenous, inviscid and compressible. We are interested here to identify the inertia and radiation forces effects on the self-gravitational instability of the model.

We shall utilize the Cartesian coordinates (x, y, z) for investigating this problem.

The required equations for the present problem are:

T the temperature at time t and $P (= P_g + P_r)$ the total pressure which is the sum of the gas kinetic pressure P_g and pressure P_r due to radiation:

an enclosure containing matter and radiation. For more details concerning equation (5) we may refer to Chandrasekhar [3], where we find:

therefore,

$$b = 1 \quad (12)$$

$$T = T_1 = \gamma \quad (13)$$

However, if the radiation is taken into account such that its pressure P_r is much greater than gas pressure P_g (i.e. $P_r \gg P_g$), we have:

$$T = T_1 = \frac{4}{3} \quad (14)$$

We assume that the medium: (i) rotates with the general uniform angular velocity:

$$\underline{\Omega} = (\Omega_x, \Omega_y, \Omega_z) \quad (15)$$

and (ii) possesses streams moving in the x -direction with velocity:

$$\underline{u}_o = (U(z), 0, 0) \quad (16)$$

varying along the z -direction of the Cartesian coordinates (x, y, z) .

Perturbation analysis

For small departures from the initial state, every variable quantity Q may be expressed as:

$$Q = Q_o + Q_1, \quad |Q_1| \ll Q_o \quad (17)$$

where Q stands for each ρ, P, \underline{u} and V .

Based on the expansion (17), the perturbation equations could be obtained from (1)-(4) in the form:

$$\rho_o \left(\frac{\partial \underline{u}_1}{\partial t} + (\underline{u}_o \cdot \nabla) \underline{u}_1 + (\underline{u}_1 \cdot \nabla) \underline{u}_o \right) = -\nabla P_1 + \rho \nabla V_1 - 2\rho_o (\underline{u}_1 \wedge \underline{\Omega}) \quad (18)$$

$$\frac{\partial \rho_1}{\partial t} + (\underline{u}_o \cdot \nabla) \rho_1 + (\underline{u}_1 \cdot \nabla) \rho_o + \rho_o (\nabla \cdot \underline{u}_1) + \rho_1 (\nabla \cdot \underline{u}_o) = 0 \quad (19)$$

$$\nabla^2 V_1 = -4\pi G \rho_1 \quad (20)$$

$$\frac{dP_1}{dt} = C_s^2 \frac{d\rho_1}{dt} \quad (21)$$

where $C_s \left(= \sqrt{\frac{\Gamma P_o}{\rho_o}} \right)$ is the sound speed in the fluid.

By the use of the components of \underline{u}_1

$$\underline{u}_1 = (u, v, w) \quad (22)$$

together with the assumptions (15)-(16), the system of equations (18)-(21) may be rewritten as:

$$\rho_o \left[\frac{\partial u}{\partial t} + U_o \frac{\partial u}{\partial x} + w \frac{dU_o}{dz} \right] = -\frac{\partial P_1}{\partial x} + \rho_o \frac{\partial V_1}{\partial x} + 2\rho_o \Omega_y w - 2\rho_o \Omega_z v \quad (23)$$

$$\rho_o \left[\frac{\partial v}{\partial t} + U_o \frac{\partial v}{\partial x} \right] = -\frac{\partial P_1}{\partial y} + \rho_o \frac{\partial V_1}{\partial y} + 2\rho_o \Omega_z u - 2\rho_o \Omega_x w \quad (24)$$

$$\rho_o \left[\frac{\partial w}{\partial t} + U_o \frac{\partial w}{\partial x} \right] = -\frac{\partial P_1}{\partial z} + \rho_o \frac{\partial V_1}{\partial z} + 2\rho_o \Omega_y u - 2\rho_o \Omega_x v \quad (25)$$

$$\frac{\partial \rho_1}{\partial t} + U_o \frac{\partial \rho_1}{\partial x} = -\rho_o \left(\frac{\partial u}{\partial x} + \frac{\partial v}{\partial y} + \frac{\partial w}{\partial z} \right) \quad (26)$$

$$\frac{\partial^2 V_1}{\partial x^2} + \frac{\partial^2 V_1}{\partial y^2} + \frac{\partial^2 V_1}{\partial z^2} = -4\pi G \rho_1 \quad (27)$$

$$\frac{\partial P_1}{\partial t} + U_o \frac{\partial P_1}{\partial x} = C_s^2 \left(\frac{\partial \rho_1}{\partial t} + U_o \frac{\partial \rho_1}{\partial x} \right) \quad (28)$$

$$\rho_0 T_1 - (\Gamma - 1) T_0 \rho_1 = 0 \quad (29)$$

Eigenvalue relation

Apply sinusoidal wave along the fluid interface. Consequently, from the viewpoint of the stability

$$Q_1 \sim \exp \left[i(k_x x + k_y y + k_z z + \sigma t) \right] \quad (30)$$

Here σ is gyration frequency of the assuming wave. k_x , k_y , and k_z are (any real values) the wave

approaches given by Chandrasekhar [3], we assume that the space-time dependence of the wave propagation of the form:

numbers in the (x, y, z) directions. By an appeal to the time-space dependence (30), the relevant perturbation equations (23)-(29) are given by:

$$n\rho_o u + \rho_o w D U_o = -ik_x C_s^2 \rho_1 + ik_x \rho_o V_1 + 2\rho_o \Omega_y w - 2\rho_o \Omega_z v \quad (31)$$

$$n\rho_o v = -ik_y C_s^2 \rho_1 + ik_y \rho_o V_1 - 2\rho_o \Omega_x w + 2\rho_o \Omega_z u \quad (32)$$

$$n\rho_o w = -ik_z C_s^2 \rho_1 + ik_z \rho_o V_1 + 2\rho_o \Omega_y u - 2\rho_o \Omega_x v \quad (33)$$

$$n\rho_1 = -i\rho_o (k_x u + k_y v + k_z w) \quad (34)$$

$$k^2 V_1 = -4\pi G \rho_1 \quad (35)$$

where:

$$k^2 = k_x^2 + k_y^2 + k_z^2, \quad D = \frac{d}{dz} \quad (36)$$

$$n = i(\sigma + k_x U_o) \quad (37)$$

The foregoing system equations (31)-(35) could be rewritten in the matrix form:

$$\left[a_{ij} \right] \left[b_j \right] = 0 \quad (38)$$

where the elements $[a_y]$ of the matrix are given in the Appendix while the elements of the column matrix $[b_j]$ are u, v, w, ρ_1 and V_1 . For non-trivial solution

$$A_5 n^5 + A_4 n^4 + A_3 n^3 + A_2 n^2 + A_1 n + A_0 = 0 \quad (39)$$

where the compound coefficients $A_i (i = 0, 1, 2, 3, 4, 5)$ are calculated.

RESULTS AND DISCUSSION

Equation (39) is a general eigenvalue relation of a rotating self-gravitating streaming plasma cloud. Some previously published results may be obtained

$$k^2 n^3 + k^2 (k^2 C_s^2 - 4\pi G \rho_o) n - k_x k_z (k^2 C_s^2 - 4\pi G \rho_o) D U_o = 0 \quad (40)$$

This relation coincides with the dispersion relation of a pure self-gravitating fluid medium streaming with variable streams $(U_o(z), 0, 0)$ derived by Sengar [4]. For more details concerning

$$n^2 = k^2 C_s^2 - 4\pi G \rho_o \quad (41)$$

This gives the same results given by Jeans [5]. For more details concerning the instability of this case we may refer to the discussions of Jeans [5].

The purpose of the present part is to determine the influence of rotation on Jeans' criterion (41) of a

$$n^4 + (4\pi G \rho_o - C_s^2 k_z^2 - 4\Omega^2) n^2 + 4\Omega_z^2 (C_s^2 k_z^2 - 4\pi G \rho_o) = 0 \quad (42)$$

with

$$\Omega^2 = \Omega_y^2 + \Omega_z^2 \quad (43)$$

Equation (40) indicates that there must be two modes in which a wave can be propagated in the

$$n_1^2 + n_2^2 = C_s^2 k_z^2 + 4\Omega^2 - 4\pi G \rho_o \quad (44)$$

$$n_1^2 n_2^2 = 4\Omega_z^2 (C_s^2 k_z^2 - 4\pi G \rho_o) \quad (45)$$

and so we see that both the roots n_1^2 and n_2^2 are real. The discussions of (40) indicate that if the

$$C_s^2 k_z^2 - 4\pi G \rho_o < 0 \quad (46)$$

is valid, then one of the two roots n_1^2 or n_2^2 must be negative and consequently the model will be unstable. This means that under the Jeans' restriction (46), the self-gravitating rotating fluid medium is unstable. This shows that the Jeans' criterion for a

of the equations (38), setting the determinant of the matrix $[a_y]$ equal to zero (see Appendix), we get the general eigenvalue relation of seven order in n in the form:

as limiting cases here. That confirms the present analysis.

In absence of rotation, radiation forces and for inviscid fluid, i.e. $\underline{\Omega} = 0$, equation (39) yields:

the stability of this case we may refer to Sengar [4].

If $\underline{\Omega} = 0$ and $U_o = 0$, equation (39) reduces to:

uniform streaming fluid. So in order to carry out and to facilitate the present situation we may choose $\Omega_x = 0, k_x = 0$ and $k_y = 0$, then equation (39) gives:

medium. If the roots of (40) are n_1^2 and n_2^2 , then we have:

Jeans' restriction:

self-gravitating medium is unaffected by the influence of the uniform rotation.

If the non-streaming plasma cloud medium is acted upon by the combined effect of self-gravitation, gas pressure gradient and radiating pressure gradient forces, relation (39) reduces to:

$$\sigma^2 + \rho_0 A k^2 - 4\pi G \rho_0 = 0 \quad (47)$$

As the radiating self-gravitating plasma cloud streams uniformly with velocity $\underline{u}_0 = (U, 0, 0)$ the general eigenvalue relation (39) becomes:

$$\sigma^2 + 2iUk\sigma - (U^2 k_x^2 + 4\pi G \rho_0 - \rho_0 A k^2) = 0 \quad (48)$$

The quadratic equation (48) has imaginary roots if

$$4\pi G \rho_0 > A \rho_0 k^2 \quad (49)$$

This restriction (49) for a streaming plasma cloud is exactly the same as that given by Jeans' criterion [1] Therefore, we conclude that the inertia force due to uniformly streaming plasma cloud has no influence at all on the instability of a self-gravitating plasma cloud in the presence of radiation.

CONCLUSION

The effect of radiation on the self-gravitating instability of a rotating plasma cloud with streams of variable velocity distribution function of coordinate is discussed. The self-gravitating force is destabilizing according to restrictions. The rotating force has a stabilizing influence under certain restrictions. The radiation has a strong stabilizing influence for all short and long perturbation wave lengths. In the presence of radiation, the uniform streaming has no influence at all on the instability of the model and the radiation overcomes the self-gravitating instability of a plasma cloud. The inertia force due to uniformly streaming plasma cloud has no influence at all on the instability of a self-gravitating plasma cloud in the presence of radiation.

REFERENCES

1. J. Jeans, H. Philos, *Trans. R. Soc. London*, **199**, 1 (1902).
2. S. Chandrasekhar, E Fermi, *Astrophys. J.*, **118**, 116 (1953).
3. S. Chandrasekhar, *Hydrodynamic and Hydromagnetic Stability*, Dover, New York, 1981.

4. R. S. Sengar, *Proc. Acta Sci. India*, **51(A)**, 39 (1981).
5. A. Hasan, *Mathematical Problems in Engineering*, **1**, 1 (2012).
6. J. Kormendy, L. Ho, *Annual Review of Astronomy and Astrophysics*, **51**, 511 (2013).
7. X. Chen, P. Amaro-Seoane, J. Cuadra, *The Astrophysical Journal*, **819** (138), 1 (2016).
8. A. Hasan, *International Journal of Biomathematics*, **9(3)**, 1 (2016).
9. A. Hasan, *Bulg. Chem. Commun.*, **49(2)**, 487 (2017).
10. A. Hasan, *Research Journal of Applied Sciences, Engineering and Technology*, **14(10)**, 399 (2017).
11. G. Hoshoudy, A. Hasan, P. Kumar, *Journal of Scientific and Engineering Research*, **5(3)**, 245 (2018).
12. R. Morimoto, M. Miura, A. Sugiyama, M. Miura, Y. Oshikiri, I. Mogi, S. Takagi, Y. Yamauchi, R. Aogaki, *Journal of Electroanalytical Chemistry*, **847**(113255), 1 (2019).
13. R. Morimoto, M. Miura, A. Sugiyama, M. Miura, Y. Oshikiri, I. Mogi, S. Takagi, Y. Yamauchi, R. Aogaki, *Journal of Electroanalytical Chemistry*, **848**(113254), 1 (2019).
14. T. Weyens, J. Reynolds-Barredo, A. Loarte, *Computer Physics Communications*, **242**, 60 (2019).

APPENDIX

The elements a_{ij} ($i=1,2,\dots,5$ and $j=1,2,\dots,5$) of the matrix $[a_{ij}]$ in equation (40) of the linear algebraic equations (32)-(36) are:

$$\begin{aligned}
 a_{11} &= (n\rho_o), & a_{12} &= (2\rho_o\Omega_z), & a_{13} &= (\rho_o DU_o - 2\rho_o\Omega_y) \\
 a_{14} &= ik_x C_s^2, & a_{15} &= -i\rho_o k_x \\
 a_{21} &= (-2\rho_o\Omega_z), & a_{22} &= (n\rho_o), & a_{23} &= (2\rho_o\Omega_x) \\
 a_{24} &= ik_y C_s^2, & a_{25} &= -i\rho_o k_y \\
 a_{31} &= (-2\rho_o\Omega_y), & a_{32} &= (2\rho_o\Omega_x), & a_{33} &= (n\rho_o) \\
 a_{34} &= ik_z C_s^2, & a_{35} &= -i\rho_o k_z \\
 a_{41} &= i\rho_o k_x, & a_{42} &= i\rho_o k_y, & a_{43} &= i\rho_o k_z \\
 a_{44} &= n, & a_{45} &= 0 \\
 a_{51} &= 0, & a_{52} &= 0, & a_{53} &= 0 \\
 a_{54} &= 4\pi G, & a_{55} &= k^2
 \end{aligned}$$

NiO-ZrO₂ heterogeneously catalysed efficient multicomponent synthesis of polyhydroquinoline derivatives

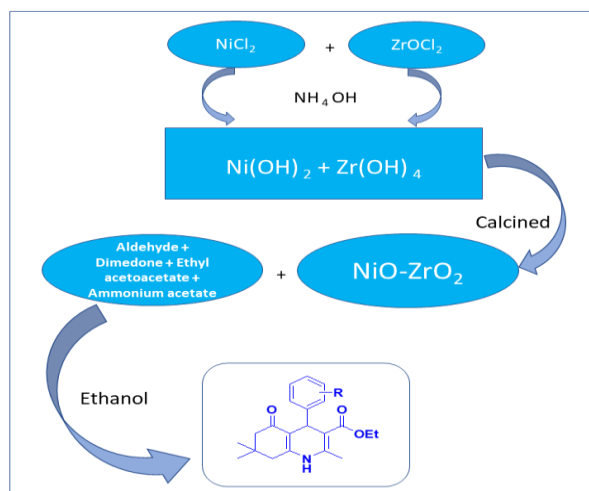
P. A. Mule¹, M. K. Patil², M. E. Navgire³, A. A. Yelwande^{1*}

¹Indraraj Arts, Commerce and Science College, Sillod, Aurangabad, Maharashtra, India

²Dr. Babasaheb Ambedkar Marathwada University, Sub-Centre, Osmanabad, India

³Jijamata College of Science & Arts, Bhende, Ahmednagar, India

Received: January 18, 2020; Revised: May 11, 2020



NiO-ZrO₂ composite material was synthesized by using a sol-gel method and was characterized by using X-ray diffraction (XRD), transmission electron microscopy (TEM), scanning electron microscopy (SEM), energy-dispersive X-ray spectroscopy (EDS) and Fourier transform infrared spectroscopy (FT-IR). The synthesized NiO-ZrO₂ composite material was successfully used as a heterogeneous catalyst for five-component one-pot synthesis of polyhydroquinolines by the cyclo-condensation reaction of aromatic aldehydes, dimedone, ethyl acetoacetate, ammonium acetate and ethanol at room temperature. NiO-ZrO₂ catalytic composite material was found to give higher yield when compared to NiO and ZrO₂ separately.

Keywords: Polyhydroquinoline, NiO-ZrO₂, sol-gel.

INTRODUCTION

Nickel oxide (NiO) is an important inorganic material having applications in solar cells, capacitors and rechargeable lithium ion batteries [1-4]. Nickel nanoparticles are important for catalysis [5]. Zirconium oxide (ZrO₂) is an important transition metal oxide which shows promising optical and electrical properties [6] and has various applications in catalysts, coatings, fuel cells and sensors [7-10]. Several methods are used for the preparation of ZrO₂ materials like hydrothermal, sol-gel, chemical vapour deposition (CVD) and sputtering [11-14]. The acid-base and redox properties of metal oxides and mixed metal oxides are important in heterogeneous catalysis [15-18]. These oxides can be used in various organic transformations such as oxidation [19-21], dehydration [22], condensation

[23], epoxidation [24] and photocatalytic reaction [25, 26].

1,4-Dihydropyridines (1,4-DHPs) and polyhydroquinoline (PHQ) derivatives are important nitrogen-containing heterocycles due to their pharmacological and biological activity [27]. Some of them have antitubercular, anticancer, neurotropic, neuropeptide, YY receptor antagonist, neuroprotective, platelet anti-aggregation, bronchodilating and antidiabetic activity [28-35]. Multicomponent synthesis of polyhydroquinoline derivatives has been carried out using various catalysts such as TMSCl, ionic liquid, polymer, molecular I₂, CAN, Yb(OTf)₃, HClO₄-SiO₂, heteropolyacid, and MCM-41 [36-46]. However, these show several disadvantages such as long reaction time, low yield, use of high-volatile organic solvents and harsh reaction conditions.

* To whom all correspondence should be sent:
E-mail: ajeetye@gmail.com

Recent work has been reported on a similar topic, using Four-Component Fusion Protocol with NiO/ZrO₂ for 1,4-dihydropyridines [47], where catalytic material was prepared by the wet impregnation method. Hence, a simple and efficient catalyst can be developed for the synthesis of polyhydroquinoline derivatives.

Considering the advantages of metal oxides it was intended to synthesize a NiO-ZrO₂ composite, characterize it with various sophisticated analytical techniques such as XRD, TEM, SEM-EDS and FT-IR and use it as an efficient catalyst for the synthesis of polyhydroquinoline derivatives.

EXPERIMENTAL

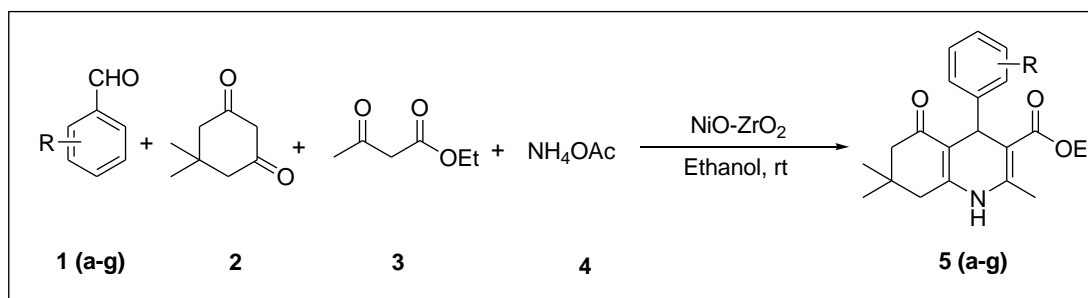
All chemicals were purchased from Merck and used without further purification. The melting points of all derivatives were taken in an open capillary and are uncorrected. ¹H NMR spectra were recorded on a 300 MHz FT-NMR spectrometer in CDCl₃ as a solvent and chemical shift values were recorded as δ (ppm) relative to tetramethylsilane (Me₄Si) as an internal standard. FT-IR spectra were recorded on a JASCO-FT-IR/4100 instrument, Japan, in KBr. The X-ray diffraction (XRD) patterns were recorded on a Bruker 8D advance X-ray diffractometer using monochromator Cu-Kα radiation of wavelength = 1.5405 Å. Transmission electron microscopy (TEM) was recorded on a CM-200 PHILIPS instrument operated at 200 kV, resolution at 0.23 nm. Scanning electron microscopy image with energy dispersive X-ray spectroscopy (SEM-EDS) was obtained on JEOL JSM-6330 LA operated at 20.0 KV, 1.000 nA.

Synthesis of NiO-ZrO₂ heterogeneous catalyst

NiO-ZrO₂ composite material was synthesized by the sol-gel method. Nickel (II) chloride hexahydrate (0.31 g) and zirconium (IV) oxychloride octahydrate (2.7 g) were dissolved in double distilled water (DDW), then ammonium hydroxide (NH₄OH) was added to obtain a white precipitate. The resulting reaction mixture was stirred continuously at room temperature for 5 hours. The mixture was then filtered and dried at 110°C in an oven for 10 hours so as to form powder material. Finally, the powder material was calcined at 500°C for 2 hours to obtain NiO-ZrO₂ composite material.

General procedure for the synthesis of polyhydroquinoline derivatives

A solution of aldehydes (1 mmol), dimedone (1 mmol), ethyl acetoacetate (1 mmol) and ammonium acetate (3 mmol) was prepared at room temperature in ethanol (15 ml) as solvent and NiO-ZrO₂ (0.05 g) was added as catalyst with continuous stirring for specific time as shown in Scheme 1 and Table 5. The progress of reaction was monitored by TLC using petroleum ether: ethyl acetate (7:3). After completion of reaction, the reaction mixture was filtered. The catalyst was easily separated from the reaction mixture. Filtrate was poured on crashed ice to crystallize the crude product. Crude product was recrystallized from ethanol to obtain the pure product.



Scheme 1. Synthesis of polyhydroquinoline derivatives

Spectroscopic data of compounds

5a. Ethyl 1,4,5,6,7,8-hexahydro-2,7-dimethyl-5-oxo-4-phenylquinoline-3-carboxylate: ¹H NMR data in (CDCl₃, 300 MHz): δ 1.07 (s, 6H), 1.11 (t, 3H), 2.12-2.23 (m, 4H), 2.32 (s, 3H), (4.07 (q, 2H), 5.04 (s, 1H), 6.64 (s, 1H, NH), 7.10 (d, 2H), 7.18 (q, 1H), 7.30 (d, 2H). ¹³C NMR (100 MHz, CDCl₃): 14.22, 19.24, 28.05, 31.54, 36.60, 40.92, 50.76, 59.82, 106.93, 111.98, 126.03, 128.02, 143.75, 147.12, 148.79, 167.55, 196.11. FT-IR (KBr, cm⁻¹): 3284,

3078, 2928, 1885, 1603, 1484, 1379, 1278, 1212, 1043 cm⁻¹.

5b. Ethyl 4-(4-chlorophenyl)-1,4,5,6,7,8-hexahydro-2,7-dimethyl-5-oxoquinoline-3-carboxylate: ¹H NMR data in (CDCl₃, 300 MHz): δ 1.07 (s, 6H), 1.12 (t, 3H), 2.12-2.30 (m, 4H), 2.36 (s, 3H), 4.06 (q, 2H), 5.01 (s, 1H), 6.47 (s, 1H, NH), 7.16 (d, 2H), 7.24 (d, 2H). ¹³C NMR (100 MHz, CDCl₃): 14.22, 19.32, 28.05, 31.93, 36.24, 41.38, 50.85, 59.92, 105.67, 111.75, 128.20, 130.95,

131.59, 143.71, 148.56, 149.26, 167.29, 196.12. FT-IR (KBr, cm⁻¹): 3200, 3074, 2925, 1983, 1740, 1600, 1487, 1376, 1276, 1213, 1069 cm⁻¹.

5c. Ethyl 4-(4-fluorophenyl)-1,4,5,6,7,8-hexahydro-2,7-dimethyl-5-oxoquinoline-3-carboxylate: ¹H NMR data in (CDCl₃, 300 MHz): δ 1.07 (s, 6H), 1.12 (t, 3H), 2.24-2.37 (m, 4H), 2.63 (s, 3H), 4.07 (q, 2H), 5.04 (s, 1H), 7.10 (s, 1H), 7.30-7.46 (m, 4H), 10.03 (s, 1H, NH). ¹³C NMR (100 MHz, CDCl₃): 14.23, 19.20, 27.44, 31.54, 32.68, 41.40, 52.30, 53.93, 111.20, 112.24, 118.76, 121.21, 122.84, 129.93, 136.25, 142.43, 167.55, 198.62. FT-IR (KBr, cm⁻¹): 3171, 3045, 2931, 1833, 1616, 1502, 1456, 1353, 1204, 1113, 736 cm⁻¹.

5d. Ethyl 1,4,5,6,7,8-hexahydro-2,7,7-trimethyl-4-(3-nitrophenyl)-5-oxoquinoline-3-carboxylate ¹H NMR data in (CDCl₃, 300 MHz): δ 1.07 (s, 6H), 1.12 (t, 3H), 2.12-2.30 (m, 4H), 2.63 (s, 3H), 4.07 (q, 2H), 5.04 (s, 1H), 6.65 (s, 1H, NH), 7.37 (t, 1H), 7.71 (d, 1H), 7.99 (t, 1H), 8.11 (d, 1H).

5e. Ethyl 1,4,5,6,7,8-hexahydro-2,7,7-trimethyl-5-oxo-4-p-tolylquinoline-3-carboxylate ¹H NMR data in (CDCl₃, 300 MHz): δ 1.07 (s, 6H), 1.12 (t, 3H), 2.12-2.30 (m, 4H), 2.34 (s, 3H), 2.63 (s, 3H), 4.07 (q, 2H), 5.04 (s, 1H), 6.64 (s, 1H, NH), 7.01 (d, 2H), 7.17 (d, 2H).

5f. Ethyl 4-(furan-2-yl)-1,4,5,6,7,8-hexahydro-2,7,7-trimethyl-5-oxoquinoline-3-carboxylate ¹H NMR data in (CDCl₃, 300 MHz): δ 1.07 (s, 6H), 1.12 (t, 3H), 2.12-2.30 (m, 4H), 2.63 (s, 3H), 4.07 (q, 2H), 5.04 (s, 1H), 6.64 (s, 1H, NH), 6.01 (s, 1H), 6.20 (s, 1H), 7.16 (s, 1H).

5g. Ethyl 1,4,5,6,7,8-hexahydro-4-(4-hydroxyphenyl)-2,7,7-trimethyl-5-oxoquinoline-3-carboxylate: ¹H NMR data in (CDCl₃, 300 MHz): δ 1.07 (s, 6H), 1.12 (t, 3H), 2.12-2.30 (m, 4H), 2.63 (s, 3H), 4.07 (q, 2H), 5.04 (s, 1H), 5.60 (s, 1H), 6.64 (s, 1H, NH), 6.64 (d, 2H), 7.16 (d, 2H).

Catalyst characterization

XRD analysis: Figure 1 shows the XRD pattern of NiO-ZrO₂. Catalytic material NiO shows the peaks obtained at 2θ° 25.47, 35.80, 51.88, 64.34, 78.87 corresponding to planes (110), (200), (220), (222) and (332) predicting a cubic structure with a = b = c = 5.341 of NiO and matching with JCPDS card no 780643.

Similarly, ZrO₂ shows a highly crystalline monoclinic phase having a = 5.169, b = 5.232, c = 5.341 showing peaks at 2θ° 29.74, 33.79, 38.12, 49.02, corresponding to the planes (-111), (002), (012), (022) and matching with JCPDS card no 371484. Similarly, some peaks were also observed for a tetragonal phase with a = 3.605, b = 3.606, c = 5.18 showing peaks at 2θ° 24.71, 30.50, 39.53,

57.16, 60.14, 66.03 and 74.48 corresponding to the planes (100), (101), (111), (210), (103), (113), (220) matching for ZrO₂.

Crystallite size of all samples was calculated by using Debye-Scherrer equation. The crystallite size mentioned is the average of crystallite size calculated using FWHM of the three highest intensity peaks. The XRD peaks are very broad; indicating that the NiO nanocrystallites are observed at crystallite size 35.85 nm and for ZrO₂ is 39.01 nm. The rod-like morphology is maintained on a large scale, as evidenced by the TEM image in Figure 2. It clearly indicated that NiO was completely deposited on the surface of ZrO₂.

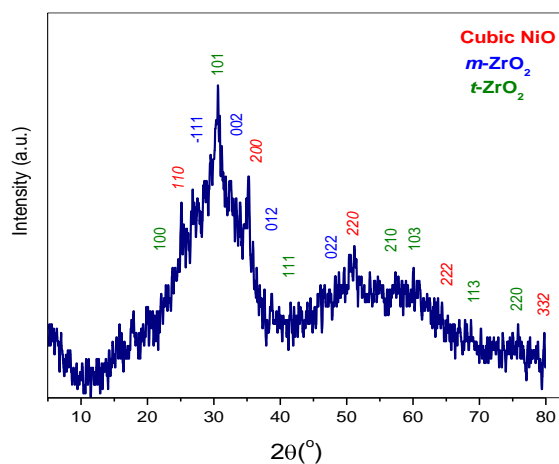


Figure 1. XRD pattern of NiO-ZrO₂

TEM analysis: The TEM images obtained for NiO-ZrO₂ are shown in Figure 2 (a-e). It exhibits uniform size distribution and high crystalline nature with size range of 35 ± 5 nm, matching with the XRD data (35.81 and 39.01 nm for NiO and ZrO₂ respectively). The diffraction spots and rings in the SEAD pattern, shown in figure 2 (f), indicate that the distance from the center of the rings to the diffraction spots is 0.29 nm for the (110) planes of NiO and 0.25 nm for the (101) planes of ZrO₂.

SEM-EDS analysis: The morphology of the catalyst was studied with scanning electron microscopy (SEM). Figure 3 indicates that nickel oxide (NiO) is uniformly deposited on the surface of zirconium oxide (ZrO₂). An increase in the crystalline state with the decrease in grain size was also observed, which results in enhancing the catalytic activity of the prepared material.

Energy-dispersive X-ray spectroscopy (EDS) image of the NiO-ZrO₂ composite material is shown in Figure 4. It reveals that constituent's elements O, Ni and Zr are present as their atomic weights (%) are 41.41, 18.18 and 40.41, respectively. The elemental analysis proved that the minimum required stoichiometric ratio is maintained (Table 1).

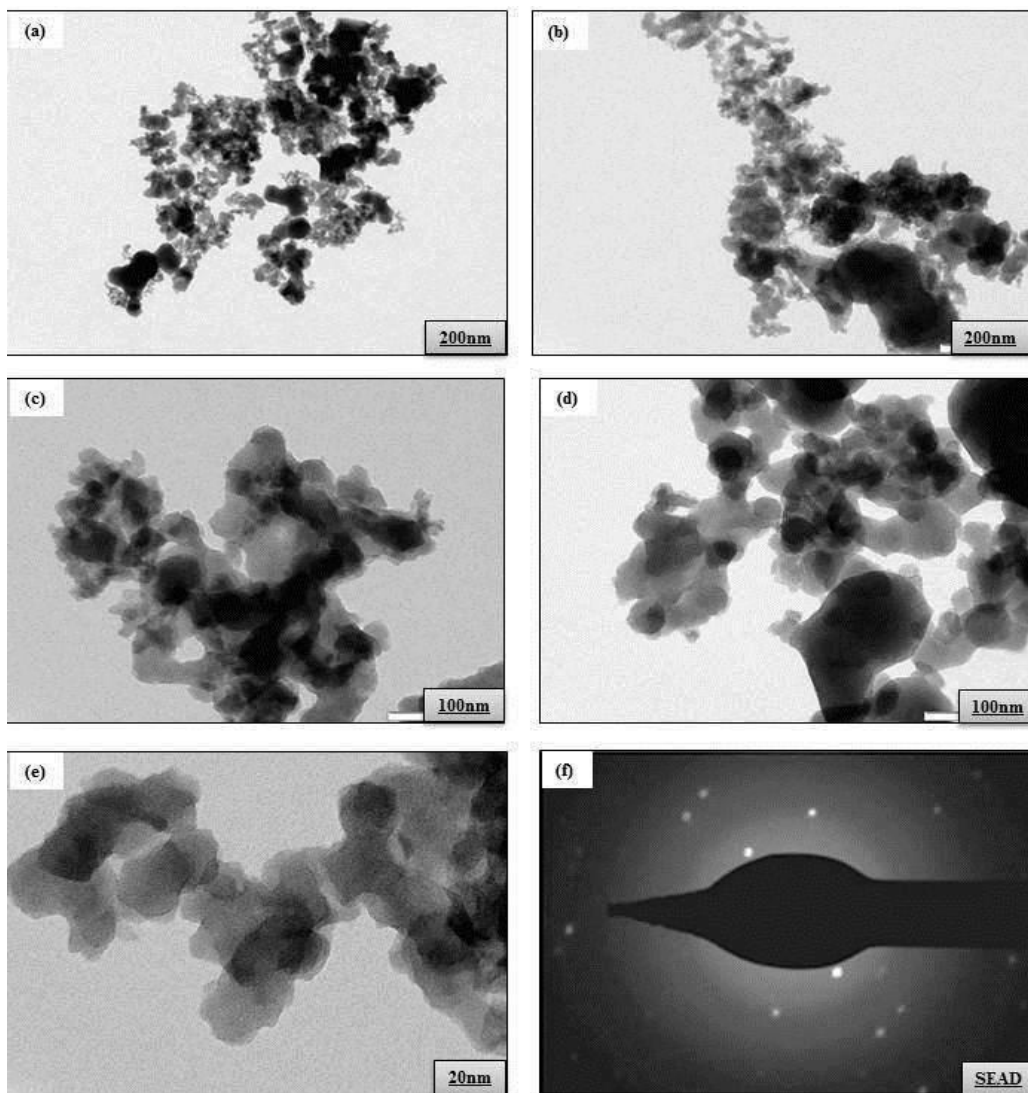


Figure 2. TEM images with different magnifications at (a, b) 200 nm, (c, d) 100 nm, (e) 20 nm and (f) SEAD pattern of NiO-ZrO₂

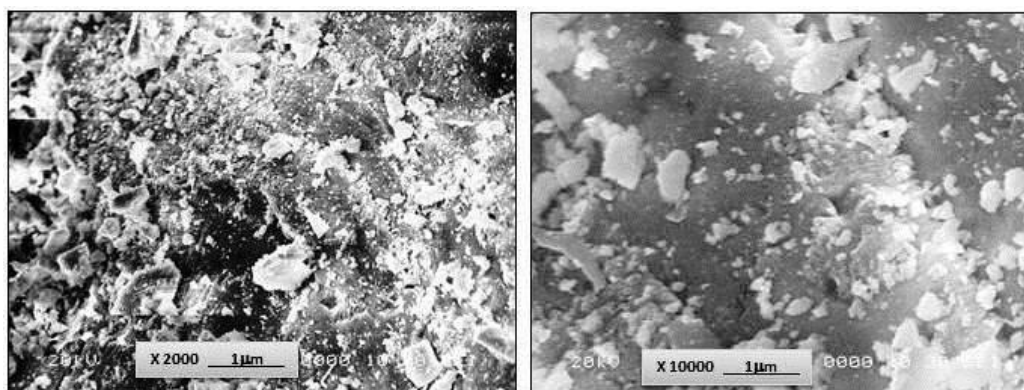


Figure 3. SEM images of NiO-ZrO₂ with different magnifications

Table 1. EDS pattern of NiO-ZrO₂

Element	Weight %	Atomic %
O	41.41	68.12
Ni	18.18	20.22
Zr	40.41	11.66
Total	100.00	100.0

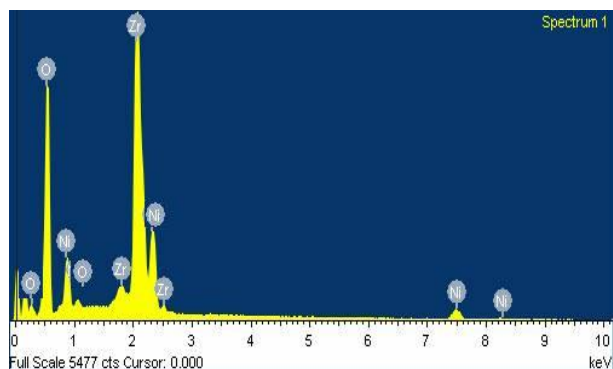


Figure 4. EDS image of NiO-ZrO₂.

FTIR analysis: Figure 5 shows the FTIR spectrum of the NiO-ZrO₂ catalytic material. The broad absorption band at 3106 cm⁻¹ can be assigned mainly to Ni-OH and Zr-OH stretching modes and that at 1641 cm⁻¹ - to the bending mode of water. The strong and intense band observed at 1090 cm⁻¹ is due to Ni-O and Zr-O stretching. The band observed at 740 cm⁻¹ is assigned to Ni-O-Ni, Zr-O-Zr bending vibrations. Similarly, sharp bands are seen at 603 cm⁻¹, which corresponds to the formation of bonds between NiO-ZrO₂ materials.

RESULTS AND DISCUSSION

After characterization and confirmation of the NiO-ZrO₂ nanocomposite material, it was tested as a heterogeneous catalyst for the synthesis by organic transformation of polyhydroquinoline derivatives. Good to excellent yield of all derivatives was established.

We performed a schematic study of the same reaction by varying the solvent, catalyst type and amount. The syntheses of polyhydroquinoline were done using benzaldehyde, dimedone, ethyl acetoacetate, ammonium acetate and ethanol as a model reaction. The results obtained using various catalysts are summarised in Table 2. NiO and ZrO₂ show better yields but time span also increases (entries 1 and 2).

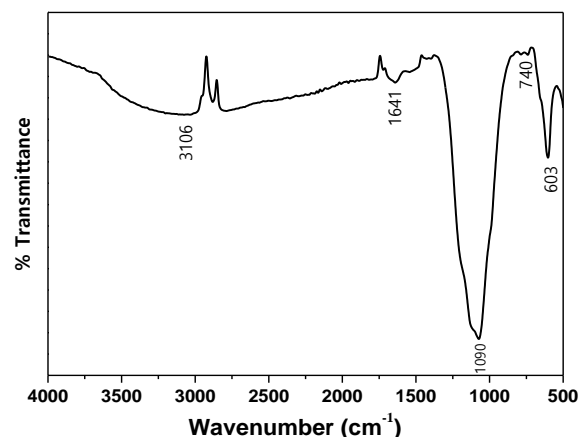


Figure 5. FTIR spectrum of NiO-ZrO₂

NiO-ZrO₂ mixed metal oxides show good to excellent yields of the desired product, shorter reaction times and improved catalytic stability for the reaction (entry 3). Hence, we have selected the NiO-ZrO₂ catalyst for the synthesis of various derivatives.

The effect of different solvents such as water, ethanol: water (1:1), acetonitrile and ethanol is shown in Table 3. The use for water gives poor yields of the product (entry 1); ethanol: water (1:1) and acetonitrile gave moderate yields (entries 2 and 4) while ethanol as a solvent gave good to excellent yields of the product and also reduced the reaction rate (entry 3). Ethanol solvent shows better activity; therefore, ethanol was selected as a solvent for the synthesis of polyhydroquinoline derivatives.

Table 2. Study of various catalysts for the synthesis of polyhydroquinoline

Entry	Catalyst	Time (min) ^a	Yield (%) ^b
1	NiO	200	85
2	ZrO ₂	190	88
3	NiO-ZrO ₂	60	93

^aReaction conditions: benzaldehyde (1 mmol), dimedone (1 mmol), ethyl acetoacetate (1 mmol), ammonium acetate (3 mmol), ethanol (15 ml) and catalyst (0.05g). ^bIsolated yields.

After studying the effect of solvent we examined how much amount of catalyst is needed for the reaction. In the absence of catalyst, no product was obtained in 250 min. We have studied different weights of catalyst such as 0.03, 0.04, 0.05, 0.06, 0.1, and 0.15 g (see Table 4). The amounts 0.03 and 0.04 g of catalyst showed poor catalytic activity for the present reaction (entries 2 and 3).

Table 3. Study of various solvents for the synthesis of polyhydroquinoline

Entry	Solvent	Time (min) ^a	Yield (%) ^b
1	Water	250	55
2	Ehanol:Water	150	80
3	Ethanol	60	93
4	Acetonitrile	160	75

^aReaction conditions: benzaldehyde (1 mmol), dimedone (1 mmol), ethyl acetoacetate (1 mmol), ammonium acetate (3 mmol), ethanol (15 ml) and catalyst (0.05g). ^bIsolated yields.

Catalyst amounts of 0.05, 0.06, 0.1 and 0.15 g showed good to excellent yields of the product (entries 4, 5, 6 and 7). Catalyst amount of 0.05 g was considered sufficient for the reaction.

After optimizing the solvent, catalyst type and amount, we studied the synthesis of polyhydroquinolines. The results are shown in Table 5.

Table 4. Amount of catalyst for the synthesis of polyhydroquinoline

Entry	Catalyst amount (g)	Time (min) ^a	Yield (%) ^b
1	-	250	-
2	0.03	80	78
3	0.04	75	83
4	0.05	60	93
5	0.06	60	93
6	0.1	60	93
7	0.15	60	93

^aReaction conditions: benzaldehyde (1 mmol), dimedone (1 mmol), ethyl acetoacetate (1 mmol), ammonium acetate (3 mmol) and ethanol (15 ml). ^bIsolated yields.

The main advantage in this reaction is the recycling and reusability of the catalytic material. The catalyst was separated, washed and dried before next catalytic activity for the reaction. The catalyst reused five times does not decrease its catalytic activity for the reaction (Table 5, entry 5a).

Table 5. Synthesis of polyhydroquinoline using NiO-ZrO₂ catalyst^a

Entry	R	Time (min)	Yield (%) ^b	M.P. (°C)
5a	Ph	60	93(92,91,91,90,90 °)	202-204
5b	<i>p</i> -Cl-C ₆ H ₄	60	92	240-242
5c	<i>p</i> -F-C ₆ H ₄	75	88	180-184
5d	<i>m</i> -NO ₂ -C ₆ H ₄	80	85	175-177
5e	<i>p</i> -Me-C ₆ H ₄	85	88	260-262
5f	2-Furyl	70	85	245-247
5g	<i>p</i> -OH-C ₆ H ₄	70	86	234-236
5h	Indol-3-carboxyl	180	No reaction	

^aReaction conditions: benzaldehyde (1 mmol), dimedone (1 mmol), ethyl acetoacetate (1 mmol), ammonium acetate (3 mmol), ethanol (15 ml) and catalyst (0.05 g). ^bIsolated yields. ^cYield after consecutive cycles.

CONCLUSION

We developed an efficient method for synthesis of polyhydroquinolines by the cyclo-condensation reaction of aromatic aldehydes, dimedone, ethyl acetoacetate, ammonium acetate and ethanol at room temperature. NiO-ZrO₂ catalytic material was synthesized by the sol-gel method. Prepared material was characterized by XRD, TEM, SEM-EDS and FT-IR. Present method shows several advantages such as high yields, non-toxicity, easy recovery and reuse of the catalyst.

Acknowledgements: Authors are thankful to the Principal Indraraj Arts, Commerce and Science College, Sillod, Aurangabad, Maharashtra, India for providing instrumental support.

REFERENCES

1. Y. Wu, Y. He, T. Wu, T. Chen, W. Weng, H. Wan, *Mater. Lett.*, **61**, 3174 (2007).
2. J. Bandara, H. Weerasinghe, *Sol. Energy Mater. Sol. Cells*, **85**, 385 (2005).
3. F-b. Zhang, Y-k. Li, H. Zhou, *Mater. Chem. Phys.*, **83**, 260 (2004).

4. R. A. Kumar, A. L. C-J. Tuan Park, J. Kim, *Ceram. Int.*, **39**, 6611 (2013).
5. S. B. Sapkal, K. F. Shelke, B. B. Shingate, M. S. Shingare, *Tetrahedron Letters*, **50**, 1754 (2009).
6. M. Jafarpour, E. Rezapour, M. Ghahramaninezhad, A. Rezaeifard, *New J. Chem.*, **38** (2), 676 (2014).
7. X. Li, Ch. Ni, Ch. Yao, Zh. Chen, *Appl. Catal. B: Environ.*, **462**, 112 (2012).
8. R. Vassen, X. Cao, F. Tietz, D. Basu, D. Stover, *J. Am. Cer. Soc.*, **83**, 2023 (2000).
9. B. C. H. Steele, A. Heinzl, *Nature*, **414**, 345 (2001).
10. B. G. Mohammad, M.-B. Leila, *J. Electroanal. Chem.*, **33**, 712 (2014).
11. M. N. Tahir, L. Gorgishvili, J. Li, T. Gorelik, U. Kolb, L. Nasdala, W. Tremel, *Solid State Sci.*, **9**, 1105 (2007).
12. G. Ehrhart, B. Capoen, O. Robbe, P. Boy, S. Turrell, M. Bouazaoui, *Thin Solid Films*, **227**, 496 (2006).
13. A. M. Torres-Huerta, M. A. Dominguez-Crespo, E. Ramirez-Meneses, J. R. Vargas-Garcia, *Appl. Surf. Sci.*, **255**, 4792 (2009).
14. C. Rozo, D. Jaque, L. F. Fonseca, J. G. Sole, *J. Lumin.*, **128**, 1197 (2008).
15. H. H. Kung, *Transition Metal Oxides: Surface Chemistry and Catalysis*, **45**, 1 (1989).
16. V. E. Henrich, P. A. Cox, *The surface science of metal oxides*; Cambridge University Press, Cambridge, UK, 1994.
17. C. Noguera, *Physics and chemistry at oxide surface*; Cambridge University Press, Cambridge, UK, 1996.
18. B. M. Reddy, Redox properties of metal oxides, in: *Metal oxides chemistry and application*, J. L. G. Fierro (ed.), Marcel Dekker Inc., 1990.
19. I. Spasova, G. Ivanov, V. Georgescu, D. J. Mehandjiev, *J. University of Chemical Technology and Metallurgy*, **41**, 225 (2006).
20. W. Feng, X. Jie, X. Li, L. Zhou, *Adv. Synth. Catal.* **347**, 1987 (2005).
21. R. Lagnathan, R. Mahalakshmy, B. Viswanathan, *Bull. Catal. Soc. India*, **7**, 50 (2008).
22. M. B. Gawande, R. V. Jayaram, *Catal. Commun.*, **7**, 933 (2006).
23. T.-F. Susana, P. Roberto, D. A. Gloriya, *Reaction Kinetics and Catalysis Letters*, **92**, 361 (2007).
24. Z. Fakhroueian, F. Farzaneh, M. Ghandi, *J. Sci. Islamic Republic of Iran*, **18**, 303 (2007).
25. J. Jose, J. Ameta, P. B. Punjabi, *Bull. Catal. Soc. India*, **6**, 110 (2007).
26. A. B. Gambhire, M. K. Lande, B. R. Arbad, *Bull. Catal. Soc. India*, **7**, 28 (2008).
27. R. Shan, C. Velazquez, E. E. Knaus, *J. Med. Chem.*, **47**, 254 (2004).
28. P. S. Eharkar, B. Desai, H. Gaveria, B. Varu, R. Loriya, Y. Naliapara, A. Shah, V. M. Kulkarni, *J. Med. Chem.*, **45**, 4858 (2002).
29. T. Tsuruo, H. Iida, M. Nojiri, S. Tsukagoshi, Y. Sakurai, *Cancer Res.*, **43**, 2905 (1983).
30. A. Krauze, S. Germane, O. Eberlins, I. Sturms, V. Klusa, G. Duburs, *Eur. J. Med. Chem.*, **34**, 301 (1999).
31. G. S. Poindexter, M. A. Bruce, J. G. Breitenbucher, M. A. Higgins, S. Y. Sit, J. L. Romine, S. W. Martin, S. A. Ward, R. T. McGovern, W. Clarke, J. Russell, I. Antal-Zimanyi, *Bioorg. Med. Chem.*, **12**, 507 (2004).
32. V. Klusa, *Drugs Future*, **20**, 135 (1995).
33. R. G. Bretzel, C. C. Bollen, E. Maeser, K. F. Federlin, *Am. J. Kidney Dis.*, **21**, 53 (1993).
34. R. W. Chapman, G. Danko, M. I. Siegels, *Pharmacology*, **29**, 282 (1984).
35. A. K. Ogawa, C. A. Willoughby, R. Bergeron, K. P. Ellsworth, W. M. Geissler, R. W. Myer, J. Yao, G. Harris, K. T. Chapman, *Bioorg. Med. Chem. Lett.*, **13**, 3405 (2003).
36. S.-J. Tu, J.-F. Zhou, X. Deng, P.-J. Cai, H. Wan, J.-C. Feng, *Chin. J. Org. Chem.*, **21**, 313 (2001).
37. G. Sabitha, G. S. K. K. Reddy, C. S. Reddy, J. S. Yadav, *Tetrahedron Lett.*, **44**, 4129 (2003).
38. S.-J. Ji, Z.-Q. Jiang, J. Lu, T.-P. Loh, *Synlett.*, **5**, 831 (2004).
39. J. G. Breitenbucher, G. Figliozzi, *Tetrahedron Lett.*, **41**, 4311 (2000).
40. A. Dondoni, A. Massi, E. Minghini, V. Bertolasi, *Tetrahedron*, **60**, 2311 (2004).
41. S. Ko, M. N. V. Sastry, C. Lin, C.-F. Yao, *Tetrahedron Lett.*, **46**, 5771 (2005).
42. S. Ko, C.-F. Yao, *Tetrahedron*, **62**, 7293 (2006).
43. L.-M. Wang, J. Sheng, L. Zhang, J.-W. Han, Z.-Y. Fan, H. Tian, C.-T. Qian, *Tetrahedron*, **61**, 1539 (2005).
44. M. Maheswara, V. Siddaiah, G. L. V. Damu, C. V. Rao, *Arkivoc*, **2**, 201 (2006).
45. M. M. Heravi, K. Bakhtiari, N. M. Javadi, F. F. Bamoharram, M. Saeedi, H. A. Oskooie, *J. Mol. Catal. A: Chem.*, **264**, 50 (2007).
46. L. Nagarapu, M. D. Kumari, N. V. Kumari, S. Kantevari, *Catal. Commun.* **8**, 1871 (2007).
47. S. Bhaskaruni, S. Maddila, W. E. van Zyl, S. B. Jonnalagadda, *ACS Omega*, **4**, 21187 (2019).

Research of tribological parameters of multilayer coating Ti/TiN/CrN-ml deposited on 1.2343 steel

V. Rupetsov^{1*}, S. Dishliev², G. Mishev¹, F. Franek³, M. Premauer³, L. Kolakleva⁴

¹ Plovdiv University "Paisii Hilendarski", 24 Tzar Assen Str., 4000 Plovdiv, Bulgaria,

² University of Food Technologies, 26 Maritsa Blvd. 4000 Plovdiv, Bulgaria

³ Austrian Excellence Center for Tribology, Viktor-Kaplan-Str. 2/C, 2700 Wiener Neustadt, Austria

⁴ Central Laboratory of Applied Physics, Bulgarian Academy of Sciences, 61 Sankt Petersburg Blvd. 4000 Plovdiv, Bulgaria

Received: February 25, 2020; Accepted: May 11, 2020

This work is dedicated to the experimental investigation of the tribological parameters of multilayer coating Ti/TiN/CrN-ml deposited on 1.2343 (X37CrMoV5-1) steel. This steel is mainly used for injection molds production. The improval of their wear resistance increases their living resources and betters the economic parameters of the company. Multilayer coating Ti/TiN/CrN-ml was deposited by the PVD method - reactive magnetron sputtering in Nanotech Group Ltd. - Plovdiv. It has a nanolaminate structure with a symmetric bylayer period of 22-30 μm . Methodology for experimental investigation of the tribological parameters of the multilayer coating Ti/TiN/CrN-ml is proposed which is based on "Ball on Flat Sliding Wear Test" tribosystem and determines the volume of the wear trace. The dimensions of the trace were determined by trace topography also using a microscope TESA VISIO-300. Coating thickness, nanohardness, friction coefficient and modulus of elasticity were measured. The influence of the main factors of the tribosystem (normal load, path and sliding speed) on the wear intensity is described.

Keywords: multilayer coating, wear intensity, PVD method

INTRODUCTION

Injection molds work under very hard regimes: high loads; high temperatures; high wear [1-4]. The tool resource is directly related to the wear of working surfaces. In order to increase the resource (life) of the injection molds, which is going to lead to a significant economic effect, it is necessary to take measures for increasing the hardness of the working surfaces of the tool and improving the wear resistance thereof [5]. About the enhancement of these two properties, the methods for deposition of hard wear-resistant coatings are the most effective [6-11]. Recently, the most widely use possess the coatings obtained by the process of Physical Vapor Deposition (PVD) [12, 13].

EXPERIMENTAL

Samples with cuboid shape: $25 \times 8 \times 5$ mm were prepared as follows (used face: 25×8 mm):

- Unhardened ground (marked as 2343A) with hardness 145 HB and surface roughness Ra 0.165 μm ;
- Hardened ground (marked as 2343B) with hardness 52 HRC and surface roughness Ra 0.112 μm ;
- Hardened polished (marked as 2343C) with hardness 52 HRC and surface roughness Ra 0.033 μm .

Static friction coefficient of the coating is 0.25 ± 0.03 (measured against polished SS 304 L). The common thickness of the layer is 3.6 ± 0.05 μm . First, it had a 0.9 μm adhesive layer consisting of Ti, followed by gradient TiN and TiCrN nanolayers. After that a nanolaminate was composed by alternating layers of TiN and CrN with thickness of 11÷15 nm each. The last layer is gradient 0.5 μm thick, which is changed from CrN through TiCrN to TiN (150 nm thick). The nanolaminate structure has the greatest influence on the coating properties and thus the signature "Ti/TiN/CrN-ml" was used (with the consent of the manufacturing company [14]). The temperature during the deposition process was 170°C.

Methods for experimental investigation of the tribological characteristics of the test samples

- *Method for experimental investigation of the wear resistance of thin hard coatings.*

The experimental studies were conducted by the "Ball on Flat Sliding Wear Test" friction scheme in horizontal orientation of the test surface [15]. One cemented-oxide ball (Al_2O_3) with diameter of 3 mm, fixed in a holder, was used as a counter-part. It rubs a linear reciprocating sample without lubricant, working in air at room temperature. The width of the arisen grooves was measured by a microscope: PC based contactless measurement

* To whom all correspondence should be sent:
E-mail: velko_r@abv.bg

system TESA VISIO-300 at $100 \times$ magnification (resolution: 0.001 mm).

The average width value b_{cp} was calculated:

$$b_{cp} = \frac{1}{n} \sum_{i=1}^n b_i, \text{ mm} \quad (1)$$

where:

n – number of the grooves (traces);

b_i – width of every particular groove.

For control of the measured width of the traces the topography of the sample surface in the traces area was generated (Figure 1). In accordance with the topographic results it was found that the error of measurement is less than 1%, which gives us to believe that the obtained results are correct.

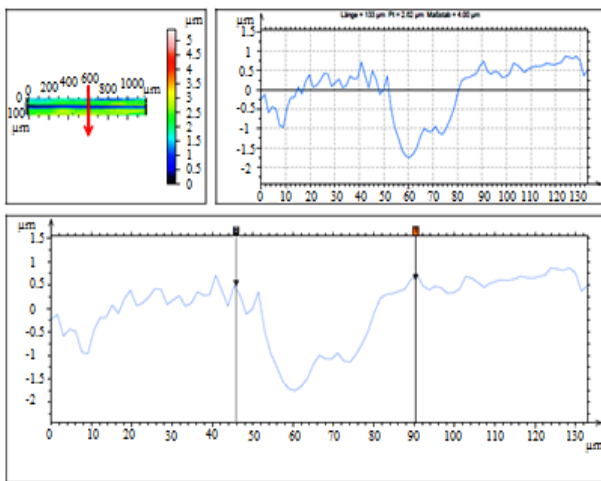


Fig. 1. Surface topography in the traces area

Traces width was used to determine the wear volume or volume of the traces which determines the wear rate I_w by the equation:

$$I_w = \frac{V}{F.L}, \text{ mm}^3/\text{N.m} \quad (2)$$

where:

V – wear volume (volume of the trace), mm^3 ;

F – normal load upon the ball, N ;

L - sliding distance between the ball and the sample, m .

The volume of the track was determined by the methodology described in [16].

Methods for investigation of thickness, nanohardness, elastic modulus and adhesion of the coating

The coating thickness h is a key complex indicator and was measured by a calotester elaborated in CLAP-Plovdiv. A ball with a diameter of 30 mm was implemented and the value

of h was calculated by the well-known formula [17,18]:

$$h = \frac{D^2 - d^2}{8R} \cdot 10^3, \mu\text{m} \quad (3)$$

where:

D - outer section diameter, mm ;

d - inner section diameter, mm ;

R - ball radius, mm (here: 15 mm).

The nanohardness and elastic modulus of the coating were determined using Compact Platform CPX (MHT/NHT) CSM Instruments in CLAP-Plovdiv. A diamond indenter (Berkovich type) was used and the results were interpreted by the Oliver and Pharr method [19].

The adhesion was tested by a Micro Scratch Tester (MST) module included in the same apparatus. A diamond indenter (Rockwell type) with a rounded apex of 200 μm was used [20].

RESULTS AND DISCUSSION

Experimental study of the wear resistance of a multilayer Ti/TiN/TiCrN-ml on 1.2343 steel

- *Experimental results for the influence of the normal load on the wear rate.*

Experimental studies were conducted under the following constant tribosystem parameters: sliding speed $V=10 \text{ mm/s}$; path $L=50 \text{ m}$. The normal load varied from 1 to 5 N . The wear of the investigated coating depends mainly of the normal load.

The experimental results were processed using the correlation analysis method. The calculated coefficient of determination shows the strength of the mutual relationships between I_w and F . For each value of normal load, three trials were performed and the mean arresting values were taken. In Table 1 the correlation equations of the wear intensity as a function of the normal load for all types of samples (12_2343A; 12_2343B; 12_2343C) and the corresponding coefficient of determination are given.

Table 1. Correlation dependencies of wear rate as a function of normal load.

Sample	Correlation equation	Coefficient of determination
12_2343A	$I_w=4.390.F+4.374$	$R^2=0.999$
12_2343B	$I_w=2.753.F+4.999$	$R^2=0.874$
12_2343C	$I_w=2.276.F-2.033$	$R^2=0.770$

At a coefficient of determination $R^2>0.7$ the mutual relation between I_w and F is very strong.

Figure 2 shows the dependence of I_w on F . With normal load increasing, the wear intensity also increases.

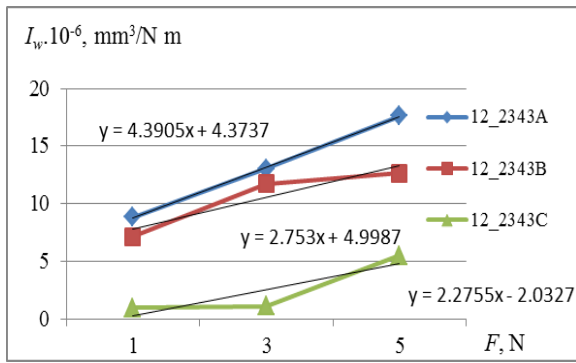


Fig. 2. Graphic dependencies of the wear rate as a function of the load $I_w=f(F)$

- *Experimental results for the influence of the path on the wear rate.*

Experimental studies were conducted under the following constant tribosystem parameters: sliding speed $V=10$ mm/s; normal load $F=1$ N. The path varied from 50 to 100 m.

The experimental results were processed using the correlation analysis method.

In Table 2 the correlation equations of the wear intensity as a function of the path for all types of samples (12_2343A; 12_2343B; 12_2343C) and the corresponding coefficient of determination are given.

Table 2. Correlation dependencies of wear rate as a function of the path.

Sample	Correlation equation	Coefficient of determination
12_2343A	$I_w=3.068.L+6.043$	$R^2=0.976$
12_2343B	$I_w=-1.438.L+8.371$	$R^2=0.937$
12_2343C	$I_w=0.394.L+0.562$	$R^2=0.999$

The negative value in the correlation equation of sample 12_2343B indicates an inverse proportional dependence of I_w on L . When L increases, I_w decreases. Figure 3 shows the dependence of the wear rate as a function of the path.

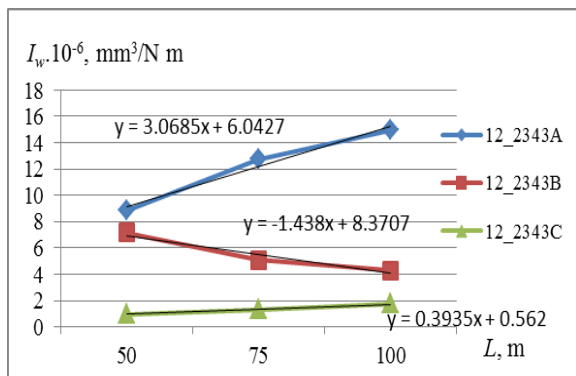


Fig. 3. Graphic dependencies of the wear rate as a function of the path $I_w=f(L)$.

- *Experimental results for the influence of the velocity on the wear rate.*

Experimental studies were conducted under the following constant tribosystem parameters: normal load $F=1$ N; path $L=50$ m. The sliding speed varied from 5 to 15 mm/s. In Table 3 the correlation equations of the wear intensity as a function of the velocity for all types of samples (12_2343A; 12_2343B; 12_2343C) and the corresponding coefficient of determination are given.

Table 3. Correlation dependencies of wear rate as a function of the velocity.

Sample	Correlation equation	Coefficient of determination
12_2343A	$I_w=-0.852.V+11.513$	$R^2=0.506$
12_2343B	$I_w=-0.609.V+8.929$	$R^2=0.610$
12_2343C	$I_w=0.111.V+1.992$	$R^2=0.010$

Figure 4 shows the dependence of the wear rate as a function of the velocity.

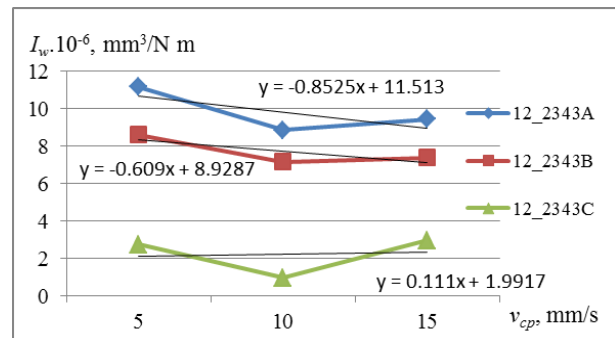


Fig. 4. Graphic dependencies of the wear rate as a function of the velocity $I_w=f(V)$.

Investigation of thickness, nanohardness, elastic modulus and adhesion of the coating

On the base of the calotester measurement, the calculated thickness is 2.92 μ m. A nanoindentation curve (load L vs. indentation depth D) of the test sample 12_2343C is shown in Figure 5. These parameters were specified: nanohardness $H = 25$ GPa; elastic modulus $E = 316$ GPa; maximal penetration depth $h_m = 336$ nm (at maximal indentation load of 50 mN). The maximal penetration depth is less than 15% of the entire coating thickness (2.92 μ m), which guarantees that the measured nanohardness is related only to coating without a substrate impact [21].

Figure 6a shows a diagram illustrating the adhesion measurement. The force F_n which presses the indenter is changed linearly to a maximum value of 30 N (the maximum load allowed by this equipment).

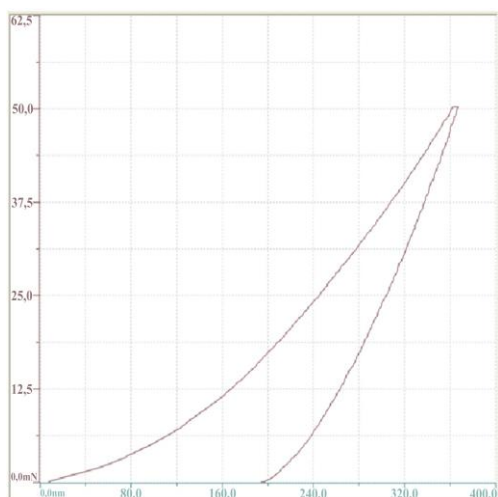


Fig. 5. Nanoindentation load/unload curve of sample 12_2343C [21]

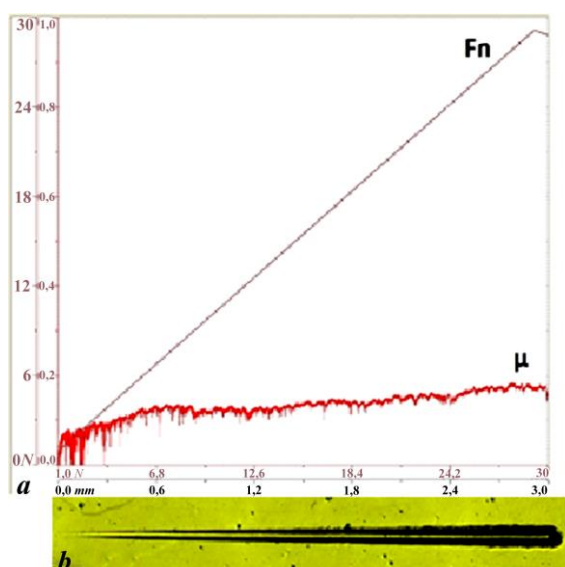


Fig. 6. Scratch test of sample 12_2343C: a) curves of the applied force F_n and friction coefficient μ ; b) view of the trace [21].

Along the trace, the friction coefficient was measured. It can be seen that it is lower than the above-mentioned static friction coefficient (friction coefficient at rest). This is consistent with the theory in mechanics where the friction coefficient at rest always has a larger value. Also, there is a difference in friction bodies material in both cases (polished SS 304L and diamond). The friction coefficient value is substantially constant (in the region of the tripping to the first damage), which can be explained by small tensions in the coating because of its nanolaminate structure, since they are unloaded between the individual layers. The first obvious damages in the coating were originated by applied force of 24 N (Figure 6b). This is the first critical load FC_1 . Since a delamination of the coating (an exposure of the substrate) in the

channel is not noticed, it is proven that the second critical force FC_2 is not reached up to the maximal applied force (30 N) [21].

CONCLUSIONS

- The main factors of a tribosystem: normal load, path and velocity have a significant impact on the wear of the multilayer nanolaminat coating Ti/TiN/CrN-ml deposited on 1.2343 steel. With normal load and path increasing the coatings wear increases as well. With velocity increasing the coating wear decreases.

- The quality of the surfaces, on which Ti/TiN/CrN-ml coating is deposited, has a significant impact on the wear of the coating. This multilayer coating doesn't change the initial surface roughness. When surface roughness decreases and/or hardness increases, the wear rate of the coating is reduced.

- The calculated wear rate of the Ti/TiN/CrN-ml coating deposited on a hardened polished surface is on average 4 times lower than that on a hardened ground surface and on average 6 times lower than that on an unhardened ground surface.

- The measured hardness and adhesion show a coating with a middle range hardness (on the edge of conventional limit for hard coatings: 20 GPa) and an excellent adhesion. Both parameters are benefited by this nanolaminate coating structure.

Acknowledgements: The authors would like to acknowledge the support of the National Programme "Young Scientists and Post-Doctoral Students" funded by the Bulgarian Ministry of Education and Science (MES).

REFERENCES

1. H. Rees, Mold Engineering, 2nd edn., Munich, Hanser Publishers, 2002.
2. T. Osswald, L.-S. Turng, P. Gramann, Injection Molding Handbook, 2nd edn., Munich, Hanser Publishers, 2008.
3. P. Unger, Gastrow Injection Molds – 130 Proven Designs, 4th edn., Munich, Hanser Publishers, 2006.
4. W. C. Oliver, G. M. Pharr, *J. Mater. Res.*, **7** (6) 1564 (1992).
5. E. A. Levashov, Ensuring the unity of measurements of physicomechanical and tribological properties of nanostructured surfaces, MISISISMAN, Moscow, 2010 (in Russian).
6. M. I. Jones, I. R. McColl, D. M. Grant, *Surf. Coat. Technol.*, **132** (2-3), 143 (2000).
7. M. J. Jung, K. H. Nam, L. R. Shaginyan, J. G. Han, *Thin Solid Films*, **435** (1-2), 145 (2003).

8. D. Kakaš, B. Škorić, A. Miletić, P. Terek, M. Vilotić, L. Kovačević, Proc. 7th Int. Conf. on Trib. (BALKANTRIB'11), Thessaloniki, Greece, 2011, p. 49.
9. P. Sveshtarov, R. Kakanakov, L. Kolaklieva, Ch. Bachchedjiev, T. Cholakova, E. Trifonova, S. Evtimova, Intern. Workshop NANO HARD, Velingrad, Bulgaria, 2007, p. 49.
10. S. Veprek, M. G. J. Veprek-Heijman P. Karvankova, J. Prochazka, *Thin Solid Films*, **476** (1), 1 (2004).
11. S. Zhang, D. Sun, Y. Fu, H. Du, *Surf. Coat. Technol.*, **167** (2-3) 113 (2003).
12. Ch. Pashinski, M. Angelov, V. Rupetsov, D. Petrov, P. Shindov, S. Dishliev, Proc. IV Int. Conf. Industr. Eng. Env. Protect. 2014 (IIZS 2014) Zrenjanin, Serbia, 2014, p. 356.
13. Ch. Pashinski, *Int. J. Sci. & Eng. Res.*, **4** (6), 870 (2013).
14. Nanotech Group Ltd., Coatings for molding and forming tools, available on www.nanotech-group.com/mouldingformingtools.html at 05. 08. 2019.
15. <http://www.astm.org/Standards/G133.htm>, ASTM G133 – 05 Standard Test Method for Linearly Reciprocating Ball-on-Flat Sliding Wear (2010).
16. V. S. Rupetsov, *Journal of Food and Packaging Science, Technique and Technologies*, **1**(4), 60 (2014) ISSN 1314-7773.
17. www.nanovea.com.
18. www.platit.com.
19. www.nanoscan.info.
20. www.csm-instruments.com.
21. V. S. Rupetsov, L. P. Kolaklieva, V. I Kopanov, V. A. Chitanov, Ch. O. Pashinski, S. I. Dishliev, *Journal of Food and Packaging Science, Technique and Technologies*, **IV** (6), 91 (2015).

Structural and electrochemical properties of Ni doped and MWCNTs coated ZnO thin films

F. Sarf

Çan Vocational School, Çanakkale Onsekiz Mart University, Çanakkale, Turkey

Received: April 06, 2020; Revised: April 24, 2020

Ni:ZnO and (Ni:ZnO)/MWCNT thin films were prepared *via* chemical bath deposition onto in-doped SnO₂ (ITO) substrates to investigate structural and electrochemical properties. An improving effect on the ZnO hexagonal würtzite structure due to a slight decrease in estimated grain sizes with nickel doping and multi-walled carbon nanotubes (MWCNTs) coating was established. Surface morphology transformed nanoflower to nanopetal with Ni doping and randomly distributed tubes were observed after MWCNTs coating. Surface impurities caused by Ni doping and nature of multi-walled carbon nanotube electron transport capability were influential in improving electrode performance. As a consequence, ZnO thin films can act as a substrate by using them as a seed layer with capacitive behaviour and high structural stability in electrochemical studies.

Keywords: ZnO; doping; MWCNT; structural; electrochemical

INTRODUCTION

Recently, as an alternative material to silicon, cheap metal oxides (MOs) have attracted attention in technological fields such as optoelectronic devices [1], gas sensors [2], Li-ion batteries [3] and catalytic devices [4]. Their physical and chemical properties can be altered by doping and/or C-based material nanocomposite. Energy levels of interstitial Zn²⁺ sites and oxygen vacancies, as well as surface shapes and particle sizes are effective in improving performance [5]. Relatively low-toxic NiO and ZnO exhibit rich redox reactions, high electrochemical stability and they are abundant in nature. Pure NiO and ZnO are p-type and n-type, respectively [6]. In addition, sp² bonded cylindrical and chemically stable multi-walled carbon nanotubes (MWCNTs) have good mechanical, optical and electrical properties [7]. MWCNTs are well-suited to obtaining nanocomposites whose charge storage properties have been improved with metal oxides [8].

Studies on ZnO as a seed layer have increased considerably since 2005, when it was first published in the literature [9]. The large majority of these studies aim at obtaining a large surface/volume ratio of ZnO nanowires or nanorods by benefitting from good ZnO seed layer crystallization and homogeneous surface morphology [10]. In other words, a ZnO seed layer with previsible c-axis orientation, good crystallinity and low lattice stress has been shown to allow obtaining of well-aligned ZnO nanorods/nanowires with uniform diameters and narrow density distributions [11]. In our

previous study, ZnS films have been produced on ZnO seed layers and the most obvious nanorod formations have been observed in S:7% films and photoluminescence spectra have yielded severely changed intensities with sulfur molar ratio [12].

To our best knowledge, there has been no study on the electrochemical properties of Ni:ZnO and Ni:ZnO/MWCNTs so far. Only Saravanakkumar *et al.* reported an investigation of photocatalytic and antimicrobial applications of NiO doped ZnO/MWCNT nanoparticles [13]. My goal is to investigate Ni doping and MWCNTs coating effect on the defect levels and electrochemical properties of ZnO seed layers.

MATERIAL AND METHODS

All reagents were of analytical grade and no further purification was used. ITO (In-doped Sn₂O₃) substrates were ultrasonically rinsed for 15 min in ethanol and hexane. Nanoflower-like ZnO films were used as a seed layer from our previous study and the same deposition process was realized [14]. Then, a molar ratio of silica gel:NiSO₄·6 H₂O = [2:1] was arranged in 100 ml of distilled water. Ammonia was added in order to obtain a basic aqueous solution. ZnO seed layers were immersed in this solution so Ni:ZnO films were obtained. T_{working}=75±5 °C and t = 15 min were growth temperature and dipping time parameters. Thereafter, enough amount of pure MWCNTs (>99%) (Nanografi Company/METU) was added in this solution and the same growth temperature and dipping time parameters were used. Finally, films were dried at room temperature for one day and were annealed at 600 °C for 2 h.

* To whom all correspondence should be sent:

E-mail: fatmaozutok@comu.edu.tr

X-ray patterns of the films were investigated by $\text{CuK}\alpha$ (1.5406 Å) Rigaku SmartLab X-ray diffractometer (XRD) adjusted to 40 mA and 45 kV. Film composition was observed by using JEOL-JSM-7100 F scanning electron microscope (SEM). Cyclic voltammetry measurements were conducted with 0.1 M $(\text{Fe}(\text{CN})_6)^{3-/4-}/\text{KCl}$ as probe at a scan rate of 50 mV/s. Nyquist plots of the samples were obtained in the following conditions: 10.0 mM $(\text{Fe}(\text{CN})_6)^{3-/4-}$ solution containing 0.10 M KCl in Faradaic mode at a formal potential of +0.18 V with frequencies between 10000 and 0.1 Hz and signal amplitude of 5 mV at room temperature. All characterization studies were realized at room temperature.

RESULTS AND DISCUSSION

XRD patterns and structural parameters of all films are shown in Fig. 1 and Table 1, respectively. The lack of impurities or secondary phase indicated high-quality film production. However, substrate (ITO) related peaks were determined so the adhesion level of the coated layers was found to be low. All films had hexagonal wurtzite ZnO structure according to JCPDS card no:36-1451 and they crystallized as polycrystalline. Diffraction peaks corresponding to (100), (002), (101), (102), (110) and (103) planes were observed from X-ray diffraction patterns. Ni^{2+} (ionic radius 0.63 Å) ions were substituted by Zn^{2+} (ionic radius 0.74 Å) due to nucleation agent alteration because ZnO peaks slightly shifted to higher 2θ and there was no other secondary phases of Ni. ZnO crystal quality

decreased with Ni doping which indicates that solubility limit of Ni in ZnO was very low at a temperature $\gg 100^\circ\text{C}$, as explained by Mandal *et al.* [15]. (Ni:ZnO)/MWCNT samples could be indexed by two phases; one was hexagonal wurtzite ZnO and another was hexagonal C (JCPDS card no:75-1621), as expected [16]. ZnO-related peaks intensity increase indicated that the chemical stability of MWCNTs could contribute to an increase in ZnO crystallinity. Grain size (D), lattice strain (ϵ) and dislocation density (δ) given in Table 1 were calculated by equations (1) – (3):

$$D = 0.94\lambda/\beta\cos\theta \quad (1)$$

$$\delta = 1/D^2 \quad (2)$$

$$\epsilon = (\beta/4)\cot\theta \quad (3)$$

Estimated grain size of the samples (D) was calculated from the XRD diffraction patterns by the Debye Scherrer equation, as shown in equation (1). The lattice parameters (a and c) of the samples were measured by this equation using (hkl) Miller indices:

$$1/d^2 = 4/3(h^2+hk+k^2/a^2) + 1/c^2 \quad (4)$$

It was determined that the ZnO structure stability was enhanced by Ni doping and MWCNTs coating process with no relative change in dislocation density and lattice strain as shown in Table 1 [17]. This might be useful in electrochemical studies when ZnO will be used as a substrate. The decrease in lattice parameters compared to hexagonal ZnO was related to the decrease in unit cell volume and grain size [18].

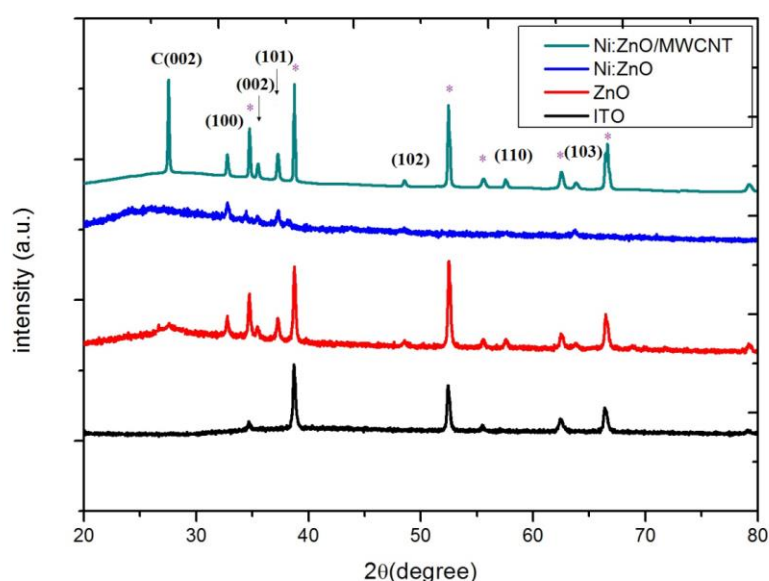


Fig. 1. XRD patterns of ZnO, Ni:ZnO and (Ni:ZnO)/MWCNT films (* sign associated to ITO related peaks)

Table 1. Structural parameters of ZnO, Ni:ZnO and (Ni:ZnO)/MWCNT films

(a)	2θ (°)	Lattice parameters (a, c)	D (Å)	D (nm)	Dislocation density (δ)	Lattice strain (ε) (%)
ZnO	37.25	3.20, 5.06	2.4137	27.5	13×10 ⁻⁴	6.182
Ni:ZnO	37.28	3.20, 5.06	2.4116	21.2	22×10 ⁻⁴	7.047
(Ni:ZnO)/MWCNT	37.27	3.19, 5.06	2.4124	22.3	20×10 ⁻⁴	6.867

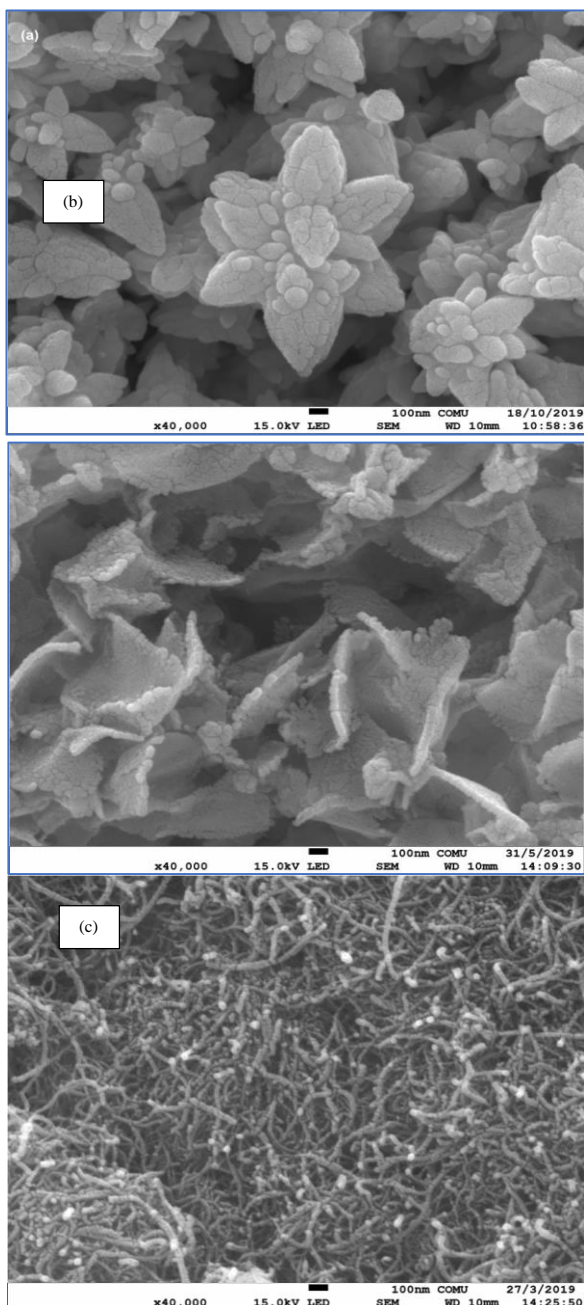


Fig. 2. SEM images of a) ZnO, b) Ni:ZnO and c) (Ni:ZnO)/MWCNT films.

SEM images of the films are illustrated in Fig. 2. All films have a relatively smooth and non-crack surface. Throughout the scanned area, there are no cluster forms, especially expected on the Ni:ZnO surface. Nanopetal formations are observed in the Ni doped ZnO samples, although ZnO films had nanoflower shapes due to incorporation of Ni²⁺ ions into ZnO [19]. While the dimensions of nanoflower ZnO forms are partially different from each other, homogeneous distribution of grain sizes is seen by Ni doping. Although the extra MWCNTs dispersion process was not implemented, random dispersed and relative non-agglomerative tube forms are found on the Ni: ZnO surface with MWCNTs coating. The cyclic voltammogram curves of ZnO, Ni:ZnO and (Zn,Ni)O/MWCNT electrodes to evaluate charge transfer properties are shown in Fig. 3. All samples have capacitive behaviour. They show a pair of redox peaks that were attributed to the (Fe(CN)₆)³⁻/(Fe(CN)₆)⁴⁻ redox process. The area surrounded by the CV curve was enhanced by Ni doping because Ni²⁺ (0.55 Å) ionic radius was smaller than Zn²⁺(0.74 Å) ionic radius so more surface impurities might occur. It caused an increase in the capacitive performance of ZnO electrode [20]. MWCNTs remarkably improved the reactivity of ZnO for oxidation process with their high current response, as shown in Table 2. Synergy between MWCNTs and ZnO/NiO caused an improved transport of electrons, therefore more electro-active sites might be created by MWCNTs coating due to the high conductive nature of MWCNTs [21]. These results were in agreement with previous studies [22]. The specific capacity of the electrodes was measured by equation (5):

$$C = i_{av} / v \times m \tag{5}$$

where C is specific capacitance (F/g), *i*_{av} is the average current (A), *v* is the potential sweep rate (V/m) and *m* is the mass of the active electrode (g). values.

Table 2. Cyclic voltammogram data of ZnO, Ni:ZnO and (Ni:ZnO)/MWCNT electrodes

Sample	Anodic peak potential (V) E_{pa}	Cathodic peak potential (V) E_{pc}	Anodic peak current (10^{-4} A) I_{pa}	Cathodic peak current (10^{-4} A) I_{pc}	Peak potential separation
ZnO	0.410	0.025	0.185	-0.118	193 mV
(Zn,Ni)O	0.550	0.043	1.628	-1.429	253 mV
(Zn,Ni)O/MWCNT	0.495	0.095	2.182	-1.923	200 mV

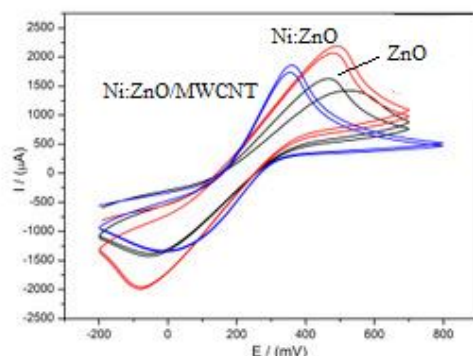


Fig.3. Cyclic voltammogram of ZnO, Ni:ZnO and (Ni:ZnO)/MWCNT electrode

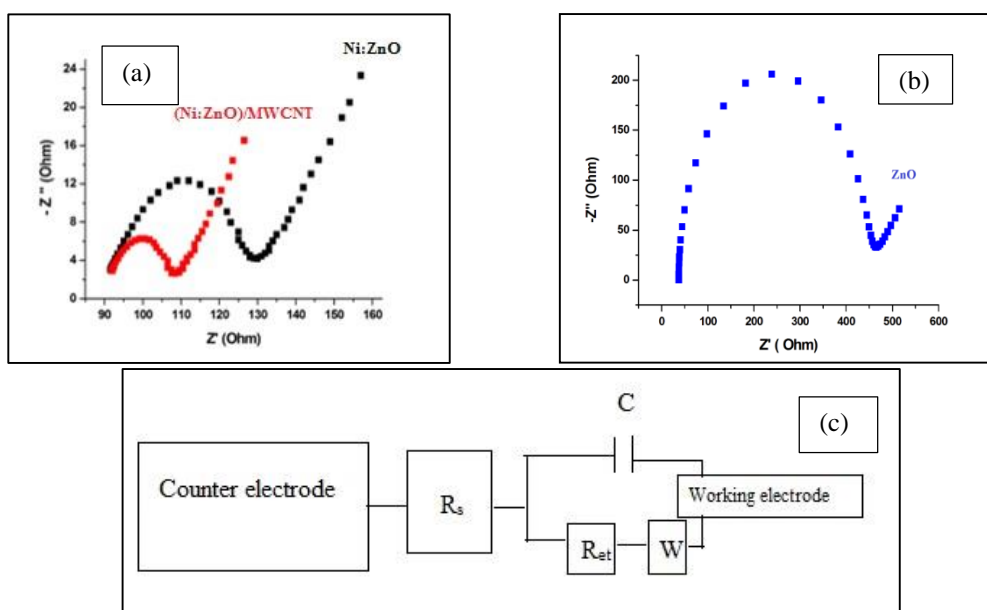


Fig. 4. Nyquist plot between a real impedance (Z') and imaginary impedance (Z'') of a) ZnO, b) Ni:ZnO and (Ni:ZnO)/MWCNT electrodes, c) the circuit used for fitting the impedance

Although no dramatic change was observed, the specific capacitance values increased with Ni doping and MWCNTs coating which indicated that low concentration of doping element and coating material has no effect on the the specific capacitance. Electrochemical impedance spectroscopy (EIS) is an effective technique to investigate reactions at the electrolyte/electrode interface. Nyquist plots of the electrodes are shown

in Fig. 4. There is a circuit diagram in Fig. 4 (c) where R_s , R_{et} , W and C are ohmic resistance, electron charge transfer resistance, Warburg impedance and double layer capacitance, respectively. Nyquist plots consist of two parts explaining charge transport and diffusion process corresponding to the semicircle in the high-frequency region and the Warburg line in the low-frequency region, respectively [23]. In the high-

frequency region, the electron charge transfer resistance (R_{ct}) modified by Ni doping and MWCNT coating and resistance magnitudes can be sorted as $R_{ZnO} > R_{Ni:ZnO} > R_{Ni:ZnO/MWCNT}$. ZnO electrode interfacial electron transfer rate was lower than that of the other two electrodes. Grain size decrease was associated with decreasing resistances from the semicircle in the high-frequency region [24]. Grain boundaries of samples were effective in the low-frequency region with changing Warburg line extrapolation in the limit of low frequency that measured as the double layer capacitance [25]. Relative Warburg line extrapolation shift showed that Ni doping had a role at grain boundaries of Ni:ZnO and (Ni:ZnO)/MWCNT. In this phenomenon, surface impurities revealed by Ni^{2+} ions might have a major effect at grain boundaries and interfaces, as reported by other researchers [26].

CONCLUSION

Polycrystalline nanoflower-shaped ZnO films were deposited by chemical bath to determine Ni doping and MWCNTs coating effect on the structural and electrochemical properties. All films have ZnO hexagonal structure while characteristic C(002) was observed in MWCNT coated Ni:ZnO films. Surface impurities occurred by Ni^{2+} ions, Zn^{2+} sites and oxygen vacancies (V_O). High electron transport character with MWCNTs coating contributed to improvement of electrochemical properties. It was shown that ZnO thin films used as a seed layer will supply high structural stability and electro-active surfaces for electrochemical studies. This paper may provide a new path for future electrochemical studies featuring ZnO seed layers to promote its use in the production of capacitors and Li-ion batteries.

Acknowledgement: This research was supported by the Council of Scientific Research Project of Çanakkale Onsekiz Mart University (ÇOMU) (Grant number: FBD-2017-1321).

REFERENCES

1. A. B. Djurisić, A. M. C. Ng, X. Y. Chen, *Progress in Quantum Electronics*, **34**, 191 (2010).
2. F. Sarf, Metal Oxide Gas Sensors by Nanostructures, Gas Sensors, Intech Open Horizons Publishing Company, London, 2020.
3. K. Cao, T. Jin, L. Yang, L. Jiao, *Mater. Chem. Front.*, **1**, 2213 (2017).
4. T. Block, M. Schmücker, *Solar Energy*, **126**, 195 (2016).
5. X. Xing, R. Liu, K. Cao, U. Kaiser, C. Streb, *Chem. Eur. J.*, **25**, 11098 (2019).
6. A. M. Akyuzlu, F. Dagdelen, A. Gultek, A. A. Hendi, F. Yakuphanoglu, *Eur. Phys. J. Plus*, **132** (2017).
7. K. S. Ibrahim, *Carbon Letters*, **14**, 131 (2013).
8. Y. Hu, C. Guo, Intech Open Horizons Publishing Company, London, ISBN 978-953-307-566-2, 2011.
9. R. B. M Cross, M. M. De Souza, E. M. Sankara Narayanan, *Nanotechnology*, **16**, 2188 (2005).
10. J. Song, S. Lim, *J. Phys. Chem. C*, **111**, 596 (2007).
11. M. Z. Toe, N. A. H. N. Jusoh, S. Y. Pung, K. A. Yaacob, A. Matsuda, W. K. Tan, S. S. Han, *Materials Today: Proceedings*, **17**, 553 (2019).
12. F. Özütok, E. Yakar, *Journal of Applied Spectroscopy*, **85**, 5191 (2018)
13. D. Saravanakumar, R. Karthika, S. Ganasaravanan, S. Sivaranjani, S. Pandiarajan, B. Ravikumar, A. Ayeshamariam, *IOSR Journal of Applied Physics (IOSR-JAP)*, **10**, 73 (2018).
14. F. Özütok, S. Demiri, *Digest Journal of Nanomaterials and Biostructures*, **12**, 309 (2017).
15. S. K. Mandal, A. K. Das, T. K. Nath, D. Karmakar, *Appl. Phys. Lett.*, **89**, 144105 (2006).
16. R. Rai, T. Triloki, B. K. Singh, *Appl. Phys. A*, **122**, 774 (2016).
17. A. K. Rana, Y. Kumar, P. Rajput, S. N. Jha, D. Bhattacharyya, P. M. Shirage, *ACS Applied Materials & Interfaces*, **9**, 7691 (2017).
18. M. G. Ortiz, E. B. Castro, S. G. Real, *J. Solid State Electrochem.*, **21**, 2339 (2017).
19. H. Lee, B. Kim, S. Kim, Y. Park, S. Jung, *Int. J. Mol. Sci.*, **19**, 3830 (2018).
20. A. Chandrasekaran, T. Prasankumar, Sujin P. Jose, K. Anitha, C. Ekstrum, J. M. Pearce, J. Mayandi, *Chemistry Select.*, **2**, 9014 (2017).
21. Ü. Alver, A. Tanrıverdi, *Appl. Surf. Sci.*, **378**, 368 (2016).
22. P. Norouzzadeh, Kh. Mabhouti, M. M. Golzan, R. Naderali, *Journal of Materials Science: Materials in Electronics*, **1**, 13 (2019).
23. O. E. Fayemi, A. S. Adekunle, E. E. Ebenso, *Sensing and Bio-Sensing Research*, **13**, 17 (2017).
24. F. Özütok, E. Yakar, *Journal of New Materials for Electrochemical Systems*, **21**, 119 (2018).
25. S. Hu, J. Nozawa, H. Koizumi, K. Fujiwara, S. Uda, *Cryst. Growth Des.*, **15**, 5685 (2018).
26. Y. Zhao, M. Zhou, Z. Lv, Z. Li, J. Huang, X. Liang, J. Min, L. Wang, *Superlattices and Microstructures*, **49**, 549 (2011).
27. M. Y. Ali Khan, M. K. R. Tanveer Karim, A. M. M. Rahman, M. M. Kamruzzaman, *Heliyon*, **6**, e03588 (2020).

Microbial biodegradation as an option for waste utilization during long-term manned space missions

Hr. Najdenski¹, V. Hubenov¹, I. Simeonov¹, V. Kussovski¹, L. Dimitrova¹, P. Petrova¹,
P. Angelov², L. Kabaivanova^{1*}

¹ The "Stephan Angeloff" Institute of Microbiology, Bulgarian Academy of Sciences, Acad. G. Bonchev Str., Bl. 26, 1113 Sofia, Bulgaria

² Space Research and Technology Institute, Bulgarian Academy of Sciences, Acad. G. Bonchev Str., Bl. 1, 1113 Sofia, Bulgaria

Received: January 25, 2020; Revised: February 12, 2020

Planned space flights in foreseeable future to Mars pose many important issues to be solved by nowadays science, especially the problem of organic wastes accumulated in large quantities. The flight from Earth to Mars takes about 520 days. The crew possibly could consist of 6 cosmonauts, each of them needing daily: oxygen (1 kg of liquid), water (1-2 litres), food (2-3 kg). The total weight is about 5 kg/day or 30 kg/day for the entire crew. During long-term manned missions, the wastes are prohibited to be disposed of in space. They must be recycled. It is known that specific bacteria are able to convert waste substrates into usable nutrients and minerals. The enormous challenge is: reducing the volume of wastes to generate liquid and gaseous fractions which could be used in the production of food, water and oxygen. Simultaneously, some biogas is obtained as a source of energy. We present the development of a process of biodegradation of cellulose containing substrates similar to personal hygiene materials for cosmonauts by selected non-pathogenic bacteria. Experiments were conducted in terrestrial conditions where a degree of biodegradation of 72% of cellulose containing substrates at anaerobic, mesophilic conditions was realized. The selected bacterial community was genetically identified. The most abundant species were *Bacteroides oleiciplenus*, *Clostridium butyricum*, and *Ruminiclostridium papyrosolvens*. Concentration and profile of volatile fatty acids accompanying the biodegradation process in a bioreactor were also followed.

Keywords: Cellulose containing wastes, Biodegradation, Bacterial community, Long-term manned space missions

Abbreviations: MELISSA: Micro-Ecological Life Support System Alternative; ESA: European Space Agency; AD: anaerobic digestion; ADS: anaerobic digestion sludge; DBD: degree of biodegradation; D: dilution rate; VFA: volatile fatty acids.

INTRODUCTION

Research related to Life Support Systems for long-term space flights is deepening in recent years. Due to vast operating distances and the resulting long travel times the maintenance of the crew has to be fully accomplished on board [1]. For the whole period the cosmonauts will require oxygen, water and food, as well as hygienic materials. After use they have to be recycled. An international group of experts is already working to create a closed micro-environmental ecosystem - the Micro-Ecological Life Support System Alternative (MELISSA), project of the European Space Agency (ESA) [2]. In it organic waste will be utilized by different groups of bacteria in special bioreactors. The closed system MELISSA is inspired by aquatic ecosystems and is designed as a model for studying regenerative life-support systems for long-term space missions. The split structure of the cycle and the choice of several microbial processes have been made to simplify the

behavior of this artificial ecosystem. The leading elements are the production of food, water and oxygen from the organic waste of the mission. The choice of this split structure is conditioned by high reliability and safety requirements and the limited space for realization. Among the wastes that are formed in the conditions of manned space flight, a significant proportion is spent on personal hygiene. The problem of waste utilization is very acute as there is no shower on board and wipes and towels are the most common means of hygiene procedures, forming consecutively the largest waste volume. Together with this a necessary element of the closed system of manned spacecraft are considered greenhouses for the reproduction of the vegetative part of the diet of cosmonauts. Vegetable remains become another waste for recycling [3]. In addition, the waste contains products of human body secretion, which are dangerous in the sanitary-epidemiological sense.

* To whom all correspondence should be sent:
E-mail: lkabaivanova@yahoo.com

In the perspective of interplanetary flights based on the requirements of planetary quarantine, it is not possible to carry out the contaminated with microorganisms' debris beyond the spacecraft. On Earth, the accumulation of these residues may cause serious environmental problems. At the same time, it may serve as a significant resource, as the high organic content of vegetable residues and other cellulose containing wastes could make them a potential source for renewable energy [4].

Anaerobic digestion of organic wastes is a very attractive biotechnology also in the field of the renewable energy sources and biofuels. Anaerobic digestion is a multi-step biotechnological process with H_2 as a non-accumulating intermediate product. Recently, the interest in H_2 production through anaerobic digestion has increased [5]. Lignocellulose degradation is indeed a process with complex regulation, as has already been demonstrated for the bacterial genera *Caldicellulosiruptor*, *Fibrobacter* or *Ruminococcus*. In the same time, the presence of other proteins involved in chitin degradation (chitinases and *N*-acetylglucosaminidases) and starch catabolism (such as amylases, maltases and fructofuranosidases) in the bacterial proteomes during growth in cellulose that we have observed, suggests that cellulases and hemicellulases may share their regulatory systems with other proteins [6].

Co-cultures often present improved performance over corresponding monocultures. The mechanisms involved may include enhanced substrate utilization, overcoming of nutritional limitations, reduction of the levels of scavengers and achieving superior overall activity, conversion and enzymatic action. In lignocellulose degradation processes, co-cultures of particular nature are superior to monocultures, as they allow division of labor in the metabolic processes that are required by the substrate. Clearly, microorganisms often lack some key metabolic pathways, which may be supplemented by others [7]

Various materials for cleaning and absorbing, including cotton towels, paper towels and napkins, "wet wipes" and gauze, are used on the International Space Station. The weekly schedule of astronauts includes cleaning the station, which involves decontamination of many surfaces with wet wipes. This leads to the accumulation of a large amount of cellulose materials, as well as other similar items such as packaging of the used provisions. To be recycled, the used textile and paper materials must be collected separately. This allows for the development of different technologies for the re-use of waste in small closed systems such as the spacecraft. Recovery of various organic wastes in

space flight is an actual problem of modern astronautics and future interplanetary and other long-duration missions. Currently, organic waste is incinerated in the Earth's atmosphere during cargo vessels reentry. The maintaining of a closed ecosystem in the spaceship is considered as one of the main ways of ensuring the food and air for the crew in the long-term missions. Accordingly, ESA started to develop a high-tech bio-waste recycling system for space missions, stepping on the biological approach for recycling that included collection of data under real operating conditions. Its aim is to construct autonomous habitats in deep space, supplying astronauts with fresh air, water and food through continuous microbial recycling of organic wastes [8].

For the purpose of MELISSA the highest degree of biomass liquefaction must be achieved for more complete nutrient recovery in the following compartments. Therefore, the most challenging part is to find out the most suitable way for solid waste degradation and liquefaction [2].

The species that degrade cellulose belong mainly to the genera *Cytophaga*, *Cellulomonas*, *Cellvibrio*, *Bacillus*, *Clostridium* and *Sporocytophaga* [9]. The strictly anaerobic, thermophilic bacterium *Ruminiclostridium thermocellum* is the microorganism with the fastest documented growth rate on the recalcitrant substrate crystalline cellulose [10]. These organisms achieve a remarkable ability by forming very large extracellular multi-enzyme complexes, known as cellulosomes. Similar complexes are formed by related Clostridia (such as *Clostridium acetobutylicum*, *Clostridium cellulolyticum*, *Clostridium cellulovorans*, *Clostridium josui* and *Clostridium papyrosolvens*) and other anaerobic cellulose-degrading bacteria, such as *Acetivibrio cellulolyticus*, *Pseudobacteroides cellulosolvans* and *Ruminococcus albus* [11]. Several methods had been applied to investigate their microbial diversity: clone library of 16S rRNA genes, denaturing gradient gel electrophoresis (DGGE) analysis, fluorescence *in situ* hybridization (FISH), etc. Metagenomics is an efficient method for determining the complex microbiota structure and performing metabolic mechanism analysis. It is applied for elucidation of community structure and metabolic pathway analysis to determine the mechanism of cellulose degradation in natural consortia [12, 13]. The aim of our study was to develop a laboratory approach for bacterial degradation of cellulose containing hygiene materials similar to those used by the crews of spacecrafts accumulated during long-term space missions.

EXPERIMENTAL

Analytical methods

Cellulose concentration was estimated by a spectrophotometer using anthrone reagent according to Updegraff [14].

Volatile fatty acids concentrations were measured by a gas chromatograph "Focus GC" Thermo Scientific, equipped with a split/splitless injector, TG-WAXMS (length -30 m, ID - 0.25 mm, film - 0.25 μ m) column and FID.

Released gas volume was determined using a graduated cylinder in the gas holder; concentration of methane (CH₄) - with the automatic gas analyzer "Dräger", X-am 7000, carbon dioxide (CO₂) and hydrogen (H₂) - with Gasboard gas analyser (China 3100D).

Experimental conditions

Working methane and hydrogen generating anaerobic digesters were used as a source of bacterial inocula. Laboratory bioreactors with working volumes of 1 dm³, 2 dm³ and 14 dm³, at a speed of the stirrer 50 rpm were involved. The first two operated in a mesophilic mode (35-37 °C), and the third - in a thermophilic (55 °C) mode. The temperature was measured and controlled by electronic regulators, the accuracy of the regulation (in normal operation) was ± 0.5 °C. The stirring was done by constant electric motors and was about 100 rpm for all bioreactors. After feeding, each time a purge was made to ensure an anaerobic environment. Substrates used were filter paper, microcrystalline cellulose and medical gauze. Whatman no. 1 filter paper was used as single rectangular pieces.

Anaerobic cultivation techniques and appliances were used. The bacterial inoculum from the laboratory bioreactors was cultured at 37 °C and 55 °C, respectively, under anaerobic conditions created in anaerobic jars of anaerobic gas-generating gasPak™ EZ sachets for anaerobic container system (Becton Dickinson, 260678). The anaerobic conditions of the environment were proved by indicators (Merck, 1.15112.0001). Process duration was 7-30 days.

Cultivation media

For 1 L of 520 DSMZ medium preparation the following components were required: 1.30 g of (NH₄)₂SO₄, 1.50 g of KH₂PO₄, 2.90 g of K₂HPO₄ \times 3 H₂O, 1.25 ml of FeSO₄ \times 7 H₂O solution (0.1% w/v in 0.1 N H₂SO₄), 1.00 ml of a solution of (0.50 g of Na-resazurin solution (0.1% w/v), 0.20 g of MgCl₂ \times 6H₂O, 75.00 mg of CaCl₂ \times 2 H₂O, 6.00 g of cellobiose (the composition is presented below),

2.00 g of yeast extract, 1.50 g of Na₂CO₃ and 0.50 g of L-cysteine-HCl \times H₂O.

For 990 ml of SL-10 trace elements: 10.00 ml of HCl (25%, 7.7 M), 1.50 g of FeCl₂ \times 4 H₂O, 70.00 mg of ZnCl₂, 100.00 mg of MnCl₂ \times 4 H₂O, 6.00 mg of H₃BO₃, 190.00 mg of CoCl₂ \times 6 H₂O, 2.00 mg of CuCl₂ \times 2 H₂O, 24.00 mg of NiCl₂ \times 6 H₂O and 36.00 mg of Na₂MoO₄ \times 2 H₂O.

For 1 L of 122 DSMZ medium, the following components were required: 1.30 g of (NH₄)₂SO₄, 2.60 g of MgCl₂ \times 6 H₂O, 1.43 g of KH₂PO₄, 5.50 g of K₂HPO₄, 0.13 g of CaCl₂ \times 2 H₂O, 6.00 g of Na₂- β -glycerol phosphate (0.1% w/v in 0.1 N H₂SO₄), 0.25 g of reduced L-glutathione, 4.50 g of yeast extract, 0.50 ml of Na-resazurin solution (0.1% w/v) and 5.00 g of cellobiose. Cultivation temperature was 37°C and 55°C.

Metagenome sequencing

Genomic DNA was extracted using a GeneJET genomic DNA purification kit (Thermo Fisher Scientific). DNA concentration and quality were measured using QB 3000 spectrophotometer. Illumina 16S library construction was performed using 16S rRNA gene specific primers, followed by MiSeq 2 \times 300 bp sequencing, and FastQC quality control (Macrogen Inc., South Korea). The assembly results showed that quality-filtered data contained 43 056 268 total bases and 96 208 read counts. The percentage of Q20 quality reads was 97.03%.

Statistical analysis

The data are average from three independent experiments. Bars \pm SD (standard deviation). The values are statistically significant ($p < 0.05$).

RESULTS AND DISCUSSION

Biodegradation of cellulose containing substrates by anaerobic microbial consortia

With the purpose of isolating cellulolytic microorganisms, batch anaerobic processes were carried out. Inoculum was taken from a working bioreactor containing powdered/microcrystalline cellulose (15 g/l) at a mesophilic regime. Bacterial communities were taken from the mesophilic and thermophilic bioreactors containing the same substrates but operating under different temperature regimes. Experiments at a mesophilic regime started with substrates: Whatman cellulose and filter paper. At the 15th day of the process partial degradation was registered (Figure 1 B), while after 20 days all pieces of filter paper disappeared (Figure 1C).



Fig. 1. Microbial degradation of filter paper pieces: at the beginning of the process (A), after 15 days (B) and after 20 days (C).

Biodegradation of cellulose containing components similar in composition to waste hygiene materials used by space crews was estimated. Lignocellulosic biomass possesses an inherent complexity and heterogeneity, so the efficient biodegradation requires activities of different types of hydrolytic enzymes and involvement of complex microbial communities that can work efficiently and synergetically. The generation of a complex microbial consortium is a promising approach for the efficient biomass decomposition [15].

The experiments continued by biodegradation of medical sterile gauze at anaerobic mesophilic conditions for 20 days (Fig. 2). Gauze, used by cosmonauts as sanitary napkins, consists of natural cellulose fibers (70-100%) and inclusions of synthetic polymeric materials (up to 30%).

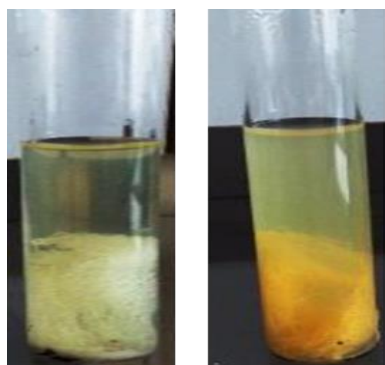


Fig. 2. Biodegradation of gauze at anaerobic mesophilic conditions for 10 days

Biodegradation of gauze at anaerobic mesophilic conditions was realized also at thermophilic conditions. The comparison did not reveal a significant difference in the residual cellulose between the 14th and 21st day at the two different temperatures. The mesophilic bacterial community after 14 days degraded cellulose to a greater extent (about 59%) compared to the thermophilic (about

35%), so we focused our attention on mesophilic processes. But for space flight conditions, maintaining a high temperature requires energy consumption and is not life-supporting for astronauts in long flights as it is one of the limiting factors. And our results showed the opposite. It is known that thermophilic cellulolytic bacteria of the genus *Clostridium* are the most promising agents capable to destroy cellulose with various degrees of ordering. But for the conditions of a space flight, such energy consuming process is not applicable.

Single colonies were isolated (using Mueller Hinton agar and TSA) at the end of the biodegradation process. They showed cellulolytic activity. Presence of spore-forming rod-shaped clostridial forms was established, following the light microscopic observations (Figure 3). From the photodocumentation, the presence of Gram - (-) spore-forming rod-shaped (short and long) and Gram - (+) clostridial typical forms is observed. Some of the cells are in the process of division, so they look bipolar.

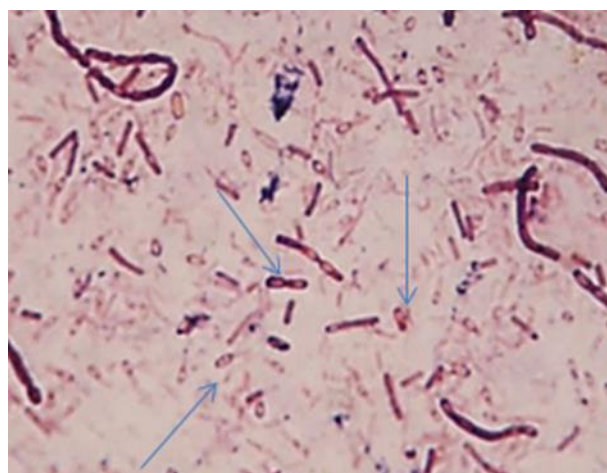


Fig. 3. Light microscopy image of the bacterial consortium realizing biodegradation of cellulose.

Stock cultures were prepared and preserved at -20°C with a cryoprotector for further use.

Next experiments were conducted for degradation of cellulose containing wastes using the selected microorganisms.

Cellulose degradation, gas formation and volatile fatty acids accumulation

The dynamics of the degradation of a model substrate (filter paper) by the selected mesophilic bacterial community showed most intense degradation during the first 17 days of the process. The correlation between substrate degradation and biogas accumulation is presented on Figure 4.

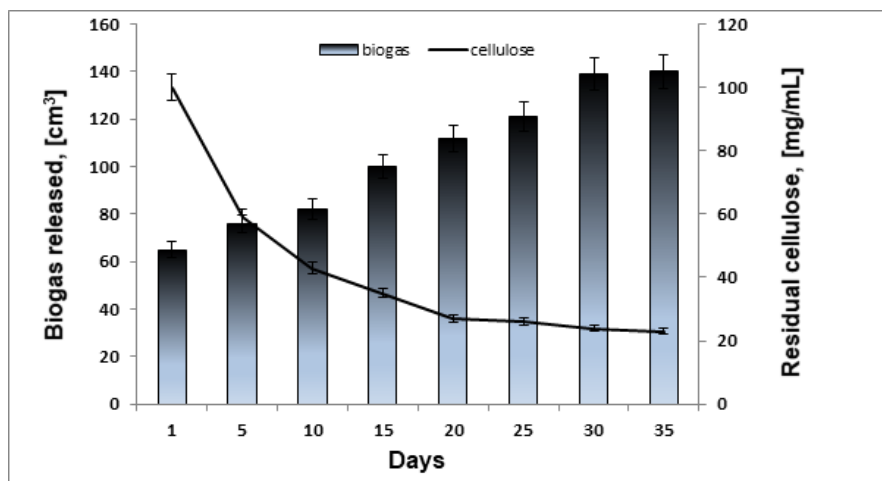


Fig. 4. Dynamics of cellulose biodegradation in relation to biogas released.

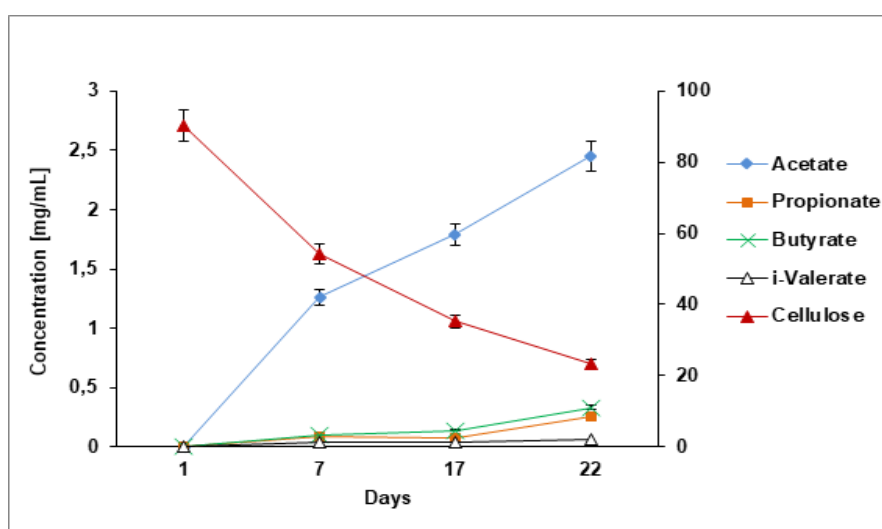


Fig. 5. Profile of fatty acids at the end of the process of biodegradation.

The degree of cellulose biodegradation was determined to be 72% at 37 °C. The process was accompanied by biogas release, in which volume percent of hydrogen was calculated to be up to 45%. These results are comparable with those obtained by Chu *et al.* [16] and Lay [17], which might show that the degradation process is paired with hydrogen production. In that case we could suggest that the cellulose degradation was realized by mixed microbial consortia *via* mixed acid fermentation. Hydrogen is known as a clean energy resource and is one of the most important elements. The biological production of hydrogen by using wastes and other biomass as raw materials has been attracting attention as an environmentally friendly process that does not consume fossil fuels. While conversion of biomass resources to hydrogen gas by fermentation has been extensively studied, most studies have been carried out with pure cultures of the isolated strains [18].

Profiles of volatile fatty acids - a major metabolic product in anaerobic biodegradation were investigated. Volatile fatty acids can serve as substrates for the next step in a closed micro-environmental life support system, such as MELISSA. The concentration of VFA was followed during the fermentative process. The biodegradation of the cellulosic material lead to accumulation in the medium mainly of acetate, followed by butyrate and propionate in the process with inoculum from a mesophilic hydrogenic reactor and substrate filter paper (Figure 5).

This result is also obtained from other authors [16, 19, 20]. According to Zang *et al.* [19], the concentration of acetate increased as pH dropped below 6.5 and decreased as pH and butyrate increased. This result suggests that the variation in pH led to changes in the distribution of fermentative products. Hydrogen production and decrease in pH were accompanied by the formation of VFA and ethanol throughout the cellulose-consuming

fermentation. In our experiments the total concentration of VFAs was 3 mg/ml, acetate was 80% among other VFA detected.

Metagenomics

We continued with identification by molecular-biological methods the bacterial population which can degrade cellulose from different sources as filter paper and other hygienic materials.

To investigate the microbial diversity involved in the production of hydrogen from cellulose, a metagenome profiling was performed (Figure 6).

Our results showed that cellulose degradation is most probably due to the presence of members of genera *Clostridium* (DNA copies 5480), *Bacteroides* (DNA copies 4263), and *Ruminiclostridium* (DNA copies 2590). Among them, the most spread species are *Clostridium butyricum*, *Bacteroides oleiciplenus* and *Ruminiclostridium papyrosolvens*. About ten times less in the sample were the representatives of the genera *Dendrosporobacter*, *Oscillibacter* and

Caproiciproducens with the most abundant species *O. ruminantium*, *Capr. galactitolivorans* and *D. quercicolus*.

A number of structurally stable multispecies consortia with high cellulose-degrading activity were obtained by successive culture enrichments using agricultural biomass as the sole carbon source under meso- and thermophilic conditions. These symbiotic consortia can efficiently degrade various cellulosic materials. Ruminal methanogenic communities were composed of hydrogenotrophic methanogens dominated by the order *Methanobacteriales* regardless of the host species. The methanogenic communities changed significantly during the enrichment procedure, but still the strict hydrogenotrophic *Methanobacteriales* and *Methanomicrobiales* were the predominant orders in the enrichment cultures [21].

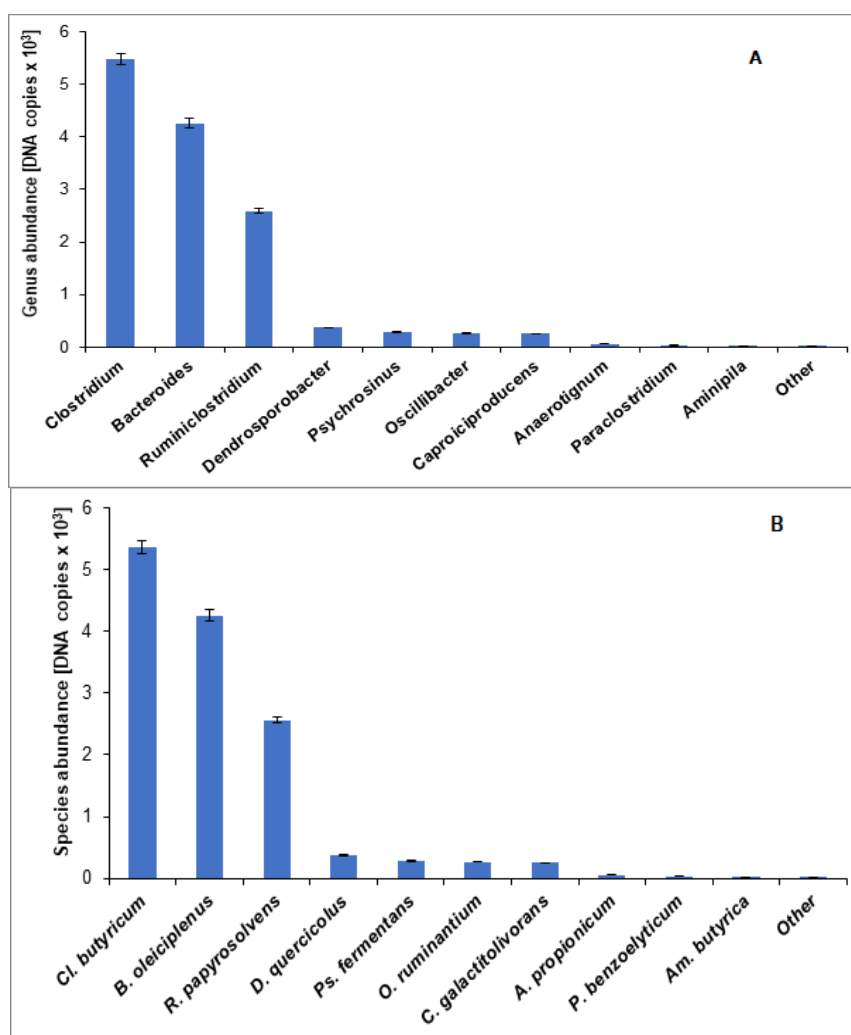


Fig. 6. Genus (A) and species (B) abundance in the investigated microbial consortium.

From the cellulose degrading bacteria, *Bacteroides oleiciplenus* is a representative of a group of microbes that constitute the most abundant members of the intestinal microflora of mammals. This organism produces many extracellular enzymes which assist in the breakdown of complex plant polysaccharides such as cellulose and hemicellulose and host-derived polysaccharides such as mucopolysaccharides. *Clostridium aciditolerans* is an obligately anaerobic, spore-forming, moderately acid-tolerant bacterium. The strain JW/YJL-B3T utilized beef extract, casamino acids, peptone, tryptone, arabinose, cellobiose, fructose, galactose, glucose, lactose, maltose, mannose, raffinose, ribose, sucrose, xylose, pyruvate, glutamate and inulin as a carbon and energy source. There were no indications of growth under aerobic or autotrophic conditions. The isolate produced acetate, butyrate and ethanol as fermentation end products from glucose [22].

The species *Ruminiclostridium papyrosolvens*, according to Dassa *et al.* [23], is able to degrade cellulose. *C. butyricum*, *C. saccharolyticum*, *C. galactitolivorans* and *D. quercicolus* are bacterial species which produce hydrogen from cellulose sources. *C. butyricum* is a producer of hydrogen from molasses [24], while the major products of *D. quercicolus* grown in a medium with yeast extract, peptone and fructose were acetate, propionate, propanol, and hydrogen [25]. The strict anaerobe *C. galactitolivorans*, Gram-positive, non-spore-forming, rod-shaped bacterial strain was isolated from an anaerobic digestion reactor during a study of bacteria utilizing galactitol as a carbon source [26].

Both *Bacteroides* and *Clostridium* are anaerobic rod-shaped bacteria with indispensable role in cellulose degradation in living nature. *Bacteroides oleiciplenus* is known to produce extracellular enzymes which assist in the breakdown of complex plant polysaccharides such as cellulose and hemicellulose [27]. *C. butyricum* also has high capacity for cellulose degradation [28]; *Ruminiclostridium cellulolyticum* is anaerobic bacterium that depolymerizes cellulose and related plant cell wall polysaccharides *via* production of large extracellular multi-enzyme complexes termed cellulosomes [29].

Depending on the nature of the sample, distinct cellulose-degrading microbial communities could be found. By Wang *et al.* [30], a cellulolytic microbial community capable to degrade cotton and paper contains *Bacillus thermoamylovorans*, *Paenibacillus barengoltzii*, *Proteobacterium*, *Pseudoxanthomonas taiwanensis*, *Rhizobiaceae*,

Beta proteobacterium, *Petrobacter succinimandens*, *Tepidiphilus margaritifera*. By omics-based research other authors found a community with cellulose activity contacting *Clostridium sporogenes*, *Clostridium thermosuccinogenes*, *Clostridium thermocellum*, *Clostridium straminisolvens*, *Brevibacillus borstelensis*, *Cellulosilyticum lentocellum* [31]. Metagenome investigations of biodiversity in an anaerobic digester for biogas production by Sun *et al.* [32] showed that ubiquitous genera involved in the cellulose hydrolysis step include *Clostridium*, *Bacteroides*, *Succinivibrio*, *Prevotella* and *Ruminococcus*. *Fibrobacter*, formerly grouped to *Bacteroides*, as well as *Ruminococcus* and uncultured bacteria have also been suggested to play important roles in cellulose hydrolysis in the rumen; *Firmicutes* and *Bacteroidetes* were suggested to be important in a hydrolytic/acidogenic digester fed with dried hay and straw [32].

Illumina high-throughput sequencing was used to explore the microbial communities and functions in anaerobic digestion sludge (ADS) from two wastewater treatment plants based on a metagenomic view. Taxonomic analysis indicated that *Proteobacteria* (9.52–13.50 %), *Bacteroidetes* (7.18 %–10.65 %) and *Firmicutes* (7.53 %–9.46 %) were the most abundant phyla in the ADS [33].

A series of recent studies had indicated that enriched microbial communities, obtained from environmental samples through selective processes, can effectively contribute to lignocellulose degradation, combining ecological theory and enrichment principles to develop effective lignocellulose-degrading minimal active microbial consortia [34]. Using them with optimal substrate supply, appropriate mixing, maintaining pH at the optimum level and removing the resulting fermentation products can significantly improve the degree and rate of degradation of the substrates used.

CONCLUSIONS

Microbial degradation of cellulose containing substrates similar in composition to the hygiene materials used by space crews was realized by a selected genetically identified bacterial community. An effective anaerobic biodegradation process was accomplished applicable to laboratory biotechnology.

Acknowledgements: This work was supported by the Bulgarian National Science Fund (Grant: DNTS/Russia/ 01/4). Metagenomics investigations were conveyed with the support of Grant: DFNI-E02/13.

REFERENCES

1. G. Bornemann, K. Waßer, T. Tonat, R. Moeller, M. Bohmeier, J. Hauslage, *Life Sci. Space Res.*, **7**, 39 (2015).
2. C. Lasseur, J. Brunet, H. de Weever, M. Dixon, G. Dussap, F. Godia, N. Leys, M. Mergeay, D. van der Straeten. *Gravit. Space Biol.*, **23**, 3 (2010).
3. J. Seon,; C. Creuly, D. Duchez, A. Pons, C. G. Dussap, *Water Sci. Technol.*, **48**, 213 (2003).
4. H. Yan, C. Zhao, J. Zhang, R. Zhang, C. Xue, G. Liu, C. Chen, *AMB Express*, **7**, 27 (2017).
5. A. Ausiello, L. Micoli, M. Turco, G. Toscano, C. Florio, D. Pirozzi, *Int. J. Hydrogen Energy*, **42**, 30599 (2017).
6. R. López-Mondéjar, D. Zühlke, D. Becher, K. Riedel, P. Baldrian, *Sci. Rep.*, **6**, 25279 (2016).
7. L. Cortes-Tolalpa, J. F. Salles, J. D. van Elsas, *Frontiers in Microbiology*, **8**, 1628 (2017)
8. J. Walker, C. Granjou, *Futures*, **92**, 59 (2017).
9. J. Szostak-Kotowa, *International Biodeter. Biodegrad.*, **53**, 165 (2004).
10. L. R. Lynd, P. J. Weimer, W. H. van Zyl, *Microbiol. Molecular Biol. Rev. MMBR*, **66**(3), 506 (2002).
11. E.A. Bayer, R. Lamed, B. A. White, H. J. Flint. *Chem. Rec.*, **8**(6), 364 (2008).
12. A. Li, Y. Chu, X. Wang, L. Ren, J. Yu, X. Liu, J. Yan, L. Zhang, S. Wu, S. Li, *Biotechnol. Biofuels*, **6**(1), 3 (2013).
13. E. Korenblum, D. Jiménez, J. van Elsas, *Microbial Biotechnol.*, **9**(2), 224 (2016).
14. D. Updegraff, *Analyt. Biochem.*, **32**, 420 (1969).
15. A. Shikata, J. Sermsathanaswadi, P. Thianheng, S. Baramee, C. Tachaapaikoon, R. Waeonukul, P. Pason, K. Ratanakhanokchai, A. Kosugi, *Enzyme and Microbial Technol.*, **118**, 66 (2018).
16. Y. Chu, Y. Wei, X. Yuan, X. Shi, *Biores. Technol.*, **102**, 3805 (2011).
17. J. J. Lay, *Biotechnol. Bioeng.* **74**(4), 280 (2000).
18. F. Taguchi, J. D. Chang, S. Takiguchi, M. Morimoto, *J. Ferment. Bioeng.*, **73**, 244 (1992).
19. L. Zhang, J. Chung, Q. Jiang, R. Sun, J. Zhang, Y. Zhong, N. Ren, *RSC Adv.*, **7**, 40303 (2017).
20. K. Ahring, N. Murali, K. Srinivas, *Ferment Technol.*, **7**, 152 (2018).
21. E. G. Ozbayram, S. Kleinstaubler, M. Nikolausz, B. Ince, O. Ince, *Appl. Microbiol. Biotechnol.*, **102** (2), 1035 (2018).
22. Y. J. Lee, C. S. Romanek, J. Wiegel, *Int. J. Systematic and Evolutionary Microbiol.*, **57**(2), 311 (2007).
23. B. Dassa, S. Utturkar, R. A. Hurt, D. M. Klingeman, M. Keller, J. Xu, O. Zhivin, *Genome Announc.*, **3**(5), 15 (2015).
24. X. Wang, B. Jin, *J. Biosci. Bioeng.*, **107** (2), 138 (2009).
25. C. Strömpl, B. J. Tindall, H. Lünsdorf, T. Y. Wong, E. R. Moore, H. Hippe, *Int. J. Syst. Evol. Microbiol.* **50** (1), 101 (2000).
26. B. C. Kim, B. S. Jeon, S. Kim, H. Kim, Y. Um, B. I. Sang, *Int. J. Syst. Evol. Microbiol.*, **65** (12), 4902 (2015).
27. Y. Watanabe, F. Nagai, M. Morotomi, H. Sakon, R. Tanaka, *Int. J. Syst. Evol. Microbiol.*, **60**, 1864 (2010).
28. D. Szymanowska-Powałowska, D. Orczyk, K. Leja, *Braz. J. Microbiol.*, **9**, 45 (2014).
29. J. Ravachol, R. Borne, I. Meynial-Salles, P. Soucaille, S. Pagès, C. Tardif, H.P. Fierobe, *Biotechnol. Biofuels*, **13** (8), 114 (2015).
30. L. Wang, Z. Cui, Y. Gao, Y. Wang, R. Jing, *Biores. Technol.*, **102**, 9321 (2011).
31. C. Zhou, L. Xu, J. Song, R. Xing, S. Xu, D. Liu, H. Song, *Sci. Rep.*, **4**, 1 (2014).
32. L. Sun, P. B. Pope, V. G. Eijsink, A. Schnürer, *Microb. Biotechnol.*, **8**(5), 815 (2015).
33. Y. Yang, K. Yu, Y. Xia, F. Lau, D. Tang, W. Fung, H. Fang, T. Zhang, *Appl. Microbiol. Biotechnol.*, **98**, 5709 (2014).
34. P. Puentes-Téllez, J. Falcao Salles, *Microbial Ecol.*, **76**(2), 419 (2018).

Hydrodynamics of the flow of two immiscible liquids in a coiled tube of small diameter

S. Verma, V. Chauhan, S. Bharti, M. M. Mandal*

University School of Chemical Technology, Guru Gobind Singh Indraprastha University, N. Delhi, India

Received: December 15, 2019; Revised: April 04, 2020

The present experimental study was carried out to investigate the hydrodynamics of two immiscible liquids (kerosene and water) flowing with superficial velocity ranging from 0.04 m/s to 0.4 m/s in a coiled tube. The effects of different flow rates of the immiscible liquids, oil volume fraction and curvature ratio of coiled tube on the pressure drop across the tube were investigated. It was also intended to observe the effect of T and Y mixer on the pressure drop of the kerosene-water flow through the coiled tube. Various patterns of flow such as stratified, dispersed, as well as annular were observed during the experimental campaign. Knowledge of flow pattern characterization is valuable for design and optimization of liquid-liquid transportation processes. This study shows that the proper control of these process parameters will help in controlling the energy losses in different equipment used in industries.

Keywords: oil-water flow, coiled tube, flow patterns, superficial velocity, pressure drop

INTRODUCTION

Literature survey shows that there has been an emerging trend in research on the oil-water flows in pipes and newer, greener technologies are being investigated to tackle the concerns for depleting oil reserves. The oil refineries are focusing to explore and process more viscous and heavier oil as they have more reserves worldwide in comparison to conventional oil [1]. Flow of two immiscible liquids is considered to be a multiphase flow and finds its relevance in various macro as well micro scale applications. These applications include flow of oil water through pipes with large diameter during oil drilling and transportation [2, 3], coolants for microfluidic conduits [4], process industries for reaction, extraction, emulsification, separation, etc. [5, 6]. It has been reported that volume fraction of water and temperature have no significant effect on pressure losses for a water-dominated flow. The water-dominated flow may be preferred during the transportation of heavy crude oil with water. The results establish a theoretical basis for water-lubricated transport of extra heavy crude oil [2]. A new drilling technology, i.e. coiled tubing ultra-short radius radial drilling has already been functional since late twentieth century [3]. This drilling technology has increased well productivity and reduced operating cost significantly as compared to conventional sidetrack drilling. It is also suitable for the productivity enhancement of old oilfields. Recently, this type of liquid-liquid flow has found its significance in micro-systems such as microreactors

and micro-mixers which are designed and optimized for such systems. Currently, studies on fluid flow and heat transfer behavior of liquid-liquid two-phase flows are being carried out by various researchers to significantly improve the heat transfer rates in microchannels [4]. In all these applications, the behavior of the liquid-liquid immiscible flow was observed to be dissimilar to the flow of a single-phase liquid. These systems also demonstrate differences as compared to other type of multiphase flows such as gas-liquid flows and solid-liquid flows [7].

Knowledge on flows of immiscible liquids finds its use in tubular reactors employed in chemical, petrochemical, food, pharmaceutical and fine chemical industry where continuous processes take place. The diameters of these reactors could be in the range of millimetres. Many models have been proposed by different researchers which help in predicting the pressure gradient in straight pipes [8, 9]. Different models may be suited to predict pressure losses for different flow patterns. For example, a two-fluid model may be employed for stratified flow, whereas a homogeneous model may be used for dispersed flow [10]. A recent investigation on the flow pattern of a highly viscous oil-water flow at various temperatures in a straight tube has been reported [11]. It has been found that flow patterns of viscous oil-water flows are highly affected by temperature, oil fraction, as well as mixture velocity. It has also been reported that inversion points are intensely affected by mixture velocity.

* To whom all correspondence should be sent:
E-mail: monishamridha1@gmail.com

Pressure losses are found to vary from minimum to maximum at the inversion point [12].

Tubular reactors such as coiled tubes offer certain benefits in contrast to continuously stirred tank reactors. Recently, a coiled flow inverter (CFI) reactor was used for transesterification of fatty acids at various flow rates and residence times [13]. CFI also displayed twelve times faster biodiesel production than the conventional batch reactors at the given conditions. This was because of mixing enhancement which affected the contact between the liquid phases in the liquid-liquid reaction. The coiled reactors exhibit better heat transfer, mass transfer as well as control owing to improved compact size [14,15]. These types of reactors also reduce the possibility of hazards because of better temperature control and offer higher yields [16]. A good design of a reactor involves a considerable knowledge of the liquid-liquid flows through the pipes. A better understanding of the flow pattern is one of the parameters needed to know the hydrodynamics of the reactor. This further helps in measuring the interfacial area of contact between the liquids [17].

The motivation for this study was aroused when the literature review showed that the majority of the researches on liquid-liquid flows were confined to flows through straight tube and capillaries [18-22]. Studies on flow patterns have rarely been reported for coiled tubes [16, 23]. Moreover, it was found that different passive mixers such as T type and Y type are used to improve mixing of immiscible liquids in channels. These have simple system design with a reasonable mixing efficiency [24]. The performances such as mixing efficiency and pressure losses of a microchannel depend on the type of flow patterns which are developed in the microchannel. These flow patterns give an idea about the specific interfacial area available for mass transfer. The flow pattern generated at a microfluidic junction depends on the geometry of the microfluidic mixer or junction [25]. Consequently, the knowledge of the flow pattern produced in a specific mixer is important while designing any process. There are limited data reported in the literature on mixing performance and pressure loss data for these types of mixers with small diameter [24-27]. These gaps in literature motivated us to investigate the effect of two different mixers on the overall pressure losses in the coiled tube system. Therefore, an experimental study was carried out to investigate the liquid-liquid flows through coiled tubes with a small diameter at lab scale. The effects of velocity of oil and water, oil volume fraction and type of mixer (T and Y type) on the pressure drop for an oil-water flow in a coiled tube of diameter 7 mm were experimentally studied.

Knowledge of pressure drop will help in evaluating the energy losses through these types of systems. It is important to identify the flow pattern as it aids in identifying the multiphase flow behaviour and designing of process equipment. Therefore, the flow patterns observed at different velocities of oil and water were reported here.

MATERIALS AND METHODS

Fig. 1 shows the experimental set-up in which the present work was carried out.

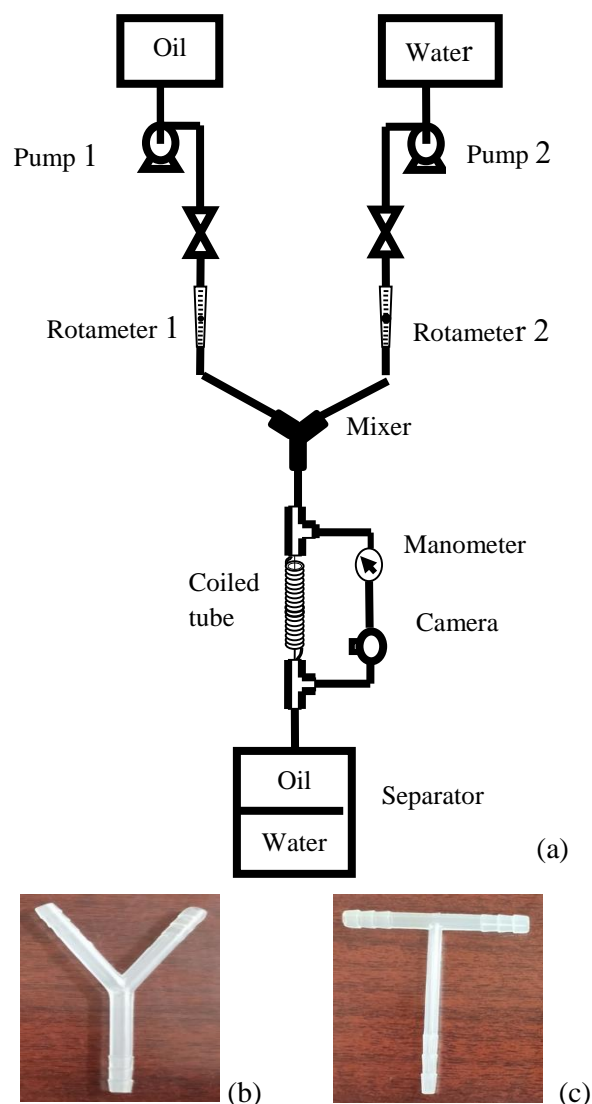


Fig. 1. (a) Experimental set-up, (b) Y type mixer, (c) T type mixer

The facility consists of two storage tanks which were used for containing oil (kerosene) and water, respectively. The experiments were conducted at an ambient temperature of 27–28 °C. The properties of kerosene and water are shown in Table 1. The two liquids were pumped with two pumps whose maximum flow rate was 1.5 m/s.

Table 1. Properties of liquids

Fluids	Kerosene	Water
Density, kg/m ³	800	996
Dynamic viscosity, Pa-s	0.00164	8.9×10 ⁻⁴
Interfacial tensions @ 20 °C, mN/m	Water /kerosene	23

The kerosene and water flow rates were measured by independent rotameters, with a measuring range of 0-2 lpm, corresponding to a superficial velocity range of 0-0.9 m/s, and uncertainty, obtained via calibration, of ±1% of full scale value. Acrylic rotameters were used to measure water and kerosene flow rates. The rotameters were factory-calibrated for given liquids under given ambient temperature and pressure conditions. These devices were re-calibrated to ensure that accurate measurements are taken. A T-type or Y-type mixing section was connected to mix the kerosene and water. The pictures of the mixers are shown in Fig.1 (b) and (c). The liquids then entered the test section (coiled tube). The test section was a transparent PVC tube with a diameter of 0.007 m and length of 89 cm which was tightly coiled over different cylinders for obtaining different curvature ratios (ratio of diameter of coiling to diameter of tube, $\lambda=dc/dt$). The coil curvature ratios were 5, 7 and 28. The experiments were carried out with superficial velocity of the liquids ranging from 0.04 m/s to 0.4 m/s. Investigations on various water and kerosene volume fractions were carried out by adjusting their flow rates. A U-tube manometer containing mercury was connected just near the inlet and outlet of the coiled tube to determine the pressure drop of the immiscible liquids flowing in the coiled tube. In the present work, total pressure drop was calculated from eq. (1):

$$(\Delta P_T) = \rho g (\Delta h) \quad (1)$$

Here ρ is the difference in density of mercury in manometer and density of oil-water mixture. Δh is the difference in height of mercury in manometer observed during the experimentation and g is the acceleration due to gravity.

The total two-phase flow pressure losses are considered to be the sum of pressure losses due to friction (ΔP_{fric}), pressure losses due to acceleration ($\Delta P_{acceleration}$) and hydrostatic pressure loss:

$$(\Delta P_{static}). \Delta P_T = \Delta P_{fric} + \Delta P_{acceleration} + \Delta P_{static} \quad (2)$$

Acceleration pressure losses ($\Delta P_{acceleration}$) may be considered to be negligible for isothermal flows in constant-diameter tubes. In eq. (2), the hydrostatic pressure loss is:

$$(\Delta P_{static}) = \rho_{mix} g \sin \phi l \quad (3)$$

where l is the difference in elevation of inlet and outlet of the coiled tube and ϕ is the angle of flow. Therefore, the pressure drop due to frictional losses, (ΔP_{fric}), can be estimated from eq. (4):

$$(\Delta P_{fric}) = (\Delta P_T) - (\Delta P_{static}) \quad (4)$$

Moreover, the friction factor, f , can be calculated from eq. (5):

$$(\Delta P_{fric}) = 2 \frac{f U_{mix}^2 \rho_{mix} L}{d} \quad (5)$$

Here L is the length of coiled tube and d is the internal tube diameter. The properties of the oil-water mixture were calculated based on their individual properties and volume fractions of the immiscible liquids [10]. Density of mixture, ρ_{mix} , was calculated by equation (6):

$$\rho_{mix} = \rho_o \phi_o + (1 - \phi_o) \rho_w \quad (6)$$

where the volume fraction of oil, $\phi_o = \frac{\text{inlet oil flowrate}}{\text{total liquid flowrate}}$, ρ_o is density of oil, ρ_w is density of water. The mixture velocity, U_{mix} , is the sum of both phases' superficial velocities:

$$U_{mix} = U_{sw} + U_{so}, \quad (7)$$

where U_{sw} and U_{so} correspond to water and oil superficial velocities, respectively. Friction factor, f , was calculated from eq. (5) and then plotted against Reynolds number, Re . Re can be calculated from equation (8):

$$Re = \frac{d \rho_{mix} U_{mix}}{\mu_{mix}} \quad (8)$$

Here the viscosity of the mixture, μ_{mix} was calculated based on the volume fraction of oil, ϕ_o , viscosity of oil, μ_o , and viscosity of water, μ_w , as given in eq. (9):

$$\mu_{mix} = \mu_o \phi_o + (1 - \phi_o) \mu_w \quad (9)$$

Each run continued for some time to achieve a steady-state flow before acquiring and recording the experimental data. The oil-water mixture was subsequently passed to a tank for separation of the oil and water. The pictures of the various patterns of flow at different velocities were taken using a digital camera Nikon 5300D. Concentrated dye soluble in the oil or water phase was added into the feed tanks for better visualization of flow patterns. The

selection criterion of dye was its solubility in one phase only. Fluorescein Sodium (green in color) was chosen as the dye for water and Biebrich Scarlett R (red in color) was chosen for the oil phase.

RESULTS AND DISCUSSION

In the present study, oil and water superficial velocities were varied from 0.04 to 0.4 m/s. Different patterns of flow were observed at varying velocities.

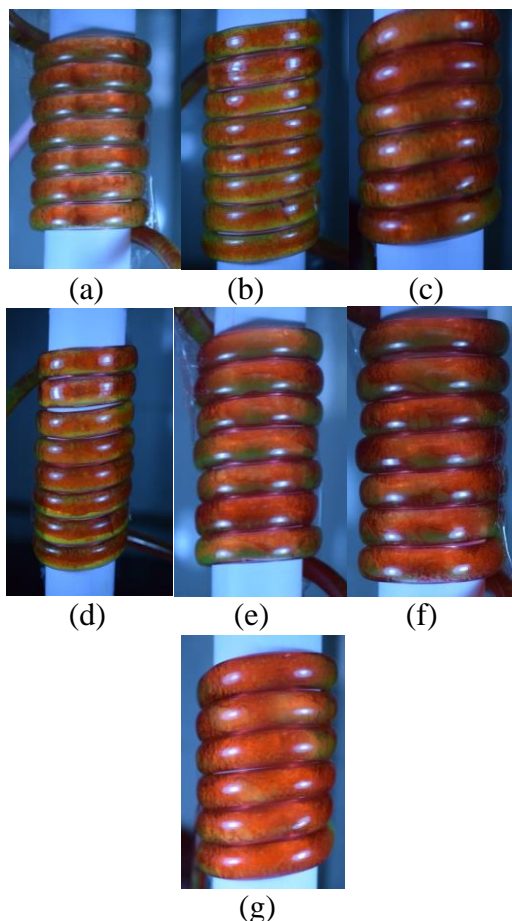


Fig. 2. Different flow patterns observed in the present study (a) Oil dispersed in water over a water layer, Do/w &w, $V_{os} = 0.04$ m/s, $V_{ws} = 0.39$ m/s; (b) annular flow, A, $V_{os} = 0.13$ m/s, $V_{ws} = 0.39$ m/s; (c) Oil in water emulsion, Eo/w , $V_{os} = 0.17$ m/s, $V_{ws} = 0.30$ m/s; (d) stratified flow, ST, $V_{os} = 0.21$ m/s, $V_{ws} = 0.30$ m/s; (e) Wavy stratified flow, WST, $V_{os} = 0.26$ m/s, $V_{ws} = 0.17$ m/s; (f) Water dispersed in oil under an oil layer, Dw/o &o, $V_{os} = 0.30$ m/s, $V_{ws} = 0.12$ m/s; (g) water in oil emulsion, Ew/o , $V_{os} = 0.30$ m/s, $V_{ws} = 0.04$ m/s.

Following patterns were noted:

- (a) Oil dispersed flow (Do/w &w): Tiny oil droplets were dispersed in water over water layer;
- (b) Annular flow (A): oil drops were dispersed in core and water in the annulus region of the coiled tube;

(c) Emulsion flow (Eo/w): oil drops were distributed in the continuous water phase;

(d) Stratified flow (ST): oil and water flow in separate layers;

(e) Wavy stratified flow (WST): wavy interface is observed between separate layers of oil and water flow;

(f) Water dispersed flow (Dw/o &o): Water droplets are dispersed in oil under oil layer;

(g) Emulsion flow (Ew/o): water drops are distributed in the continuous oil phase.

Fig. 2 shows the pictures of different flow patterns of oil in the coiled tube with a diameter of 0.007 m. The figure is arranged sequentially with increase in velocity of oil and decrease in velocity of water. Fig. 2 (a) shows the flow pattern when the velocity of oil is least, i.e. 0.04 m/s while the water velocity is maximum, i.e. 0.39 m/s. It can be observed that oil bubbles are dispersed in water at the upper section of coiled tube. When the velocity of oil increases to 0.13 m/s, the flow pattern changes to annular flow. Fig. 2(b) depicts that the oil is dispersed at the core while water is at the annulus of the tube. Fig. 2(c), shows that as superficial velocity of oil is increased to 0.17 m/s while the water velocity is decreased to 0.3 m/s, water is in continuous phase and oil bubbles are distributed throughout the tube cross-section. Stratified flow is viewed at oil velocity of 0.21 m/s and velocity of water of 0.3 m/s. This is illustrated in Fig. 2 (d). The first five turns of the coiled tube have a stratified flow with mixed interface. The last three turns of the coil tube have a more distinct interface between the immiscible liquids. The interface between the two immiscible liquids is clear cut, smooth and displays two noticeable separate regions of different liquids. Fig. 2 (e) shows that the increase in superficial velocity of oil to 0.26 m/s and decrease in velocity of water to 0.17 m/s lead to a wavy stratified flow. The additional enhancement in velocity of oil (0.30 m/s) leads to a change in flow pattern in which water is dispersed in oil under the oil layer. This is revealed in Fig. 2 (f). In this case, the continuous phase is oil. When the water velocity is decreased to 0.04 m/s, water bubbles are found to be dispersed in the oil as shown in Fig. 2 (g). Hence, it is observed that changes in velocity of oil and water affected the pattern of flow. These flow patterns were plotted for varying water and oil velocities and are illustrated in Fig. 3. Figures 3 (a) and 3(b) show the flow pattern maps for T type mixer and Y type mixer, respectively. The figure exemplifies the flow regime of the oil-water flow through a coiled tube with curvature ratio of 5.

Fig. 3(a) illustrates that in the T type mixer, flow pattern Do/w (oil dispersed in water) was observed for the mixture where water was at a higher velocity of 0.4 m/s and oil was at a lower velocity of 0.04 m/s. Gradually, annular flows were observed when the oil velocity was increased to around 0.1 m/s and water velocity was still higher at 0.35 m/s. Stratified flow and wavy stratified flows were observed when the oil and water velocities were in similar ranges. Emulsion of water in oil was observed when the

water velocity was low (0.04 m/s) as compared to oil. Fig. 3 (b) shows the flow pattern map for the Y type mixer. It can be seen from Fig. 3 (b) that some of the flow patterns such as annular, stratified, as well as emulsion of water in oil were not detected for the present experimental conditions in the Y type mixer. At low oil velocity (0.17 m/s) and higher water velocity, dispersion of oil over water layer was observed.

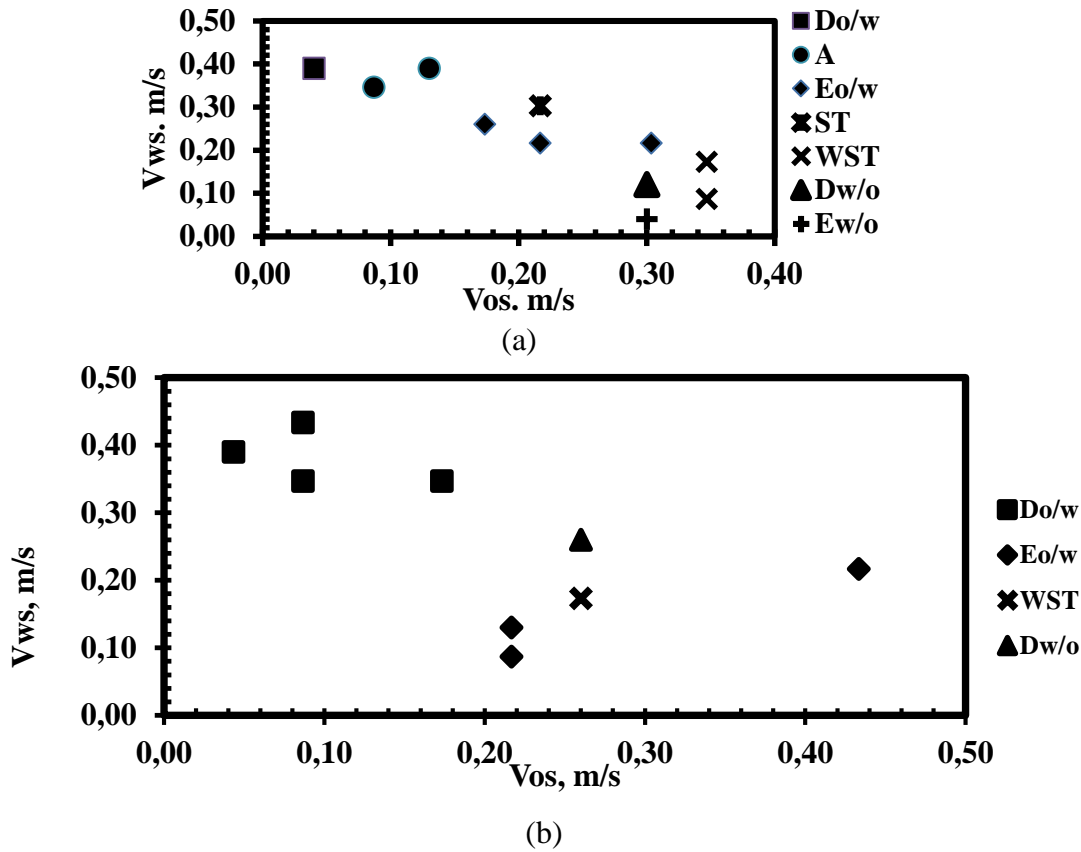


Fig. 3. Flow regime of the oil water flow through a coiled tube with $d_c=0.007$ mm, $\lambda=5$
 (a) T type mixer, (b) Y type mixer

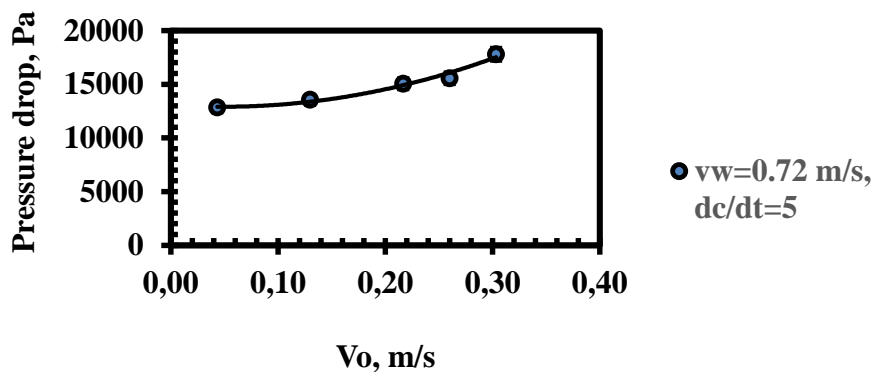


Fig. 4. Pressure drop vs. velocity of oil through the coiled tube of diameter 0.007 m, $\lambda=5$ at constant water flow rate of 0.72 m/s

Emulsion of oil in water was observed when the oil velocity was increased to 0.21 m/s. Wavy stratified flow pattern was found when the oil velocity was further increased to 0.26 m/s. Dispersion of water under the oil layer was found when velocities of both water and oil were 0.26 m/s.

Fig. 4 shows the values of pressure drop at various oil velocities. The velocity of oil was varied within the range of 0.04 to 0.3 m/s and water velocity was kept constant at 0.72 m/s. Pressure drop was

found to be increasing with increase in oil velocity. When the oil velocity was increased from 0.04 to 0.3 m/s, there was nearly 25 % enhancement in pressure drop. This is due to the enhancement of inertial forces with increasing flow rates. Parity plots were plotted for pressure drop values measured from the present experiments against values predicted for single-phase flows in a coiled tube from correlations of Mishra and Gupta (1979) [28] and are shown in Fig. 5.

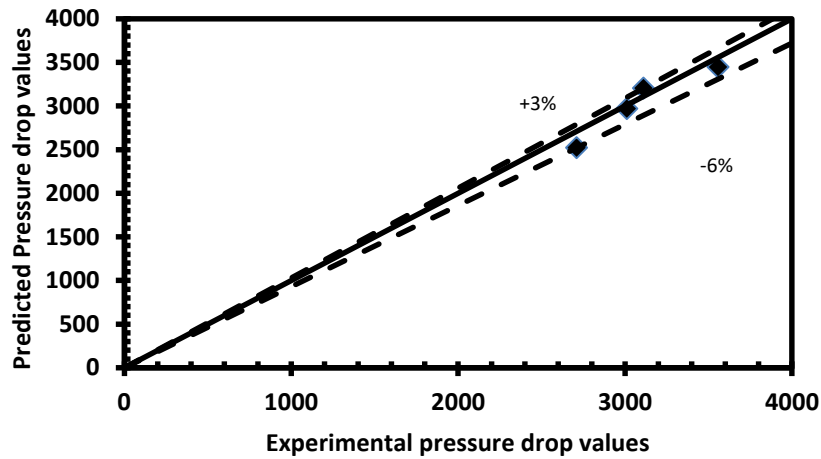


Fig. 5. Parity plot of experimental pressure drop values vs. predicted pressure drop values

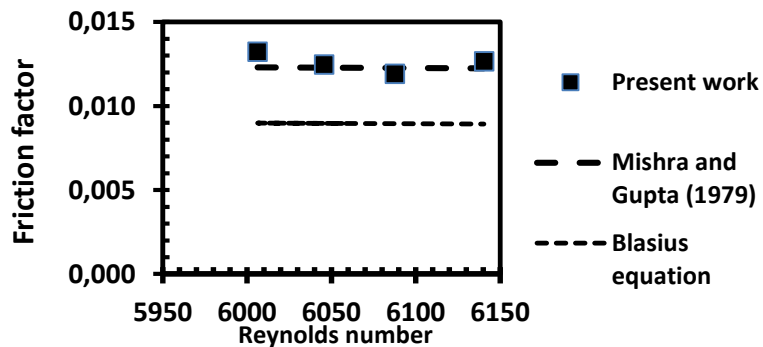


Fig. 6. Comparison of friction factor vs. Reynolds number with previous literature

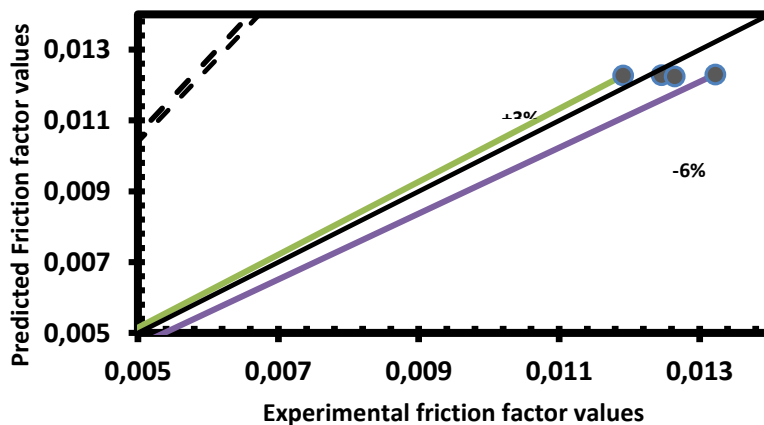


Fig. 7. Parity plot of experimental friction factor values vs. predicted friction factor values

The friction factor values were calculated for different Reynolds numbers and are reported in Fig. 6. The present data were compared with existing correlations previously reported for single-phase flows in a coiled tube, as well as in a straight tube by Mishra and Gupta (1979) [28] and by Blasius equation [29], respectively. It was found that under present flow conditions, the friction factor decreased with the increase in Reynolds number. Friction factor calculated from the present work was found to be by 24 to 32 % higher than that of Blasius equation proposed for a straight tube. Present experimental values were found to be in agreement with values predicted by correlation of Mishra and Gupta (1979) [28]. Fig. 7 shows the parity plot between friction factor values calculated from present experiments and values predicted from correlations of Mishra and Gupta (1979). Present experimental values are in

agreement with predicted values and are within ± 6 % error.

Fig. 8 shows the effect of oil fraction on pressure drop across the coiled tube with a curvature ratio $dc/dt=7$. Pressure drop increased with the increase in both oil fraction and velocity of oil-water. This was because of the enhancement of overall viscous forces and inertial forces. The percentage increase in pressure drop for the different velocities was 10 % at 0.3 oil fraction. However, this increment was 20 % for 0.5 oil fraction. The effect of curvature ratio on pressure drop at different oil fractions can be seen in Fig. 9. The curvature ratios were 7 and 28. The difference in pressure drop due to varying curvature at 0.41 oil fraction for 0.43 m/s was nearly 9 %. However, the increment increased to 25 % for $v=0.52$ m/s at oil fraction of 0.75.

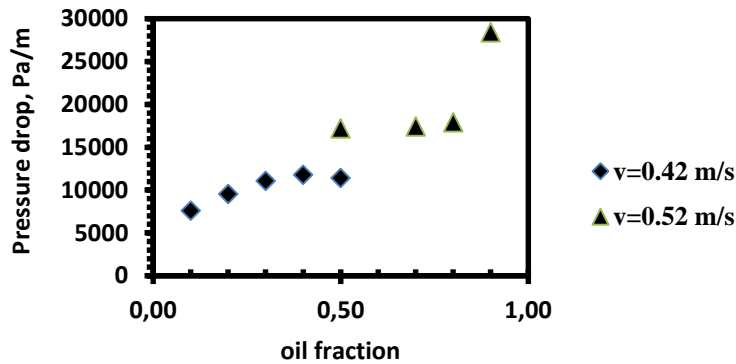


Fig. 8. Variation of pressure drop and oil fraction for different mixture velocities for $d_t=0.007$ mm, $\lambda=7$

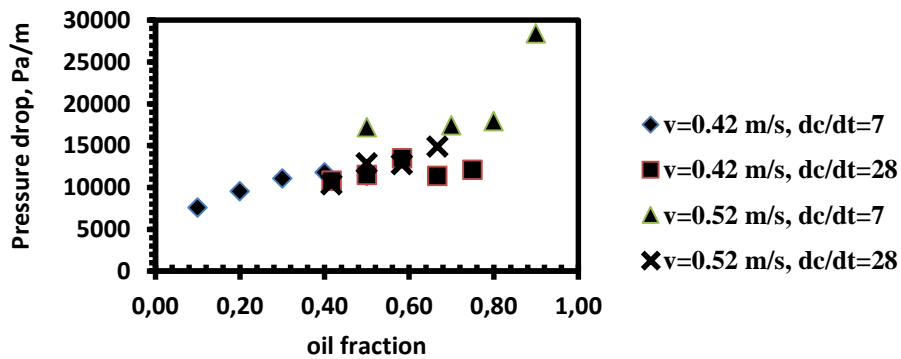


Fig. 9. Pressure drop vs. oil fraction for different curvature ratios

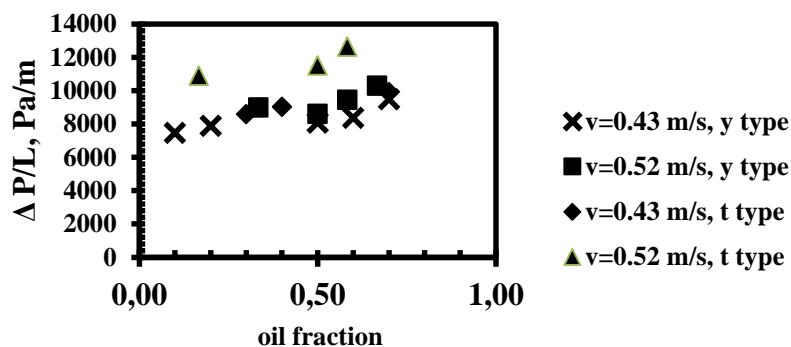


Fig. 10. Pressure drop vs. oil fraction for T-type mixer and Y- type mixer

This shows that the effect of curvature ratio on pressure drop was prominent at higher velocity. This was because of stronger development of secondary forces in a coiled tube at higher velocity.

Literature shows that the type of mixers has impact on the flow patterns of liquids flowing in micro tubes. The effect of two types of mixers (T type and Y type) on pressure drop was investigated and displayed in Fig. 10. In the present work, no significant effect was observed for lower velocity. However, pressure drop was found to increase for higher velocity ($v=0.52$ m/s) when the liquids flow through a T type mixer. Pressure drop value was by nearly 26 % higher in T type as compared to Y type mixer.

CONCLUSIONS

The present experimental study was carried out to gain insight on the hydrodynamics of oil-water flows through a coiled tube of diameter 7 mm. The study helped in identifying the various flow patterns of two immiscible liquids, i.e. kerosene and water. Various patterns of flow such as stratified, dispersed and annular flows were observed at different superficial velocities of water and oil. Flow pattern maps were plotted based on varying water and oil superficial velocities and reported for T type and Y type mixers. Effect of parameters such as velocity of oil, curvature ratio of coiled tube and oil fraction on pressure drop was observed. It was found that there was nearly a 25 % increment in pressure drop as the total oil–water flow velocity was increased from 0.76 m/s to 1.1 m/s. The influence of curvature of coiled tube on pressure drop was prominent at higher velocities. There was a pressure drop increment of 25 % for oil fraction of 0.75 at velocity 0.52 m/s. Increase in oil fraction lead to an increase in pressure drop due to enhancement of viscous forces. The significance of T or Y type mixer on pressure drop was observed for higher velocity. The T type mixer produced 26 % higher pressure drop for the oil-water flow with $v=0.52$ m/s in the coiled tube. This

suggests that Y type mixers may be preferred to minimize energy losses for oil-water flows. Present study will be helpful in designing energy-efficient reactors and heat exchangers where immiscible liquids are used.

Acknowledgement: The authors would like to acknowledge Guru Gobind Singh Indraprastha University for the financial, as well as administrative support to carry out this research work.

REFERENCES

- H. Alboudwarej, J. Felix, R. Badry, *Oilfield Review*, **18** (2), 34 (2006).
- X. Luo, G. Lü, W. Zhang, L. He, Y. Lü, *Exp. Therm. Fluid. Sci.*, **82**, 174 (2017).
- M. Dongjun, L. Gensheng, H. N. Mingjuan, L. Jingbin, *Petrol. Explor. Develop.*, **39**, 528 (2012).
- A. Abdollahi, R. N. Sharma, A. Vatani, *Int. Commun. Heat Mass*, **84**, 66 (2017).
- R. Kaur, M. Ramakrishna, K.D.P. Nigam, *Rev. Chem*, **23**, 247 (2007).
- R. Kaur, M. Ramakrishna, K.D.P. Nigam, *Int. J. Chem. React. Eng.*, **5**, A27 (2007).
- T. K. Mandal, D. P. Chakrabarti, G. Das, *Chem. Eng. Res. Des.*, **85**(8), 1123 (2007).
- P. Angeli, G. F. Hewitt, *Int. J. Multiphase* **24**, 1183 (1999).
- N. Brauner, *Int. J. Multiphase*, **27**, 885 (2001).
- M. Hadziabdic, R. V. A. Oliemans, *Int. J. Multiphase*, **33**, 1365, (2007).
- J. Jing, J. Sun, J. Tan, M. Huang, Q. Liang, T. Xue, *Exp. Therm. Fluid Sci.*, **72**, 88 (2016).
- A. Mukhaimer, A. Al-Sarkhi, M. El Nakla, W.H. Ahmed, L. Al-Hadhrami, *Int. J. Multiph. Flow*, **100** (73), 90 (2015).
- E. L. Guajardo, E. O. Nadal, E. M. Castellanos, K. D. P. Nigam, *Chem. Eng. Sci.*, **169**, 179 (2017).
- M.M. Mandal, C. Serra, Y. Hoarau, K. D. P. Nigam, *Microfluid Nanofluid*, **10**, 415 (2011).
- E. A. López-Guajardo, G. M. Garza-Cantú, A. Marques-Camarena, E. Ortiz-Nadal, K. D. P. Nigam, A. Montesinos-Castellanos, *Ind. Eng. Chem. Res.*, **58**, 1075 (2019).
- M.M. Mandal, P. Aggarwal, K. D. P. Nigam, *Ind. Eng. Chem. Res.*, **50**(23), 13230 (2011).

17. M. Darekar, K. K. Singh, S. Mukhopadhyay, K. T. Shenoy, *Eng. Chem. Res.*, **56** (42), 12215 (2017).
18. T. Ganat, S. Ridha, M. Hairir, J. Arisa, R. Gholami, *J. Petrol. Explor. Prod. Technol.*, **9**, 2911 (2019).
19. M. Du, N .D. Jin, Z. K. Gao, Z. Y. Wang, L. S. Zhai, *Int. J. Multiph. Flow*, **41**, 91 (2012).
20. H. Hu, J. Jing, J. Tan, G. H. Yeoh, *Exp. Comput. Multiph. Flow*, **2**, 99 (2020).
21. T. Al-Wahaibi, Y. Al-Wahaibi, A. Al-Ajmi, R. Al-Hajri, N. Yusuf, A. S. Olawale, I. A. Mohammed, *J. Petrol. Sci. Eng.*, **122**, 266 (2014).
22. L. Edwards, D. Jebourdsingh, D. Dhanpat, D. P. Chakrabarti, *Cogent Eng.*, **5**, 1494494 (2018).
23. A. Dey, M.M. Mandal, *Adv. Sci. Eng. Med.*, **12**, 173 (2020).
24. S.S. Hsieh, J.W. Lin, J.H. Chen, *Int. J. Heat Fluid Fl.*, **44**, 130 (2013).
25. S. Sarkar, K. K. Singh, V. Shankar, K. T. Shenoy, *Chem. Eng. Process*, **85**, 227 (2014).
26. S. M. Tu, S. Torii, Y. C. Shi, *J. Multiphysics*, **5**, 215 (2011).
27. L. Xin, W. Shaoping, *CJA*, **26**(4), 1080 (2013).
28. P. Mishra, S. N. Gupta, *Ind. Eng. Chem. Process Des. Dev.*, **18**, 130 (1979).
29. W. L. McCabe, J. C. Smith, P. Harriott, Unit operations of chemical engineering (5th edn.). New York, London, McGraw-Hill, 1993.

Application of CFD-DEM method in modeling of wood combustion in a fixed bed

J. K. Tanui¹, P. N. Kioni¹, T. Mirre², M. Nowitzki², D. A. Todorova^{3*}

¹Department of Mechanical Engineering, Dedan Kimathi University of Technology, P.O. Box 657-10100, Nyeri, Kenya

²Department of Engineering and Natural Sciences, Technical University of Applied Science, Wildau, Hochschulring 1, 15745 Wildau, Germany

³Department of Pulp, Paper and Graphic art, University of Chemical Technology and Metallurgy, 8 Kl. Ohridski Blvd., 1756 Sofia, Bulgaria

Received: September 12, 2019; Accepted: May 07, 2020

In this study, a numerical simulation of wood burning in a biomass stove is presented. The main aim was to test the suitability of Computational Fluid Dynamics – Discrete Element Method (CFD-DEM) approach in predicting temperature distribution and species generation in a fixed bed applicable in small-scale biomass stoves. A commercial software code STAR CCM+ was used to simulate combustion of eucalyptus wood under air-fuel condition. Wood burning in a fixed bed was simulated using Lagrange-Euler method, where gas-phase was calculated using computational fluid dynamics while solid-phase was tracked in Lagrange approach. Modeling was validated by comparison with measured data. A good agreement between model and measured data was achieved. Therefore, the CFD-DEM method is a good tool in design and optimization of new combustion equipment.

Keywords: CFD-DEM, Wood combustion, Fixed bed, Temperature distribution

INTRODUCTION

Most people in the world still use small-scale biomass stoves for domestic energy requirements. Biomass combustion significantly contributes to air pollution in terms of particulate matter (PM) or soot and toxic gases [1]. It is a well-known fact that exposure to PM and black carbon from any source causes respiratory and cardiovascular diseases [2]. In addition, some of the pollutants emitted by biomass combustion, for instance, PAH, aldehydes and benzene, are carcinogenic and mutagenic [1]. Therefore, there is need for proper design of biomass burners which have optimum combustion parameters; high efficiency and low emissions.

Biomass conversion to energy is done using different combustion chambers operated under wide conditions. A typical example is a fixed bed combustion chamber. Biomass combustion in a fixed bed is affected by fuel type and composition, air flow rate, amount of moisture in the fuel, fuel shape and size [3, 4]. These factors also affect emission characteristics of the fixed bed reactor. Careful consideration of these factors should be taken into account when designing a biomass burner.

CFD is an important tool in designing and optimization of new burner equipment, as well as troubleshooting old devices. It helps in understanding combustion processes which take place in a burner. CFD simulations give an approximate of these physical and chemical processes. However, they do not give a detailed

description of all the relevant combustion phenomena. Modeling of biomass thermal conversion in a packed bed have been differently approached. Using one-dimensional models, different researchers [5–7] have studied the propagation of ignition front and the reactions in a fixed bed of biomass fuels. These models do not consider individual particles, hence they do not accurately predict thermal conversion of fixed bed and require an experimentally determined empirical correlation. Another approach is the single particle model, where conversion of packed bed is constituted by summation of individual particle conversion. Through this approach the effects of initial relative velocity, free stream oxygen concentration, particle size, pre-exponential factor and particle entrainment on the conversion of a single particle have been investigated [8–10]. Recently, three-dimensional models for simulating combustion in a fixed bed have been developed [11–13]. Collazo *et al.* [11] simulated a fixed bed reaction using a 3D model that did not consider bed shrinkage. A 3D model that considers bed movement was developed by Mahmoudi *et al.* [14]. In this model, gas phase was modeled as three-dimensional, while solid phase was modeled as one-dimensional. Although an extensive CFD research has been done on fixed bed combustion, a few researchers use detailed models to predict both bed and freeboard biomass combustion in a fixed bed.

* To whom all correspondence should be sent:

E-mail: todorova.dimitrina@uctm.edu

The main aim of this study was to test the suitability of the CFD-DEM approach in predicting temperature distribution and species generation in a fixed bed. Experimental tests were carried out in a laboratory-scale fixed bed. Temperature distribution in the bed was measured and compared to CFD-DEM results.

EXPERIMENTAL

A schematic diagram and a photo of the experimental set-up used in this work are shown in Fig. 1. A detailed description of the set-up has been given in our previous paper [15]. It is a cylindrical chamber with an internal diameter of 40 mm and a height of 200 mm. Air inlet port is located at the bottom and grate is located 40 mm from it. Flue gas

outlet is located at the top of the chamber. Wood particles were fed up to a height of 6 cm.

Proximate and ultimate analysis for the wood samples investigated in this study are presented in Table 1 and physical properties - in Table 2.

Numerical simulations of combustion of wood in a fixed bed were carried out using a commercial software CD-Adapco (STAR CCM+ version 11.04) [16]. Wood burning in a fixed bed was simulated using Lagrange-Euler method, where gas-phase was calculated using computational fluid dynamics (Euler phase) while solid-phase was tracked in Lagrange phase (discrete element method). A detailed description of the governing equations is given in Ref. [16].

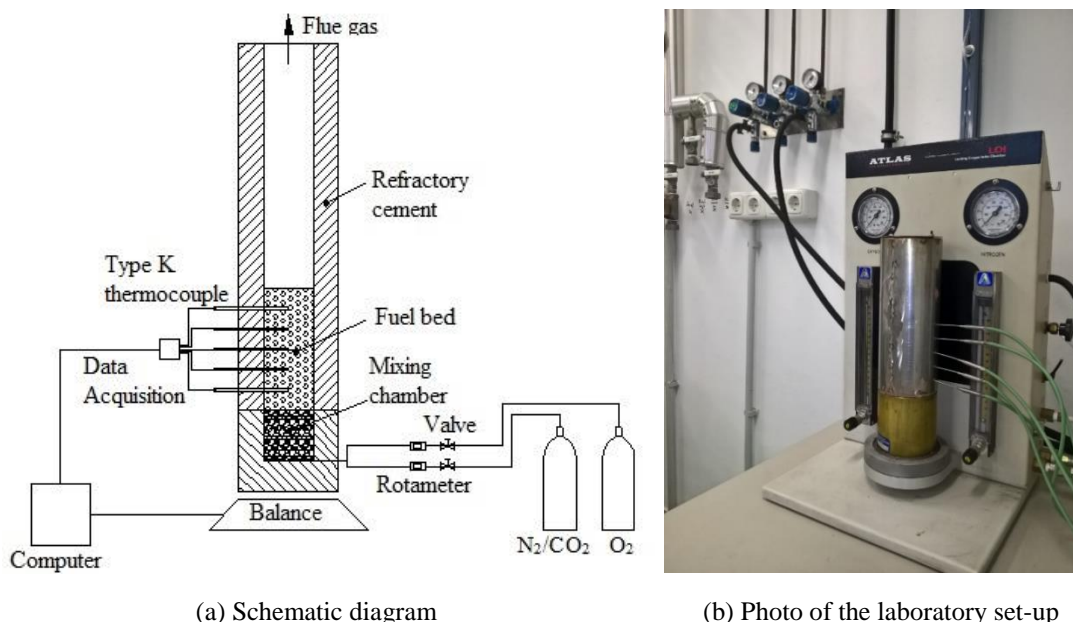


Figure 1. Experimental set-up.

Table 1. Proximate and ultimate analysis of fuel sample.

Proximate Analysis	(wt %)	Standards
Moisture	10.3	CEN-TS 14774-2:2009
Volatile matter (wt% dry basis)	84.9	CEN-TS 15148:2009
Fixed carbon (wt% dry basis) - by difference	14.9	-
Ash (wt% dry basis)	0.2	CEN-TS 14775:2009
Ultimate Analysis	(wt % dry basis)	Standards
C	50.87	CEN-TS 15104:2011
H	5.73	CEN-TS 15104:2011
N	0.3	CEN-TS 15104:2011
O (by difference)	43.1	-
Gross calorific value (MJ/kg)	19.3	CEN-TS 14918:2009

Table 2. Physical properties of wood

Particle diameter, d_p (m)	0.005
Eucalyptus wood	
Density, ρ (kg/m ³)	1220
Porosity, θ	0.64
Specific heat, c_p (J/kgK)	$1500 + T_s$
Conductivity, λ_s (W/mK)	0.2
Char	
Density, ρ (kg/m ³)	250
Porosity, θ	0.85
Specific heat, c_p (J/kgK)	$420 + 2.09T_s - 6.85 \times 10^{-4} T_s^2$
Conductivity, λ_s (W/mK)	0.1

The geometrical configuration of the combustion chamber shown in Fig. 1 was meshed into a highly-refined unstructured grid. The computational mesh consisted of approximately 200,000 cells.

Chemical kinetics of wood conversion in the bed was simulated using different sub-models, which consisted of drying model, pyrolysis model, homogeneous reaction model and char oxidation and gasification model. Kinetic data of these sub-models are given in Table 3.

The cold air at a temperature of 295 K enters the burner through the bottom boundary modeled as mass flow boundary, and hot combustion products exit the domain through the top boundary modeled as pressure outlet boundary. The air flow rate at the inlet was 0.1 kg/m²s while the mass fractions concentration of O₂ and N₂ were specified using the standard air composition. A stationary wall with no-slip conditions was considered; the tangential velocity at the wall was explicitly set to zero. Heat transfer by radiation and convection at the wall were considered. Emissivity of the surface and coefficient of heat transfer were assumed to be 0.8 and 10 W/m² K, respectively.

RESULTS AND DISCUSSION

The model results were validated by comparing predicted and measured temperature at corresponding positions in the fuel bed. Shown in Fig. 2 is the temperature history at 5 cm from bed bottom. A good agreement between predicted and measured temperature values is achieved. The graph shows that the temperature profile has two peaks; the first peak is about 1200 K while the second peak is about 1400 K. As the flame front passes the position where measurement is done, temperature rises rapidly up to the first peak. Then it gradually

decreases to about 900 K where it starts to rise again. This phase of combustion is characterized by both exothermic and endothermic processes. Exothermic reactions of the volatiles increase the temperature while drying and pyrolysis, which are endothermic processes, decrease the temperature. The second part of the graph, where temperature rises, signifies the end of endothermic processes. The volatiles transported from the lower part of the bed burn in this phase. The last regime, where temperature decreases, is characterized by char gasification and oxidation. Whereas char oxidation increases the temperature, char gasification with H₂O and CO₂ decrease the temperature. Overall decrease in temperature indicates that gasification is the dominant process in this regime.

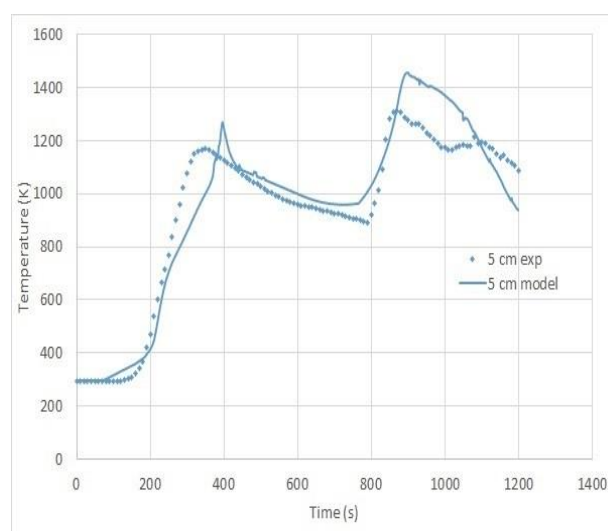


Figure 2. Measured and predicted temperature profile at 5 cm from fuel bottom.

Presented in Fig. 3 are the gas-phase and particle surface temperatures at different times. The figures clearly reveal the movement of reaction front from top to bottom as combustion proceeds. Temperature distribution at the same cross-section is non-uniform. Some particles have higher temperature than others located within the same height. Particles close to the wall have higher temperatures compared to corresponding particles close to the centre. This is because walls were modeled in such a way that small amount of heat is lost.

Initially, the bed is ignited at the top. During ignition, a lot of heat is absorbed by the particles. This heat is used for drying and pyrolysis which occur simultaneously, and the bed temperature does not significantly increase, as illustrated in Figs. 3(a) and (b). Once pyrolysis products are released, they react with O₂ and release more heat which increases the temperature, as shown in Fig. 3(c).

Table 3. Biomass kinetic model

Drying		Rate expression	Source
R(1)	Wet wood \rightarrow Dry wood + H ₂ O (g)	$R_{dry} = Y_{mp,b,wet} 1.6 \times 10^{27} \exp(-25000/T_s)$	[17]
Pyrolysis Reactions			
		Rate expression, Kinetics:	Source
		$K_i = A_i T^n \exp(-E_i/RT)$	
R(2)	Dry wood \rightarrow gas	$w'_b = K_2 \rho_{b,dry}$	[18]
R(3)	Dry wood \rightarrow tar	$w'_b = K_3 \rho_{b,dry}$	[18]
R(4)	Dry wood \rightarrow char	$w'_b = K_4 \rho_{b,dry}$	[18]
R(5)	Tar $\rightarrow \gamma_t \text{Tar}_{inert} + \gamma_{CO} \text{CO} + \gamma_{CO_2} \text{CO}_2 + \gamma_{H_2} \text{H}_2 + \gamma_{CH_4} \text{CH}_4$	$w'_{tar} = K_5 \rho_{tar}$	[13, 14]
Homogeneous Gas-Phase Reactions			
		Rate expression, Kinetics:	Source
		$K_i = A_i T^n \exp(-E_i/RT)$	
R(6)	$2\text{CO} + \text{O}_2 \rightarrow 2\text{CO}_2$	$R_{CO} = K_6 [\text{CO}][\text{O}_2]^{0.25} [\text{H}_2\text{O}]^{0.5}$	[13, 14]
R(7)	$\text{CH}_4 + 2\text{O}_2 \rightarrow \text{CO}_2 + 2\text{H}_2\text{O}$	$R_{CH_4} = K_7 [\text{CH}_4]^{0.7} [\text{O}_2]^{0.8}$	[13, 14]
R(8)	$2\text{H}_2 + \text{O}_2 \rightarrow 2\text{H}_2\text{O}$	$R_{H_2} = K_8 [\text{H}_2][\text{O}_2]$	[13, 14]
R(9)	$\text{Tar} + 2.9\text{O}_2 \rightarrow 6\text{CO} + 3.1\text{H}_2$	$R_{tar} = K_9 [\text{Tar}]^{0.5} [\text{O}_2]$	[13, 14]
R(10)	$\text{CO} + \text{OH} \rightarrow \text{CO}_2 + \text{H}$	$R_{CO} = K_{10} [\text{CO}][\text{OH}]$	[19]
R(11)	$\text{H} + \text{O}_2 \rightarrow \text{O} + \text{OH}$	$R_H = K_{11} [\text{O}][\text{OH}]$	[19]
R(12)	$\text{H}_2 + \text{O}_2 \rightarrow \text{OH} + \text{OH}$	$R_{H_2} = K_{12} [\text{H}_2][\text{O}_2]$	[20]
R(13)	$\text{H}_2\text{O} + \text{CO} \rightarrow \text{CO}_2 + \text{H}_2$	$R_{H_2O} = K_{13} [\text{H}_2\text{O}][\text{CO}]$	[17, 18]
R(14)	$\text{CO}_2 + \text{H}_2 \rightarrow \text{H}_2\text{O} + \text{CO}$	$R_{CO_2} = K_{14} [\text{CO}_2][\text{H}_2]$	[17, 18]
Heterogeneous Reactions			
		Rate expression, Kinetics:	Source
		$K_i = A_i T^n \exp(-E_i/RT)$	
R(15)	$\Omega \text{C} + \text{O}_2 \rightarrow 2(\Omega - 1) \text{CO} (2 - \Omega) \text{CO}_2$	$w'_{char,oz} = K_{15} P_{O_2} S_{a,char}$	[13, 14]
R(16)	$\text{C} + \text{CO}_2 \rightarrow 2\text{CO}$	$w'_{char,CO_2} = K_{16} P_{CO_2} S_{a,char}$	[13, 14]
R(17)	$\text{C} + \text{H}_2\text{O} \rightarrow \text{CO} + \text{H}_2$	$w'_{char,H_2O} = K_{17} P_{H_2O} S_{a,char}$	[13, 14]

Heat spreads to other particles by radiation, convection and conduction. As the reaction front moves downward, more pyrolysis products are released. These products are not completely reacted at their point of production. Some are transported downstream (freeboard region) where they react and generate more heat which significantly increases the temperature, as shown in Figs. 3 (d) and (e). After the reaction front moves from top to bottom, all particles in fuel bed have undergone devolatilization. As a result, the fuel bed has slightly shrunk, as shown in Fig. 3(f). The remaining biomass is now pure char which is undergoing heterogeneous reactions with O_2 , H_2O and CO_2 . The overall temperature decreases because char endothermic reactions with H_2O and CO_2 are dominant in this phase. It is also noted that in the vicinity of the grate, temperatures are lower than in the other region of the bed. Convective cooling due to cold air inlet causes this effect.

Illustrated in Figs. 4 and 5 is the mass fraction distribution of the major combustible species of pyrolysis; tar and CO. Likewise to temperature distribution, the species mass fraction distribution at a given cross-section is also non-uniform. Nonetheless, the flame front propagation is clearly depicted. Significant amounts of tar and CO are produced in the fuel bed from ignition up to about 750 s, as shown in Figs. 4 and 5. During this period, devolatilization is the dominant process. At 1000 s,

Figs. 4 and 5, traces of the volatiles noticeable in the bed indicate a char combustion stage.

Volatiles released from the bed burn within or outside the bed. The tested flow rate of oxidant is high enough to oxidize all the volatiles, as shown in Fig. 6. As the flame front moves downward, the amount of tar and CO released at its position decrease. This could be attributed to non-uniformity of flame front movement. Some particles at the same level get heated and pyrolyzed faster than others.

Shown in Fig. 7 is water vapor (H_2O) mass fraction distribution in the fuel bed. H_2O is a gaseous product arising from particle evaporation. It is also one of the pyrolysis products. In addition, H_2O in the bed is due to oxidation of CH_4 and H_2 . During initial stages of combustion, for instance, ignition up to 300 s, most of H_2O is confined to the fuel bed. This is because during this period H_2O is mostly from particle evaporation and pyrolysis. As combustion proceeds, e.g. from 400 s to 1000 s, H_2O generated in the fuel bed is spread to freeboard region by convection. It is important to notice that at this time, all the aforementioned sources participate in its production making it more pronounced than at the earlier stage. H_2O together with CO_2 are the main products of combustion that radiate heat. As a result, their effect on temperature distribution is seen in Fig. 3.

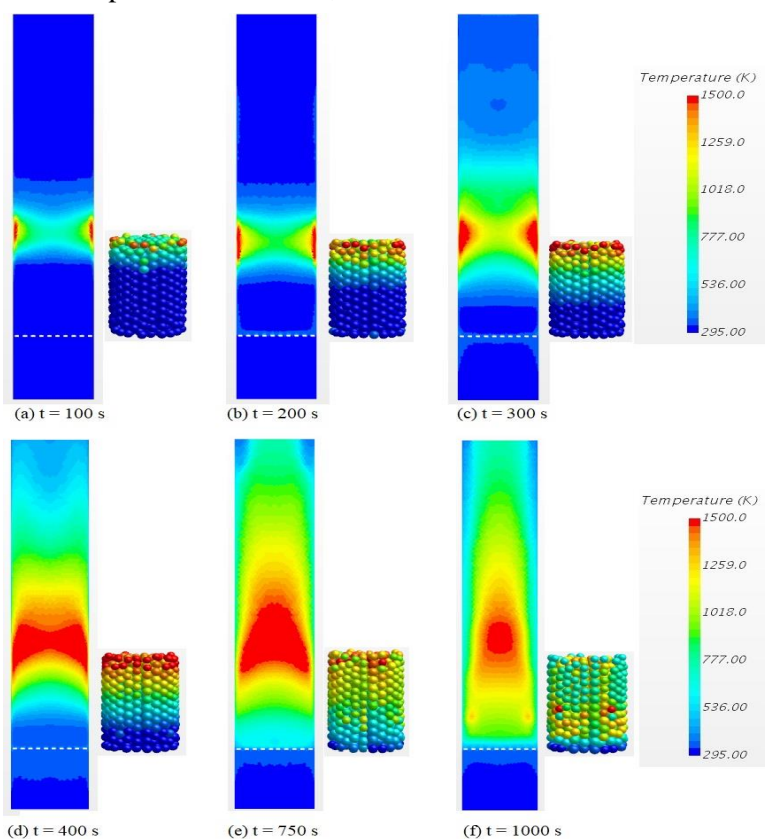


Figure 3. Gas-phase and particle surface temperature distribution in the wood fuel bed at different times.

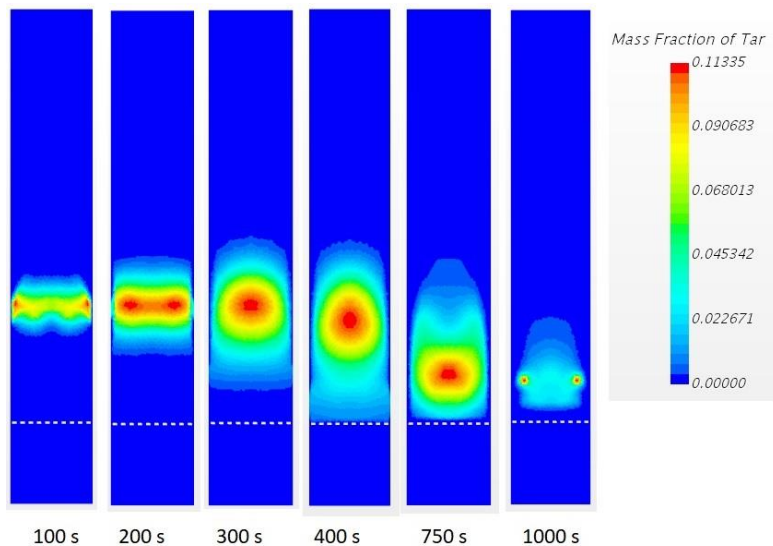


Figure 4. Tar mass fraction distribution in the wood fuel bed burning at 21%O₂/79%N₂ at different times.

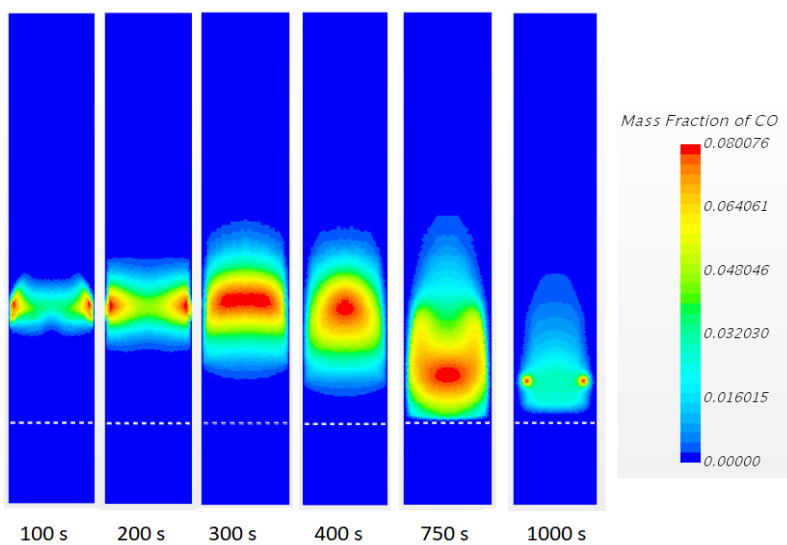


Figure 5. CO mass fraction distribution in the wood fuel bed burning at 21%O₂/79%N₂ at different times.

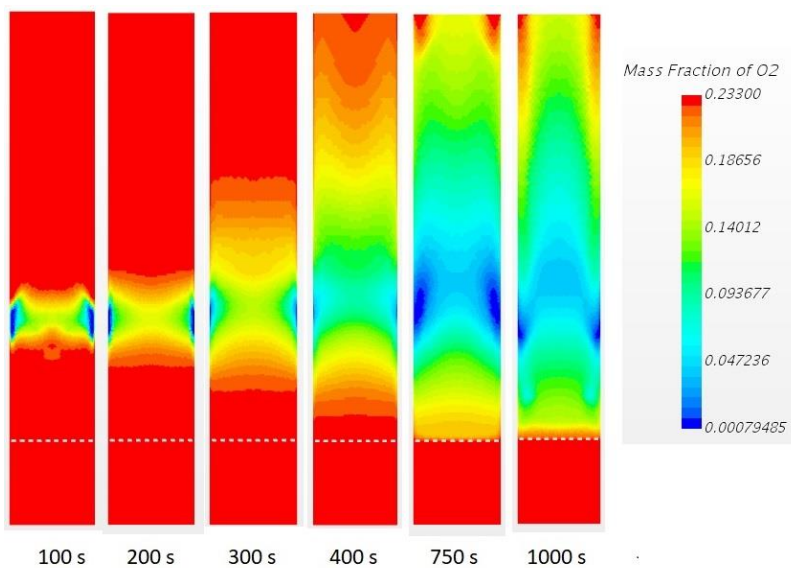


Figure 6. O₂ mass fraction distribution in the wood fuel bed burning at 21%O₂/79%N₂ at different times.

Presented in Fig. 8 is the mass fraction distribution of CO₂ in the burner. CO₂ is a product which arises from pyrolysis, as well as oxidation of CO, CH₄ and char. Its production is also contributed by tar cracking reaction. During the initial stage of combustion, 100 s to 300 s, it is observed that CO₂ production is minimal and restricted to the fuel bed. CO₂ generation is more pronounced in the last stage of combustion, 750 s and 1000 s. This is char combustion stage where char is oxidized into CO and CO₂ which increases its amount in the burner. The role of CO₂ in temperature distribution through radiation is also seen in Fig. 3.

Flame structures at different positions from fuel bed bottom are presented in Fig. 9. The graphs show

that in the freeboard region flame structures at different positions have similar profiles but differ in magnitude. Since the fixed bed that was tested was operated in batch mode under unsteady conditions, the amount of heat released changed with respect to time. At 10 cm, intense heat is released between 170 s and 600 s, while at 15 cm it is at 200 s to 600 s. These periods fall within the devolatilization stage where volatiles transported to these positions react and generate heat. Temperature then gradually decreases until the end of combustion. During this time, heat present in these positions is due to convection and radiation from fuel bed.

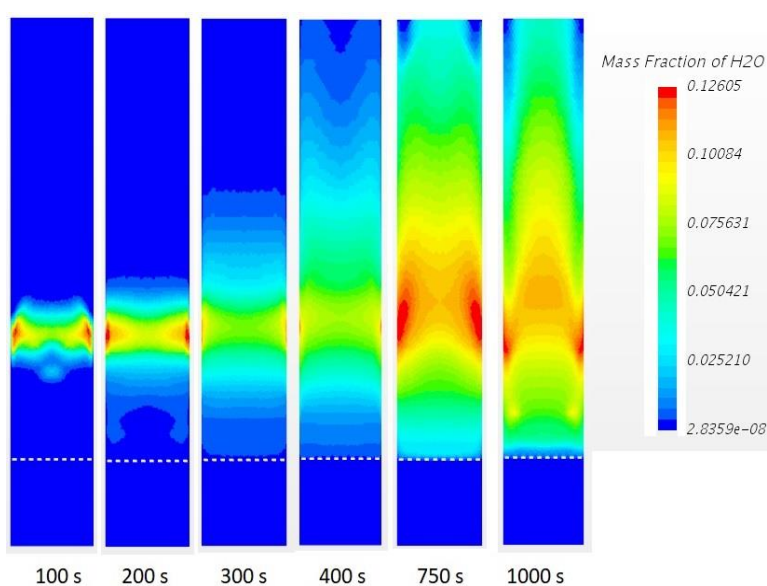


Figure 7. H₂O mass fraction distribution in the wood fuel bed burning at 21%O₂/79%N₂ at different times.

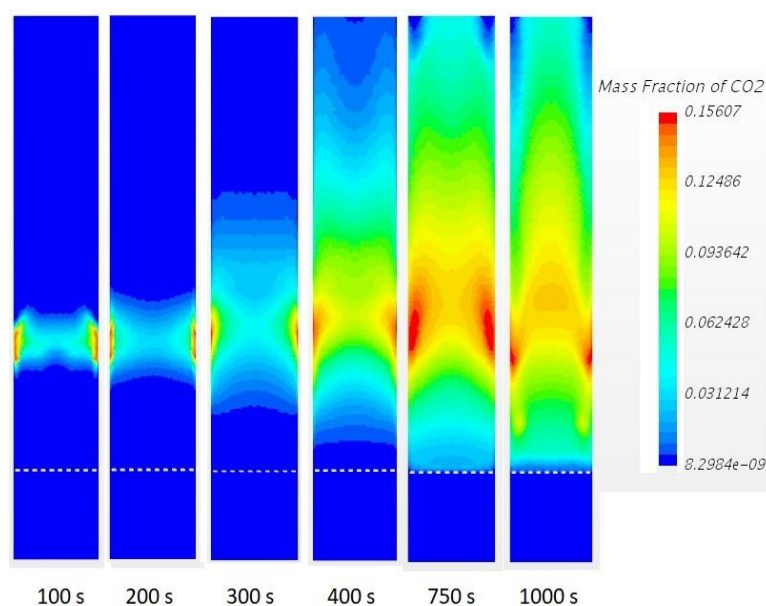


Figure 8. CO₂ mass fraction distribution in the wood fuel bed burning at 21%O₂/79%N₂ at different times.

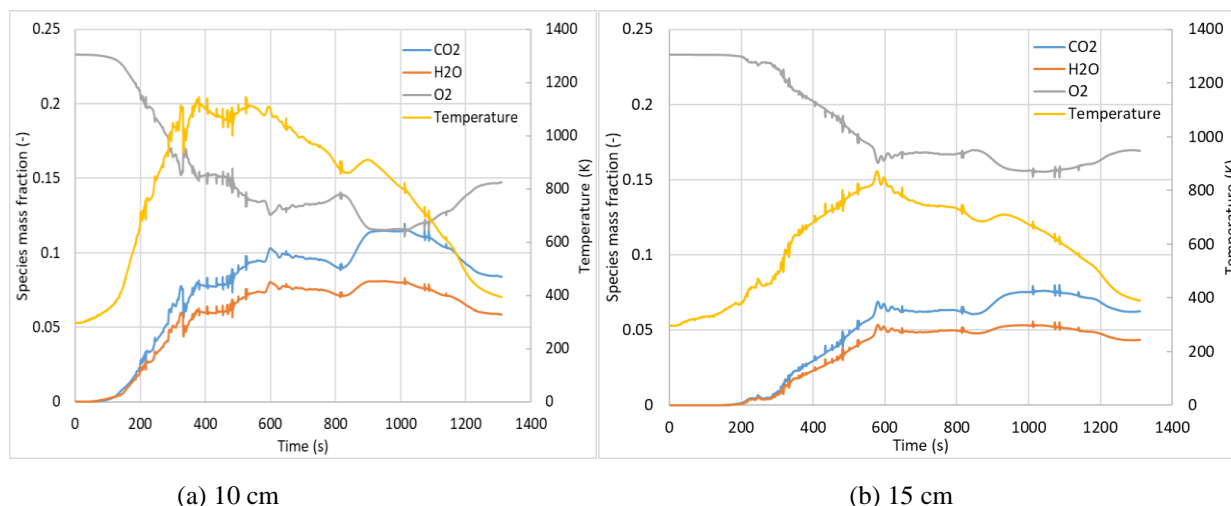


Figure 9. Major species and temperature profiles at different positions from fuel bed bottom for wood combustion at 21% O₂/79% N₂.

CONCLUSION

This study presented modeling of fixed bed combustion of wood using the CFD-DEM approach. The modeling results were validated with measurements done in a laboratory-scaled fixed bed. A good agreement between model and experimental results was achieved. Temperature distribution at the same cross-section is non-uniform. Some particles have higher temperature than others located within the same height. Likewise, species mass fraction distribution at a given cross-section is also non-uniform. Nonetheless, the flame front propagation is clearly depicted. In the freeboard region, flame structures at different positions have similar profiles but differ in magnitude. Therefore, it was proven that CFD-DEM is a good tool in design, optimization and analysis of fixed bed furnaces.

Acknowledgement: This work was financially supported by both Dedan Kimathi University of Technology, Kenya and Technical University of Applied Science Wildau, Germany. The first author would like to thank the German Academic Exchange Service (DAAD) for granting him stipend while undertaking this work at the Technical University of Applied Science, Wildau, Germany.

REFERENCES

1. S. Jiménez, J. Ballester, *Proc. Combust. Inst.*, **30**, 2965 (2005).
2. S. Jiménez, J. Ballester, *Combust. Flame*, **140**, 346 (2005).
3. Y. Bin Yang, C. Ryu, A. Khor, V. N. Sharifi, J.

- Swithenbank, *Fuel*, **84**, 2026 (2005).
4. S. Mahapatra, S. Dasappa, *Fuel Process. Technol.*, **121**, 83 (2014).
5. M. Fatehi, M. Kaviany, *Combust. Flame*, **99**, 1 (1994).
6. J. J. Saastamoinen, R. Taipale, *Combust. Flame*, **123**, 214 (2000).
7. S. Kumar, S. Dasappa, *Appl. Therm. Eng.*, **112**, 1382 (2017).
8. B. Peters, *Combust. Flame*, **146**, 132 (2002).
9. J. C. Lee, R. A. Yetter, F. L. Dryer, *Combust. Flame*, **101**, 387 (1995).
10. M. Y. Ha, B. R. Choi, *Combust. Flame*, **97**, 1 (1994).
11. J. Collazo, J. Porteiro, D. Patiño, E. Granada, *Fuel*, **93**, 149 (2012).
12. A. H. Mahmoudi, F. Hoffmann, B. Peters, *Appl. Therm. Eng.*, **93**, 1091 (2016).
13. A. H. Mahmoudi, F. Hoffmann, M. Markovic, B. Peters, G. Brem, *Combust. Flame*, **163**, 358 (2016).
14. A. H. Mahmoudi, M. Markovic, B. Peters, G. Brem, *Fuel*, **150**, 573 (2015).
15. J. K. Tanui, P. N. Kioni, T. Mirre, M. Nowitzki, *Fuel Process. Technol.*, **179**, 285 (2018).
16. CD-Adapco, "STAR CCM+ Version 11.04," www.cd-adapco.com, 2017.
17. R. Johansson, H. Thunman, B. Leckner, *Combust. Flame*, **149**, 49 (2007).
18. M. A. Gómez, J. Porteiro, D. de la Cuesta, D. Patiño, J. L. Míguez, *Fuel*, **184**, 987 (2016).
19. G. P. Smith, D. M. Golden, M. Frenklach, N. W. Moriarty, B. Eiteneer et al., "GRI-Mech 3.0," 1999. <http://combustion.berkeley.edu/gri-mech/version30/text30.html>.
20. C. K. Westbrook, F. L. Dryer, *Prog. Energy Combust. Sci.*, **10**, 1 (1984).

Warfarin replaces dexamethasone in drug complexes with human serum albumin - a fluorescence spectroscopy study

S. Abarova*, A. Papageorgiou, Y. Ivanov, B. Tenchov

Department of Medical Physics and Biophysics, Medical University-Sofia, 1431 Sofia, Bulgaria

Received: March 16, 2020; Accepted: March 19, 2020

In this work we used fluorescence spectroscopy to study the interaction of human serum albumin (HSA) with two widely used drugs, the anticoagulant warfarin (War) and the synthetic corticosteroid medication dexamethasone (Dex). Intrinsic fluorescence emission spectra of HSA in presence of the studied drugs, recorded in the range 300-500 nm at an excitation wavelength of 283 nm, showed that both drugs form complexes with HSA and act as quenchers. The HSA-drug complex formation manifested a significant decrease in the fluorescence intensity most likely due to changes in the protein fluorophore (Trp-214) environment caused by the drug binding to HSA subdomain IIA. In addition to the quenching effect, War binding caused a red shift and Dex binding caused a blue shift of the HSA emission maximum at 337 nm. Remarkably, the addition of War to already formed HSA-Dex complexes caused a red shift of the emission maximum to higher wavelengths typical of HSA-War complexes, while the addition of Dex to preformed HSA-War complexes resulted in no spectral shifts. We conclude on this basis that War has a higher binding affinity to HSA than Dex, respectively, it successfully competes with Dex for the binding site and can replace Dex in already formed HSA-Dex complexes. This effect is of certain interest as it may influence the balance between bound and freely circulating drugs in cases of simultaneous application of two drugs, thus affecting the drug pharmacokinetics, efficacy and adverse side effects.

Keywords: dexamethasone; warfarin; human serum albumin; fluorescence spectroscopy; quenching; drug binding

INTRODUCTION

Albumin, the most abundant protein in blood plasma, has high binding affinity to many endogenous and exogenous compounds and serves as their transporter in the circulation. Among the transported substances are various metabolites, drugs, and other biologically active compounds present in the blood [1]. In the present work we used fluorescence spectroscopy to study the interaction of two widely used drugs, warfarin and dexamethasone, with human serum albumin (HSA).

Warfarin (War, Fig. 1a), 3-(α -acetonylbenzyl)-4-hydroxy-coumarin, is the most widely used oral anticoagulant. Its metabolical assimilation by the human organism is excellent [2].

Dexamethasone (Dex, Fig. 1b), pregna-1,4-diene-3,20-dione,9-fluoro-11,17,21-trihydroxy-16-methyl-, (11 β ,16 α)-, is a synthetic corticosteroid medication that is widely used in clinical treatment of Addison's disease, systemic lupus erythematosus,

allergic reactions, certain skin and eye conditions, breathing problems, bowel disorders, certain cancers and autoimmune diseases (pubchem.ncbi.nlm.nih.gov/compound/dexamethasone). Dex is easy to overdose. Its adverse side effects include seizures, gastrointestinal perforation, and heart attack. Long-term use can also cause Cushing's syndrome, osteoporosis, and cataracts [3].

Both Dex and War are known to bind to HSA [4, 5]. However, their mutual interactions upon simultaneous application and formation of complexes with HSA are not clear. In particular, the effect of War on the HSA-Dex complexes in the blood circulation is not well characterized. Therefore, investigating the interaction of Dex with HSA in the presence of War can provide useful information about the drug relative affinities to HSA and can be used as a model to clarify the properties of the drug-protein complexes in cases of simultaneous application of the two drugs.

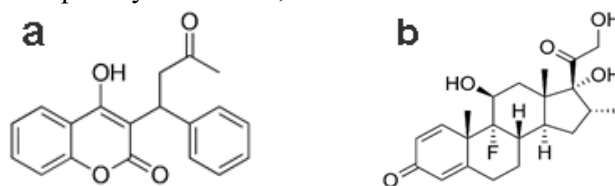


Fig. 1. Chemical structures of the drugs studied: a) warfarin, b) dexamethasone.

* To whom all correspondence should be sent:

E-mail: sabarova@abv.bg

In order to analyze the possible influence of War on the properties of the HSA-Dex complexes, we focused here on investigating the effects of War and Dex on the drug-HSA fluorescence spectra, fluorescence quenching mechanisms, binding constants and binding mode. These measurements are expected to provide information on the HSA-Dex and HSA-War relative complex stability.

MATERIALS AND METHODS

Fatty acid-free human serum albumin and warfarin were obtained from Sigma-Aldrich. Dexamethasone solution for injection (4 mg/ml dexamethasone phosphate in PBS, Sopharma) was purchased from a pharmacy shop. Stock solutions of HSA, War, and Dex were prepared in PBS, pH 7.4, and diluted to various lower concentrations for actual use.

Fluorescence Spectroscopy

A Scinco 2 spectrofluorimeter (South Korea) with temperature control accessory was used to measure the fluorescence spectra. Bandwidths for both excitation and emission were 5 nm. Fluorescence measurements of HSA-Dex and HSA-War mixtures were carried out by keeping a constant HSA concentration, while the Dex and War concentrations were varied in a broad range. Fluorescence spectra were recorded at three temperatures, 288, 298, and 310 K. The fluorescence emission range was 300–500 nm and the excitation wavelength was 283 nm.

UV-Vis Absorption Measurements

UV absorption spectra of HSA and its complexes with the drugs studied were measured in the range of 250–330 nm ($n = 5$ replicates) at 298 K.

RESULTS AND DISCUSSION

The HSA intrinsic fluorescence emission spectra recorded at three different temperatures are shown in Fig. 2. As could be expected, the HSA fluorescence intensity decreases with temperature increase. The intrinsic fluorescence of HSA is mainly due to the tryptophan residue Trp-214 in the hydrophobic cavity of HSA subdomain IIA (Sudlow's binding site I). Accordingly, if a compound binds to the latter site, it will likely affect the HSA intrinsic fluorescence [6].

Quenching of the HSA Fluorescence Spectrum by Warfarin and Dexamethasone

War is known to bind to subdomain IIA of HSA (Sudlow's binding site I) where its interaction with the protein is dominated by hydrophobic contacts.

According to published data, the interaction between the War benzyl ring and the Trp-214 moiety represents a major contribution to the stability of the HSA-War complex [7-9].

As shown in Fig. 3, the HSA fluorescence is gradually quenched by addition of increasing War concentrations. The decrease of the fluorescence intensity is accompanied by a shift in the fluorescence maximum to higher wavelengths (red shift). These data suggest that War forms a complex with HSA leading to a microenvironment change in subdomain IIA and consequently to quenching of the Trp-214 fluorescence.

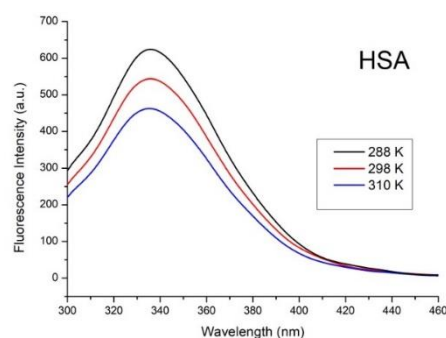


Fig. 2. Intrinsic fluorescence emission spectra of 30 μM HSA at temperatures 288, 298 and 310 K. Excitation wavelength $\lambda_{\text{ex}} = 283$ nm.

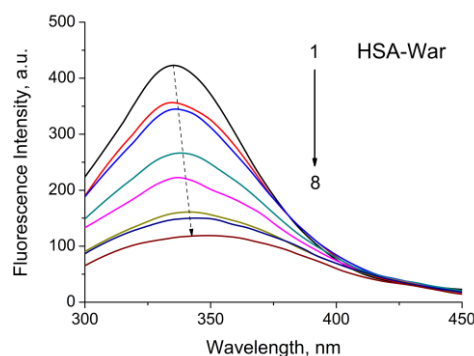


Fig. 3. Quenching of the fluorescence emission spectrum of 20 μM HSA by warfarin (War) at 298 K. Curves 1-8 correspond to War concentrations of 0, 6, 12, 18, 24, 30, 36, 42 μM , respectively. The emission maximum experiences a red shift with increase of War concentration (dashed arrow).

Addition of Dex to HSA solutions also quenched the HSA fluorescence (Fig. 4) [10]. This indicates binding of Dex to the HSA subdomain IIA where tryptophan Trp-214 is located. The increase of the Dex concentration was accompanied by a blue shift of the emission maximum (Fig. 5). Blue shifts typically result from placement of the protein fluorophore Trp-214 in a more hydrophobic environment, apparently reached in the present case

after the binding of Dex to the HSA subdomain IIA [4].

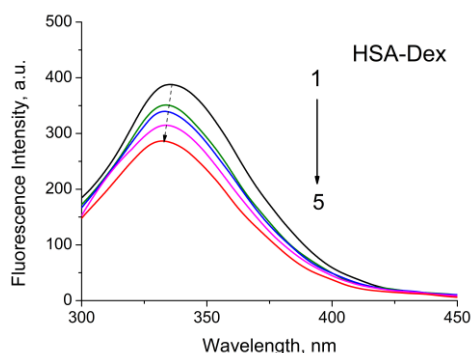


Fig. 4. Quenching of the fluorescence emission spectrum of 20 μM HSA by dexamethasone (Dex) at 298 K. Curves 1-5 correspond to Dex concentrations 0, 6, 12, 18 and 24 μM , respectively. The emission maximum experienced a blue shift with increase of Dex concentration (dashed arrow).

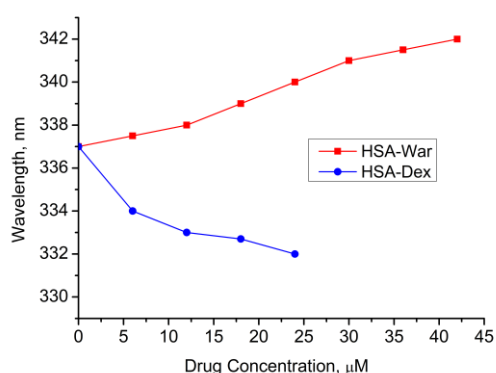


Fig. 5. Shifts in the fluorescence emission maximum upon addition of warfarin (red shift to higher wavelengths) and dexamethasone (blue shift to lower wavelengths). HSA concentration 30 μM .

Quenching Mechanism of HSA Fluorescence by War and Dex

The interactions of War and Dex with HSA were measured at three temperatures 288 K, 298 K, and 310 K and the temperature data were used to determine the nature of the drug interactions with HSA. The fluorescence quenching and the spectral shift effects at 288 K and 310 K (not shown) were similar to the results shown in Figs. 3 and 4 for 298 K.

According to its mechanism, fluorescence quenching can be dynamic or static [11]. Dynamic quenching results from collisional encounters of the quencher with the fluorophore in excited state, while static quenching results from complex formation between the fluorophore in its ground state and the quencher. Dynamic and static quenching can be distinguished from their dependence on temperature

and viscosity. The decrease in emission intensity upon quenching can be described by the Stern–Volmer equation:

$$F_0/F = 1 + K_{SV} Q$$

where F_0 and F are the fluorescence intensities in the absence and presence of quencher, respectively, Q is the concentration of the quencher, and K_{SV} is the Stern–Volmer quenching constant. Plots of F_0/F vs. Q are indicative for the type of quenching, i.e., they can be either linear for static or dynamic quenching, or display an upward curve for mixed quenching types [11]. For the linear plots obtained in the present study, the Stern–Volmer quenching constant K_{SV} can be calculated using the above equation. Its values for three different temperatures are given in Table 1. The K_{SV} decrease with increase of temperature shows that the HSA fluorescence quenching for both War and Dex takes place via a static quenching mechanism. The K_{SV} values also show the sensitivity of the fluorophore to a quencher. For the studied here HSA, quenching with War is obviously more efficient than quenching with Dex, as is clear from the K_{SV} values in Table 1.

Table 1. Stern–Volmer quenching constants K_{SV} for HSA complexes with War and Dex.

Temperature, K	HSA-War	HSA-Dex
	$K_{SV} \times 10^{-4} \text{ M}^{-1}$	$K_{SV} \times 10^{-4} \text{ M}^{-1}$
288	5.24	2.57
298	3.03	1.62
310	1.96	1.10

Displacement of Dex by War in HSA-Dex Complexes

In order to evaluate the relative stability of the HSA-War and HSA-Dex complexes we applied the following protocol. First, 5 μM HSA was reacted with 4 μM Dex and a small blue shift of about 1 nm was recorded for the HSA-Dex complex. After that, increasing concentrations of War were added, which resulted in a strong red shift of the fluorescence emission, showing that War replaced Dex in the HSA-Dex complexes (Figs. 6A and 6B). Alternatively, 5 μM HSA was reacted with 4 μM War and a small red shift of about 1 nm was recorded. After that, increasing concentrations of Dex were added, which resulted in no shifts in the emission maximum (Fig. 6B). These observations show that War binds more strongly to HSA and cannot be displaced even by large Dex concentrations, while the Dex binding is weaker than that of War and, correspondingly, War can displace

Dex from its complex with HSA. These observations were corroborated by previous findings [4] that addition of War reduced the binding constants of Dex to HSA. The observed by us displacement of Dex by War also showed that Dex most likely binds to the same site in subdomain IIA, which serves as binding locus for War with Trp-214 located near or within the binding site.

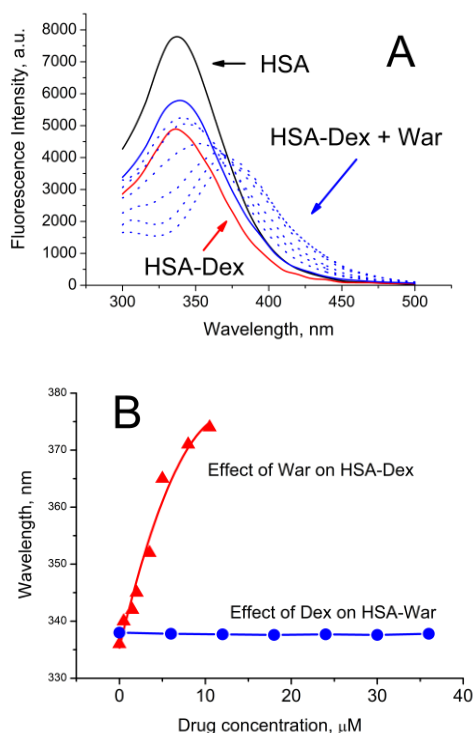


Fig. 6. A. Red shifts in the emission spectra of 5 μM HSA-4 μM Dex complexes upon addition of increasing War concentrations from 0.5 to 10.5 μM; B. Red spectral shifts induced by addition of War to HSA-Dex complexes (red triangles) and absence of spectral shifts upon addition of Dex to HSA-War complexes.

The influence of War and Dex on the UV-Vis Spectra of HSA

The UV absorption spectra exhibited by proteins are due to absorption by Trp (280 nm), Tyr (280 nm) and Phe (257 nm), also by the peptide bonds (225 nm) [12-14]. Here we measured the UV-Vis absorption spectra of HSA and HSA-drug complexes in order to identify and confirm the mechanism of the quenching process. We found that the UV absorption of HSA increased upon addition of both War and HSA (Fig. 7). As dynamic quenching only affects the excited states of the fluorophores, it results in no change in the absorption spectra. Thus, UV absorption increase upon addition of War and Dex to HSA indicates formation of HSA complexes with the drugs. These data confirmed once again that War and Dex quenched the HSA

intrinsic fluorescence by means of a static quenching mechanism, in agreement with our previous work and other published studies [10, 15].

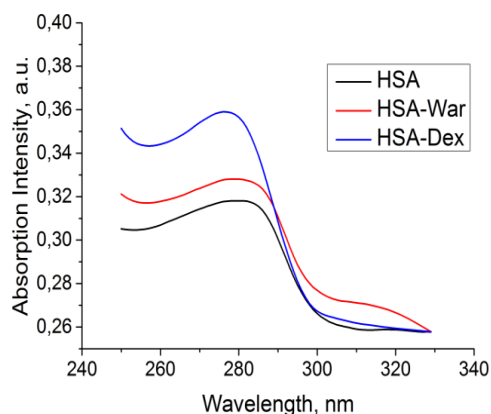


Fig. 7. UV absorption spectra of HSA, HSA-War and HSA-Dex complexes. $C_{HSA} = C_{War} = C_{Dex} = 4 \mu\text{M}$.

CONCLUSIONS

Measurements of HSA intrinsic fluorescence showed that two widely used drugs, War and Dex, form complexes with HSA, manifested in strong fluorescence quenching. In addition to their quenching effect, War and Dex also caused red and blue shifts, respectively, of the HSA emission maximum at 337 nm.

Based on these spectral shifts, we applied a new, rather sensitive protocol to evaluate the relative stability of the HSA-drug complexes and found that War displays a higher affinity to HSA and can displace Dex from the HSA-Dex complexes, while Dex cannot displace War from the HSA-War complexes even at rather high Dex concentrations. This effect is of certain interest as it sheds light on the balance between bound and freely circulating drugs in cases of simultaneous application of two drugs, thus affecting the drug pharmacokinetics, efficacy and adverse side effects.

Acknowledgements: This work was supported by grant D-241/19. 12. 2019 by SMN at the Medical University-Sofia.

REFERENCES

1. M. T. Larsen, M. Kuhlmann, M. L. Hvam, K. A. Howard, *Mol. Cell. Ther.*, **4**, 3 (2016).
2. J. D. Horton, B. M. Bushwick, *Am. Fam. Physician*, **59**, 635 (1999).
3. F. Buttgerit, J. A. P. Da Silva, M. Boers, G. Burmester, M. Cutolo, J. Jacobs, J. Kirwan, L. Kohler, P. van Riel, T. Vischer, J. Bijlsma, *Ann. Rheum. Dis.*, **61**, 718 (2002).
4. P. Naik, S. A. Chimatadar, S. T. Nandibewoor, *Journal of Photochemistry and Photobiology*, **100**(3), 147 (2010).

5. Z. J. Yasseen, M. O. El-Ghossain, *Journal of Biomedical Sciences*, **5**, 3 (2016).
6. F. Yang, Y. Zhang, *Int. J. Mol. Sci.*, **15**, 3580 (2014).
7. R. Ishima, D. A. Torchia, *Nature Struct. Mol. Biol.*, **7**, 740 (2000).
8. H. J. Dyson, *Chem. Rev.*, **104**, 3607 (2004).
9. G. D. Fasman, *Infrared and Raman Spectroscopy of Biological Materials*, New York, Plenum Press, 1996, p. 109.
10. S. M. Abarova, A. Zasheva, R. Koynova, B. Tenchov, *Comptes Rendus de l'Académie Bulgare des Sciences*, in press.
11. J. R. Lakowicz, *Principles of Fluorescence Spectroscopy*, 3rd edn. New York, Springer, 2006.
12. M. C. Otey, J. P. Greenstein, *Arch. Biochem. Biophys.*, **53**, 501 (1954).
13. C. R. Cantor, P. R. Schimmel, *Biophysical Chemistry*. W. H. Freeman Publ., New York, 1980.
14. G. D. Fasman, CRC Press, New York, 1992.
15. L. Qiang, W. Yang, L. Qu, H. Qi, Y. Huang, Z. Zhang, *Hindawi Publishing Corporation Journal of Spectroscopy*, Article ID 834501 (2014).

Instructions about Preparation of Manuscripts

General remarks: Manuscripts are submitted in English by e-mail. The text must be typed on A4 format paper using Times New Roman font size 11, normal character spacing. The manuscript should not exceed 15 pages (about 3500 words), including photographs, tables, drawings, formulae, etc. Authors are requested to use margins of 2 cm on all sides.

Manuscripts should be subdivided into labelled sections, e.g. **Introduction, Experimental, Results and Discussion, etc.** The **title page** comprises headline, author's names and affiliations, abstract and key words. Attention is drawn to the following:

a) **The title** of the manuscript should reflect concisely the purpose and findings of the work. Abbreviations, symbols, chemical formulas, references and footnotes should be avoided. If indispensable, abbreviations and formulas should be given in parentheses immediately after the respective full form.

b) **The author's** first and middle name initials and family name in full should be given, followed by the address (or addresses) of the contributing laboratory (laboratories). **The affiliation** of the author(s) should be listed in detail by numbers (no abbreviations!). The author to whom correspondence and/or inquiries should be sent should be indicated by asterisk (*) with e-mail address.

The abstract should be self-explanatory and intelligible without any references to the text and containing not more than 250 words. It should be followed by key words (not more than six).

References should be numbered sequentially in the order, in which they are cited in the text. The numbers in the text should be enclosed in brackets [2], [5, 6], [9–12], etc., set on the text line. References are to be listed in numerical order on a separate sheet. All references are to be given in Latin letters. The names of the authors are given without inversion. Titles of journals must be abbreviated according to Chemical Abstracts and given in italics, the volume is typed in bold, the initial page is given and the year in parentheses. Attention is drawn to the following conventions: a) The names of all authors of a certain publication should be given. The use of "*et al.*" in the list of references is not acceptable. b) Only the initials of the first and middle names should be given. In the manuscripts, the reference to author(s) of cited works should be made without giving initials, e.g. "Bush and Smith [7] pioneered...". If the reference carries the names of three or more authors it should be quoted as "Bush *et al.* [7]", if Bush is the first author, or as "Bush and co-workers [7]", if Bush is the senior author.

Footnotes should be reduced to a minimum. Each footnote should be typed double-spaced at the bottom of the page, on which its subject is first mentioned. **Tables** are numbered with Arabic numerals on the left-hand top. Each table should be referred to in the text. Column headings should be as short as possible but they must define units unambiguously. The units are to be separated from the preceding symbols by a comma or brackets. Note: The following format should be used when figures, equations, etc. are referred to the text (followed by the respective numbers): Fig., Eqns., Table, Scheme.

Schemes and figures. Each manuscript should contain or be accompanied by the respective illustrative material as well as by the respective figure captions in a separate file (sheet). As far as presentation of units is concerned, SI units are to be used. However, some non-SI units are also acceptable, such as °C, ml, l, etc. The author(s) name(s), the title of the manuscript, the number of drawings, photographs, diagrams, etc., should be written in black pencil on the back of the illustrative material (hard copies) in accordance with the list enclosed. Avoid using more than 6 (12 for reviews, respectively) figures in the manuscript. Since most of the illustrative materials are to be presented as 8-cm wide pictures, attention should be paid that all axis titles, numerals, legend(s) and texts are legible.

The authors are required to submit the text with a list of three individuals and their e-mail addresses that can be considered by the Editors as potential reviewers. Please, note that the reviewers should be outside the authors' own institution or organization. The Editorial Board of the journal is not obliged to accept these proposals.

The authors are asked to submit **the final text** (after the manuscript has been accepted for publication) in electronic form by e-mail. The main text, list of references, tables and figure captions should be saved in separate files (as *.rtf or *.doc) with clearly identifiable file names. It is essential that the name and version of the word-processing program and the format of the text files is clearly indicated. It is recommended that the pictures are presented in *.tif, *.jpg, *.cdr or *.bmp format.

The equations are written using “Equation Editor” and chemical reaction schemes are written using ISIS Draw or ChemDraw programme.

EXAMPLES FOR PRESENTATION OF REFERENCES

REFERENCES

1. D. S. Newsome, *Catal. Rev.–Sci. Eng.*, **21**, 275 (1980).
2. C.-H. Lin, C.-Y. Hsu, *J. Chem. Soc. Chem. Commun.*, 1479 (1992).
3. R. G. Parr, W. Yang, *Density Functional Theory of Atoms and Molecules*, Oxford Univ. Press, New York, 1989.
4. V. Ponec, G. C. Bond, *Catalysis by Metals and Alloys (Stud. Surf. Sci. Catal., vol. 95)*, Elsevier, Amsterdam, 1995.
5. G. Kadinov, S. Todorova, A. Palazov, in: *New Frontiers in Catalysis (Proc. 10th Int. Congr. Catal., Budapest, (1992)*, L. Guzzi, F. Solymosi, P. Tetenyi (eds.), Akademiai Kiado, Budapest, 1993, Part C, p. 2817.
6. G. L. C. Maire, F. Garin, in: *Catalysis. Science and Technology*, J. R. Anderson, M. Boudart (eds), vol. 6, SpringerVerlag, Berlin, 1984, p. 161.
7. D. Pocknell, *GB Patent 2 207 355* (1949).
8. G. Angelov, PhD Thesis, UCTM, Sofia, 2001, pp. 121-126.
- 9 JCPDS International Center for Diffraction Data, Power Diffraction File, Swarthmore, PA, 1991.
10. CA **127**, 184 762q (1998).
11. P. Hou, H. Wise, *J. Catal.*, in press.
12. M. Sinev, private communication.
13. <http://www.chemweb.com/alchem/articles/1051611477211.html>.

Texts with references which do not match these requirements will not be considered for publication!!!

CONTENTS

<i>B. Mombeni Goodajdar, F. Akbari</i> , An efficient synthesis of azidohydrin catalyzed by a novel polymeric ionic liquid	335
<i>A. G. Dyachenko, O. V. Ischenko, M. G. Zhudenko, S. V. Gaidai, T. M. Zakharova, A. V. Yatsymyrskyi, V. V. Lisnyak</i> , CO ₂ methanation over Co-Ni/Al ₂ O ₃ and Co-Ni/SiC catalysts..	342
<i>M. Meena, M. J. Umapathy</i> , Toxic solvent-free: Radical polymerizations of vinyl monomers using a di-site phase-transfer catalyst – a kinetic approach.....	348
<i>A. A. Hasan</i> , Gravitational instability of a rotating streaming plasma cloud with radiation....	355
<i>P. A. Mule, M. K. Patil, M. E. Navgire, A. A. Yelwande</i> , NiO-ZrO ₂ heterogeneously catalysed efficient multicomponent synthesis of polyhydroquinoline derivatives.....	362
<i>V. Rupetsov, S. Dishliev, G. Mishev, F. Franek, M. Premauer, L. Kolakleva</i> , Research of tribological parameters of multilayer coating Ti/TiN/CrN-ml deposited on 1.2343 steel....	369
<i>F. Sarf</i> , Structural and electrochemical properties of Ni doped and MWCNTs coated ZnO thin films.....	374
<i>Hr. Najdenski, V. Hubenov, I. Simeonov, V. Kussovski, L. Dimitrova, P. Petrova, P. Angelov, L. Kabaivanova</i> , Microbial biodegradation as an option for waste utilization during long-term manned space missions.....	379
<i>S. Verma, V. Chauhan, S. Bharti, M. M. Mandal</i> , Hydrodynamics of the flow of two immiscible liquids in a coiled tube of small diameter.....	387
<i>J. K. Tanui, P. N. Kioni, T. Mirre, M. Nowitzki, D. A. Todorova</i> , Application of CFD-DEM method in modeling of wood combustion in a fixed bed.....	396
<i>S. Abarova, A. Papageorgiou, Y. Ivanov, B. Tenchov</i> , Warfarin replaces dexamethasone in drug complexes with human serum albumin - a fluorescence spectroscopy study.....	404
INSTRUCTIONS TO AUTHORS	409